Motion compensation for MRI-guided radiotherapy

Markus Glitzner

Cover The magnet reverses motion-induced dispersion.
Design: M. E. Löffler (oblique.at)

Motion compensation for MRI-guided radiotherapy
PhD thesis, Utrecht University, The Netherlands

Manuscript
Layout: M. Glitzner
Typeset in: LaTeX 2$_\varepsilon$
Printed by: Ipskamp Drukkers
ISBN: 978-90-393-6798-8

Financial support for publication of this thesis was kindly provided by Elekta B.V. and Philips Healthcare.

Motion compensation for MRI-guided radiotherapy

Bewegingscompensatie voor MRI-gestuurde radiotherapie

(met een samenvatting in het Nederlands)

Proefschrift

ter verkrijging van de graad van doctor aan de
Universiteit Utrecht
op gezag van de rector magnificus, prof. dr. G.J. van der Zwaan,
ingevolge het besluit van het college voor promoties
in het openbaar te verdedigen
op vrijdag 7 juli 2017 des middags te 12.45 uur

door
Markus Glitzner
geboren op 10 oktober 1985
te Hallein bei Salzburg, Oostenrijk

Promotoren:	Prof. dr. B.W. Raaymakers
	Prof. dr. ir. J.J.W. Lagendijk
Copromotoren:	Dr. ir. S.P.M. Crijns
	Dr. B. Denis de Senneville

This dissertation was partly accomplished with financial support from the ITEA programme (project 12026 SoRTS).

Contents

List of acronyms

4DCT 4D computed tomography

ADC apparent diffusion coefficient

ALF aperture light field

AP anterior-posterior

API application programming interface

ART adaptive radiotherapy

ASEQ adaptive sequencing

BEV beam's eye view

BOLD blood oxygenation level dependent

CARTAR convolution-adapted ratio of tissue-air ratios

CC caudo-cranial

COG center of gravity

CPU central processing unit

CSC control system cycle

CBCT cone beam computed tomography

CT computed tomography

CTV clinical target volume

CUDA compute unified device architecture

DAH dose-area histogram

DIR deformable image registration

dMLC dynamic multileaf collimator

DVF deformation vector field

DVH dose-volume histogram

EBRT external beam radiotherapy

ED electron density

EM electro-magnetic

EPI echo planar imaging

EPID electronic portal imaging device

ERE electron return effect

FFE fast field echo

FFF flattening filter free

FIFO first in first out

FOV field of view

GTV gross tumor volume

GPU graphics processing unit

HIFU high intensity focused ultrasound

HU Hounsfield unit

ICRU International Commission on Radiation Units and Measurements

IGRT image guided radiotherapy

IMRT intensity modulated radiotherapy

ITV internal target volume

kV kilovoltage

KDE kernel density estimator

linac linear accelerator

LED light emitting diode

LPS linear positioning system

MC Monte-Carlo

MLC multileaf collimator

MOSSE minimum output sum of squared error

MR magnetic resonance

MRI magnetic resonance imaging

MV megavoltage

NMR nuclear magnetic resonance

OAR organ at risk

PCA principal component analysis

pCT pseudo-CT

PGK penumbra-generating kernel

PNS peripheral nerve stimulation

PSF point spread function

PTV planning target volume

QA quality assurance

RCC renal cell carcinoma

RF radio frequency

RPM *Real-time Position Management*

RMS root mean square

SAD source-to-axis distance

SAR specific absorption rate

SBRT stereotactic body radiotherapy

SENSE sensitivity encoding

SID source-to-imager distance

SNR signal to noise ratio

TCP tumor control probability

VMAT volumetric intensity modulated arc therapy

VOI volume of interest

TFE turbo field echo

TPS treatment planning system

TTL transistor-transistor logic

US ultrasound

USB universal serial bus

CHAPTER 1

Introduction

Radiotherapy is an established option for cancer treatment, applied in more than 50% of all cases (Delaney et al. 2005). The therapeutic effect is based on the local interaction of ionizing radiation with tissue. In external beam radiotherapy (EBRT) or *teletherapy*, a high energy megavoltage (MV) photon beam is generated and directed at a typically compact distribution of cancerous cells, within a neighborhood of normal, healthy tissue.

Typically, in the preparation phase of radiotherapy, computed tomography (CT) is used. CT produces 3D images of the anatomy with high geometric fidelity and high, sub-millimeter resolution, which are used to identify and contour target structures, as well as organs at risk (OAR). Furthermore, electron density (ED) maps can be extracted from CTs which can be used to estimate the location of ionization events by computing a particle's trajectory through tissue (Purdy 1992).

During the radiotherapy planning process, therapeutic energy prescriptions in Gray (Gy) are translated into a sequence of delivery machine actions. Based on the ED distribution and the target contours, delivery schemes for prescribed energy distributions are calculated. Depending on the complexity of the treatment planning system (TPS) and the beam models used, treatment plans are obtained either in a forward or inverse planning manner (Ahnesjö and Aspradakis 1999).

1.1 Uncertainties and conformity

The imaging and planning process, in which the distribution of radiation energy (dose) is defined according to the exact patient anatomy and prescriptions, is done only once prior to the treatment series. The patient geometry is thus assumed to be reproducible throughout the treatment course. Superficial markers, such as tattoos on the skin of the patient serve as geometric reference points. Isocenter

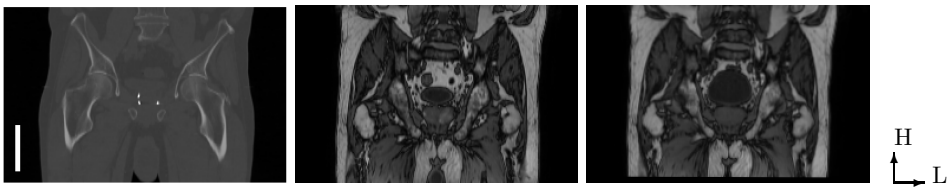

(a) Planning CT **(b)** Planning MRI **(c)** Later MRI

Figure 1.1: CT and MR imaging in the planning phase. Bony anatomy and gold fiducial markers in the prostate are clearly visible on CT (a), while MRI offers soft-tissue definition (b). In subsequent fractions, bladder filling can cause significant internal anatomy variations (c). Scale bar in (a): 10 cm.

lasers on both preparation and therapy units are then used to match the reference points in order to align the generated treatment plan to the patient. Figures 1.1a and 1.1b depict CT and magnetic resonance (MR) images of a patient's anatomy in the planning state.

However, the assumption of a reproducible patient anatomy is inherently wrong, as physiologic processes and limited positioning precision are imposing geometric displacements, leading to position uncertainties. The nature of these uncertainties and their mitigation are a main branch of research and also the content of this thesis. Position uncertainties due to physiology are typically distinguished according to the time constants of the physiologic processes. Processes which change the anatomy between the individual treatment sessions cause *inter-fraction* motion. For example slow digestive processes, such as rectum and bladder filling, which is shown in fig. 1.1c. These effects have been extensively studied for the pelvis, however, position variations due to organ filling have also been reported in abdominal sites (Wysocka et al. 2010). Additionally, effects of therapy response, such as weight loss, tumor size variation or migration can lead to *inter-fraction* variation (Langen and Jones 2001).

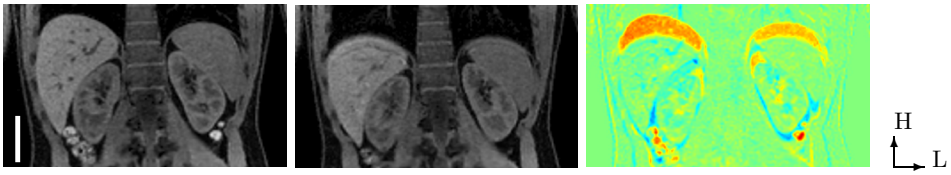

(a) exhale **(b)** inhale **(c)** Δ

Figure 1.2: Dynamic range of intrafraction motion in an MRI of a volunteer in a coronal slice. Respiratory motion (exhale in (a), inhale in (b)) causes displacements of up to 3 cm (intensity difference in (c)). Scale bar in (a): 10 cm.

Faster processes acting in the course of one session effect *intra-fraction* variation. Its most prominent type is the continuous geometric modulation of the thorax

and abdomen due to breathing, accounting for peak displacements of 35 mm for kidney (Moerland et al. 1994), 25 mm for lung and liver (Shirato et al. 2004) and 42 mm for pancreas (Feng et al. 2009). Figure 1.2 illustrates the gravitas of breathing motion, showing a coronal MRI acquisition of a volunteer in inhale- and exhale-state, respectively. Next to the periodic breathing, drift components have been reported, causing a continuous baseline shift in the *intra-fraction* regimen (Siebenthal et al. 2007b; Zachiu et al. 2015).

The entire range of described internal changes remain invisible to positioning techniques based on superficial markers. The target dose, which was planned assuming static anatomy throughout the treatment course, is thus diluted as a function of the internal motion. In order to compensate for these motion effects, motion margins have been conceptualized, which extend the clinically relevant target volume (clinical target volume (CTV)) to a planning target volume (PTV), in order to encompass the geometric errors and thus retain the target dose (ICRU 83 2010). Derivation of these margins is a statistical exercise, balancing accepted treatment delivery errors against systematic and random errors observed in a large population (Van Herk et al. 2000).

Although radiation can be delivered with increasingly high conformity from a machine point of view (Wolff et al. 2009), the use of error margins inevitably imposes clinically unintended dose onto OAR in the vicinity of the target, increasing the risk of acute and late side effects. In order to achieve an optimal differential sparing between the (unintended) damage to the OAR and the (intended) damage to the target, the prescription dose has to be applied in a fractionated manner (Fowler 2005), typically applying 30-40 fractions per treatment course.

1.2 Hypofractionated therapy

Hypofractionation is a treatment regimen which prescribes a smaller number of therapy sessions than usual. The rationale for hypofractionation can be economic and logistic, benefiting both the patient and the radiotherapy sites by the reduced net machine use per patient. The difference in radiosensitivity between target and OAR is one of the two possible clinical incentives for hypofractionated treatment. In sites such as the prostate it has been shown that the targeted cancer is more sensitive to fractionation than the surrounding OAR. Accordingly, hypofractionated studies in prostate have been performed which show comparable tumor control probability (TCP) to conventional fractionation (Macías and Biete 2009).

The second clinical incentive for hypofractionation is the potential increase in TCP, achieved for higher doses per fraction. This treatment regimen has been utilized previously by studies in lung (Onishi et al. 2011) and liver (McCammon et al. 2009) and its application has been expanded to other sites in the abdomen such as the kidney (Chang et al. 2016) with excellent control rates.

While hypofractionated therapy is beneficial in the discussed sites, it is crucial that adjacent normal tissue and OAR are spared from the high fraction dose as much as

possible. The need for OAR sparing is especially true for ablative techniques, such as stereotactic body radiotherapy (SBRT). Inevitably, geometrical and statistical concepts such as PTV which purely serve the compensation of uncertainty, have to be questioned in this context as these concepts may not be valid for small numbers of fractions and are the main contributors to off-target doses, risking significant side effects in large volumes of normal tissue (Verellen et al. 2007).

1.3 On-board imaging for image guided radiotherapy (IGRT)

In order to gain confidence in the position of the target at the time of treatment, radiotherapy machines have been equipped with imagers. These on-board or in-room imagers enable the comparison of anatomy at the time of planning to anatomy at the time of treatment. Potentially detected changes are then either adapted on-line, i.e. for the current fraction, or off-line for the remaining treatment course. Many different modalitites have been presented, which differ in capability for spatio-temporal resolution, image quality, invasiveness and their interdependency with the treatment system.

1.3.1 X-ray based systems

Sourcing from radiology, X-ray based imaging systems for IGRT inherited all modi, i.e. projective, fluoroscopic and tomographic imaging, from their original domain.

Instrumentally, electronic portal imaging device (EPID) imaging is the simplest method, which records the transmission image of the treatment beam on the opposing side of the MV source. In radiology beam energies are optimized to generate optimal contrast. In radiotherapy, however, the treatment beam is designed to deposit energy at a reasonable depth in tissue and thus uses much higher energies. For this sub-optimal imaging regimen, large gradients in X-ray absorption are necessary to obtain reasonable contrast using EPIDs. Accordingly, transitions from soft-tissue to implanted radio-opaque fiducial markers or bone are used for position detection (Nederveen, Lagendijk, and Hofman 2000; Herman 2005). Recent EPID panels enable frame rates of 30 Hz and are thus able to track targets in the abdomen and thorax in real-time (Poels et al. 2014). Furthermore, recording the transmission field enables treatment quality assurance (QA) and dose reconstruction using EPIDs (Wendling et al. 2006). Since the transmission image is obtained *for free*, population studies of inter- and intrafraction motion can be performed without additional radiation dose from imaging (Heide et al. 2007; Kotte et al. 2007) .

Additionally added imaging beams are typically in the radiologic energy range (kilovoltage (kV)), mounted in a fixed position relative to the treatment beam. In the most common configuration, the kV imaging beam is orthogonally mounted on a coplanar therapy system, acquiring projections on a flat-panel detector. The main advantage of kV imaging is the improved contrast as compared to MV (Groh et al. 2002), allowing for better soft-tissue definition. Many studies investigated

the use of kV-imagers to track target positions either on fiducial markers (Shimizu et al. 2000) or on soft-tissue (Berbeco et al. 2005).

In addition to projective imaging, kV-imaging systems mounted on the rotating gantry can be used to reconstruct volumetric cone beam computed tomography (CBCT) scans. This can be used to obtain 3D images with CT-like contrast at the treatment site (Jaffray et al. 2002). While the technique has the advantage of obtaining 3D target positions in relatively good contrast, the image quality is inferior to diagnostic CT and is not suitable for on-line recontouring (McBain et al. 2006). In an attempt to bring diagnostic CT-quality to the treatment site, an in-room CT has been investigated (Uematsu et al. 1996), sliding the patient between CT and treatment unit.

1.3.2 Electromagnetic beacons

For projective X-ray, fiducial markers with high atomic number (Z) provide ideal contrast. Thus, in order to optimally detect a target position, a number of markers are implanted. The marker positions are then found by taking multiple projections to triangulate their position. However, as the position of most imagers is rigidly bound to the treatment system, the independent, concurrent use of treatment and imaging beam path is inherently impossible. Furthermore, for every acquired X-ray image, the patient is exposed to imaging dose, which should be kept as low as possible.

In order to account for these issues, electro-magnetic (EM) beacons were developed (Willoughby et al. 2006). The positions of these implanted transponders are detected by a receiver array near the treatment site. The EM-beacons are implanted in the same way as high-Z fiducial markers and offer an independent positioning, irrespective of the treatment machine geometry. Furthermore, dose exposure is not increased, due to the EM measurement. However, like X-ray fiducial markers, the technique solely returns rigid target shifts and is thus not able to resolve complex anatomy deformation.

Using appropriate implantation techniques, the beacons can be inserted in thoracic sites. Combined with read-out frequencies greater than 10 Hz, this allows for real-time target tracking of highly mobile lung tumors (Shah et al. 2013).

1.3.3 Ultrasound

In order to reduce the radiation exposure and increase image quality, ultrasound (US) imaging has been applied in radiotherapy (Lattanzi et al. 1999). One challenge of the reflective US is to achieve absolute positioning with respect to the treatment coordinate system. In order to relate the imaging coordinate system to the treatment coordinate system, transducers are either rigidly fixed to the table or referenced to the treatment coordinate system by means of infrared markers.

In the abdomen, Fuss et al. (2004) demonstrated target tracking using guidance structures (blood vessels) which could be easily identified in the US images and

are directly coupled to the actually tracked target. For prostate radiotherapy, US contrast enables the operator to distinguish OAR from the prostate, however, systematic position errors with respect to fiducial marker based positioning were observed (Lattanzi et al. 1999; Scarbrough et al. 2006). The use of US probes requires user-dependent pressure to be applied to the patient which can cause deformations of the volume of interest (VOI) and subsequent erroneous target position estimations (McGahan, Ryu, and Fogata 2004).

1.3.4 Online MRI guidance

Hitherto, in radiotherapy, the high image fidelity of MRI is mostly appreciated in pre-treatment diagnostics and planning. Due to the relatively complex signal generation and various read-out techniques (pulse sequences), the modality allows for the generation of a large variety of different soft-tissue contrasts. These can either be determined from nuclear magnetic resonance (NMR) tissue parameters, such as ρ, T_1, T_2 and χ, or encoded functional properties of tissue, such as oxygenation (blood oxygenation level dependent (BOLD)), diffusion (e.g., apparent diffusion coefficient (ADC)), flow and perfusion.

In contrast to projective techniques like CT and CBCT, the image data collection in MRI is based on volume selection and *Fourier* encoding using magnetic field gradients. By this means, VOIs can be sliced out, accessing e.g. single, non-projected 2D slices or whole 3D volumes in arbitrary directions (Haacke et al. 1999). Acquisition times in MRI depends mostly on the chosen acquisition volume and resolution. Thus, in order to cover processes with many different time constants, the dimensionality and size of the VOI can be changed to achieve the required acquisition times. This makes the imaging technique remarkably scalable.

The configurable soft-tissue contrast along with the option to achieve scalable sampling frequency makes MRI flexible enough for an on-line IGRT setting. It integrates the requirements for patient set-up (3D with soft-tissue contrast) and target tracking (rapidly updated target position updates with soft-tissue contrast) in one device.

Contrary to the projective X-ray techniques, MRI is based on a non-ionizing working principle. This allows for long imaging durations without penalties due to additional radiation dose. Nevertheless, a limit to specific absorption rate (SAR) is imposed. In order to stay within the limits, the radio frequency (RF) energy deposition is restricted by means of repetition frequency and amplitude of RF pulses. In this way, excessive heating from the imposed RF pulse energy can be prevented.

The advantages of MRI as a fully integrated positioning device in radiotherapy was identified by Lagendijk et al. (2002). In an attempt to integrate MRI into the therapy process, Karlsson et al. (2009) prototyped a solution sliding the patient between treatment machine and MR and referencing both machine coordinate systems using a docking device. Jaffray et al. (2014) also coupled MRI and linear accelerator (linac), using a rail-system to slide the entire MRI magnet into the

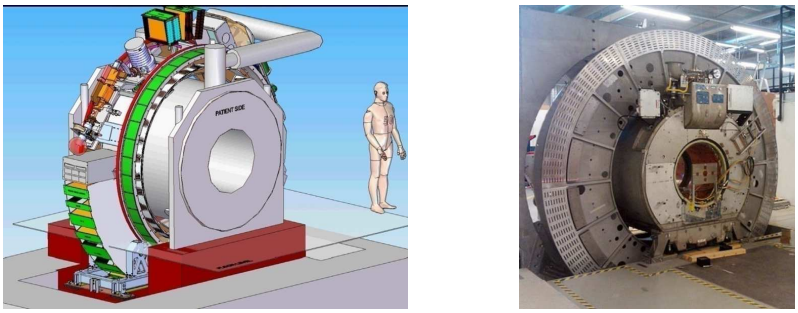

(a) **(b)**

Figure 1.3: *Utrecht* MR-linac design: the drawing in (a) displays the integration of the MRI with the linac: electric components reside in a low magnetic field region around the bore. (b) shows the production prototype as installed in *U1* at UMC Utrecht.

treatment room. Both systems can make use of the MRI for daily imaging and positioning based on anatomy changes, however, the patient needs to be physically moved between the two devices during the set-up process, which could possibly induce anatomy changes. Furthermore, the configuration does not allow for on-line imaging.

The physical integration of an MRI-machine and linac is technically and clinically challenging, as electric components of the beam generation (Lagendijk and Bakker 2000) and dose deposition within the subject (Raaymakers et al. 2004; Raaijmakers, Raaymakers, and Lagendijk 2005) are altered by the strong magnetic fields of MRI.

Nevertheless, several groups are investigating integrated designs. With *MRIdian*, ViewRay (Oakwood Village, Ohio, USA) marketed the first integrated system, comprising 3 rotating ^{60}Co sources radiating through a split-bore magnet with low 0.35 T field strength. On this system, the first patients were treated in 2014 (Mutic and Dempsey 2014). Several other research groups are investigating other set-ups, which mainly differ in the geometric orientation of the photon beam with respect to the main magnetic field, i.e. orthogonally or parallel (Keall, Barton, and Crozier 2014; Fallone 2014).

In this thesis, the MR-linac, a design evolving from a collaboration between University Medical Center Utrecht (Utrecht, The Netherlands), Elekta AB (Stockholm, Sweden), and Philips (Best, The Netherlands) is considered (Lagendijk et al. 2002; Raaymakers et al. 2009; Lagendijk, Raaymakers, and Vulpen 2014). The configuration consists of a magnet of diagnostic field strength of 1.5 T. The beam generation is placed on a gantry surrounding the magnet as shown in fig. 1.3. To avoid interference of the main magnetic field with the linac, active shielding coils in the magnet are driven in such a way to generate a low-field torus around the magnet, in which the beam generation components are situated (Overweg et al.

2009). The 7 MV flattening filter free (FFF) photon beam is shaped by a multi-leaf collimator (MLC) with 80 leaf pairs, traveling longitudinally, in parallel to a patient's caudo-cranial (CC) axis.

1.4 Motion compensation techniques

With the image guidance capabilities of IGRT, and specifically with on-line and real-time MRI on the MR-linac, adaptation of the treatment according to the actual anatomy becomes feasible. Ideally, the gradually decreased position uncertainty will translate into proportionally decreased PTV margins.

In current clinical practice, the most commonly applied position correction techniques for *inter-fraction* motion are couch adjustments according to pre-treatment imaging, such as CBCTs, kV, MV or EM transponders. These on-line adjustments reduce daily set-up errors significantly (Litzenberg et al. 2002).

Due to the limited dimensionality or contrast, current image-guided positioning techniques rely on the *rigid body assumption*, identifying the target as a non-deformable body with position $\boldsymbol{x}_{target}$ in space. The positioning and delivery is then performed on translations and rotations of that body, assuming that all anatomy is, at every time during treatment, moving rigidly with $\boldsymbol{x}_{target}$. Inevitably, however, deformations due to normal physiology, such as organ filling (fig. 1.1) or as a response to radiotherapy occur as the treatment progresses. Rather than by on-line repositioning, these non-rigid deformations can currently only be resolved by off-line adaptation strategies such as library of plans or regular replanning based on repeated CTs, promising large OAR sparing (Wu et al. 2009; Bondar et al. 2012).

During the set-up procedure, fast *intra-fraction* motion can impose a large uncertainty on the positioning, if it cannot be appropriately resolved by the pre-treatment imaging. Furthermore, residual motion occurring after the positioning cannot be corrected by table alignments. Therefore, treatment margins covering *intra-fraction* motion have to remain. Constrained by the breathing motion excursions, large PTVs are necessary to encompass the CTV for optimal target motion coverage throughout the therapy session. Especially for targets in thoracic and abdominal sites, margin concepts such as internal target volume (ITV) (ICRU 83 2010), mid-ventilation and mid-position (Wolthaus et al. 2006; Wolthaus et al. 2008) were designed.

Active motion compensation techniques challenge *intra-fraction* margin concepts, by actively modifying the treatment delivery in response to the currently detected situation of the anatomy in real-time.

Respiratory gating (Ohara et al. 1989) is the simplest approach to active motion compensation. Using imaging of either anatomic features or surrogates, the target position within the respiratory cycle is determined. The beam is then automatically turned on, when the target anatomy is in the relatively stable and

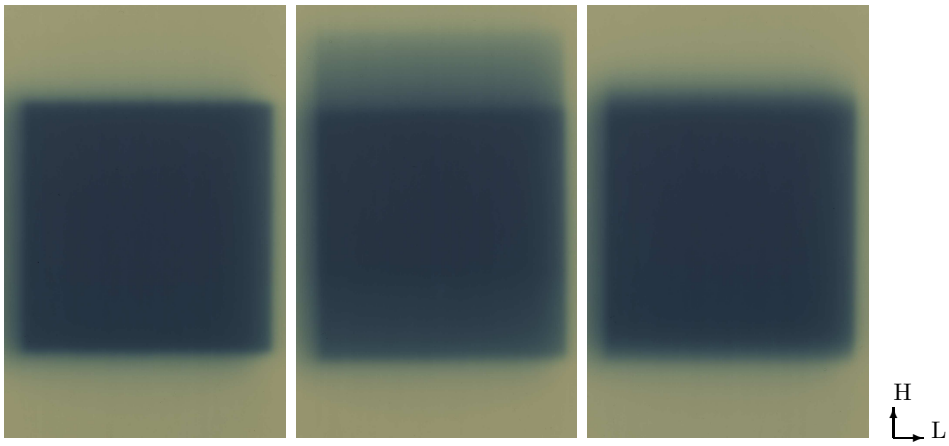

(a) **(b)** **(c)**

Figure 1.4: Gating experiment on a radiosensitive film. The blackening of the static film (1.4a) is smeared out when translating the film in head-foot direction (1.4b). Enabling gating (1.4c) collapses the diluted dose and retains a compact distribution.

motionless expiration state (gating window) and turned off when leaving that window. Figure 1.4 displays the dosimetric improvement of gated delivery with respect to continuous delivery. Respiratory gating has been applied using several position sources such as implanted markers or optical (surface) surrogates, which are assumed to be correlated to the internal motion (Gierga, Brewer, and Sharp 2005). The instrumental simplicity makes the technique interesting in terms of PTV reduction. However, as conformity increases due to small gating windows, total therapy time becomes longer. Thus an optimum has to be found between treatment efficiency and therapy duration.

In order to increase treatment efficiency, tracking using the on-board MLC of intensity modulated radiotherapy (IMRT) was devised (Keall et al. 2001). Using aperture morphing algorithms, MLC-segments are translated according to a shifted target position in real-time (Sawant et al. 2008; Tacke et al. 2010; Wisotzky, O'Brien, and Keall 2016). Similar to gating, the target position can be found using surrogates returning absolute target coordinates or whose motion are correlated to the motion of the target in pre-treatment 4D computed tomography (4DCT). First deliveries have been performed clinically, demonstrating the significant tissue sparing potential of MLC-tracking (Keall et al. 2014; Booth et al. 2016). MLC tracking relies on reactive translations of MLC leaves with relatively high mechanical inertia, which causes a delay between the target position and the responding aperture shift. Borrowing from first-order linear systems, this complex interplay is generally estimated as an averaged time delay.

Both gating and tracking have technical requirements and work under clear as-

sumptions. With current imaging techniques, the treated anatomy cannot be resolved volumetrically in sufficiently small time to resolve the respiration excursion. Thus both gating and tracking rely on the position information of single points extracted from low-dimensional images. On the analogy of couch adjustments, the target position is extrapolated onto the entire anatomy using the rigid body assumption. It is obvious that this assumption hardly holds for breathing excursions in the abdomen, e.g. by comparing the motion of both kidneys in fig. 1.2. Rigidly tracking on the right kidney will underestimate the motion of the left kidney. Similarly, for the lack of volumetric imaging, deformations cannot be accounted for during treatment using these techniques.

1.5 Thesis outline

This thesis investigates novel motion compensation and delivery methods enabled by on-line MR-image guidance. The following chapters cover imaging methods (**chapter 2**), integrated delivery and imaging methods (**chapter 3**) and conceptually pure delivery techniques (**chapters 4** and **5**).

In contrast to all other on-line imaging methods, MR-imaging enables the volumetric acquisition of images during the ongoing treatment fraction. Ideally, all anatomy changes can thus be recorded and reacted upon. The ability to register anatomic changes of different timescales is dependent on temporal resolution of the imaging method, thus, image acquisition time is a key figure. Relating to the fact that volumetric MRI is relatively slow, and that the acquisition can be sped up by reducing the image resolution, **chapter 2** establishes a correlation between the acquisition speed of 3D-MR images and the quality of motion estimation. For this purpose, 4D imaging series of volunteers are gradually downsampled, to emulate the quadratic decrease of acquisition time. To assess the quality, the deformation vector fields (DVFs) returned by the non-rigid motion estimation are then compared to the original estimation in representative regions and globally.

The on-board MRI of the MR-linac is versatile enough to rapidly switch between imaging modes. This feature is the basis of the investigation of **chapter 3**, which uses interleaved real-time and volumetric MRI. The described method employs the benefits of fast imaging in combination with the rigid body approximation for active motion compensation, i.e. gating. In addition, deformable anatomy changes during the treatment are recorded using interleaved volumetric (3D) images. Both imaging modes are combined to create a pipeline for automatic dose reconstruction of a fully respiratory motion compensated treatment on an MR-linac.

The MR-linac features an MLC derived from the Elekta Agility 160. In order to determine the tracking capability of the MLC and in further consequence of the MR-linac, **chapter 4** assesses the real-time tracking performance of the Agility. The responsiveness of the hardware is characterized using the (first order) delay determination. To evaluate real-world tracking performance, a camera-based research tracking pipeline was devised which was used to steer the MLC with respect to a target, moving in a physiologic manner.

Finally, errors induced by the non-ideal, higher-order response of the MLC-tracking system are discussed in **chapter 5**. The MLC-tracking system produces a complex mismatch between the image-determined target positions and the MLC-aperture position, depending on the target motion. While for the sake of simplicity, these effects are commonly integrated into a single time delay determined per machine as discussed in **chapter 4**, **chapter 5** assesses the current geometric mismatches in real-time. The subsequently inferred dosimetric effect of these mismatches is used to estimate tracking margins, optimally covering for the geometric errors of the current tracking situation in an on-line fashion. As a proof of concept, the dosimetric effect of tracking margins is assessed by tracking targets imposed with physiologic motion patterns.

CHAPTER 2

Fast motion detection using spatially undersampled MRI

The following chapter is based on:
Glitzner, M., Denis de Senneville, B., Lagendijk, J. J. W., Raaymakers, B. W., and Crijns, S. P. M. (2015a). "On-line 3D motion estimation using low resolution MRI.". In: *Phys. Med. Biol.* 60.16, pp. 301–310

Abstract

Image processing such as deformable image registration finds its way into radiotherapy as a means to track non-rigid anatomy. With the advent of MRI guided radiotherapy, intrafraction anatomy snapshots become technically feasible.

MRI provides the needed tissue signal for high-fidelity image registration. However, acquisitions, especially in 3D, take a considerable amount of time. Pushing towards real-time adaptive radiotherapy, MRI needs to be accelerated without degrading the quality of information.

In this paper, we investigate the impact of image resolution on the quality of motion estimations. Potentially, spatially undersampled images yield comparable motion estimations. At the same time, their acquisition times would reduce greatly due to the sparser sampling. In order to substantiate this hypothesis, exemplary 4D datasets of the abdomen were downsampled gradually. Subsequently, spatiotemporal deformations are extracted consistently using the same motion estimation for each downsampled dataset. Errors between the original and the respectively downsampled version of the dataset are then evaluated.

Compared to ground-truth, results show high similarity of deformations estimated from downsampled image data. Using a dataset with $(2.5\,\mathrm{mm})^3$ voxel size, deformation fields could be recovered well up to a downsampling factor of 2, i.e. $(5\,\mathrm{mm})^3$. In a therapy guidance scenario MRI, imaging speed could accordingly increase approximately fourfold, with acceptable loss of estimated motion quality.

2.1 Introduction

Recent developments enabled on-line MRI during radiotherapy (Raaymakers et al. 2009; Lagendijk, Raaymakers, and Vulpen 2014). In further consequence, new possibilities for elements in the feedback chain of adaptive radiotherapy (ART) arise: in contrast to currently available real-time positioning devices which provide only surrogate displacement data, MRI returns 3D anatomical information of both target volume and OAR.

After acquisition, 3D displacements need to be estimated from the dynamic volumes using image-based motion estimation algorithms (Oliveira and Tavares 2014). The displacements become 3D DVF which can be used as feedback variable for e.g. dose calculations or target tracking during intervention (Denis de Senneville et al. 2012). However, MRI is an inherently slow imaging modality and acquisition speed depends directly on image resolution. Additionally, MRI acquisition speedup is limited by both technical (gradient strength/noise bandwidth) and physiological (SAR, peripheral nerve stimulation (PNS)) constraints (Haacke et al. 1999). Similarly, model based acceleration techniques such as parallel imaging (Blaimer

et al. 2004) or compressed sensing (Lustig, Donoho, and Pauly 2007) are limited by the validity of their underlying model and the demand for reconstruction time.

The aspiration of this work is to investigate the impact of image resolution on the quality of motion estimation. Potentially, in case of obtaining comparable motion estimation with lower resolution, MRI acquisitions could be accelerated significantly. The gain in acquisition speed would enable applications which demand for high-frequency, real-time MRI, such as 3D target and dose tracking for ART.

2.2 Methods

2.2.1 Image data and imaging

As ground-truth for all experiments, 4D-MRI datasets depicting volunteers' abdomen were used. The use of volunteer data was chosen for the lack of satisfying synthetic phantoms for deformable image registration.

To avoid image modulation from breathing motion, respiratory gating was employed with a gating window of 5 mm using navigator echoes on the interface between lung and left liver-dome. Gating in end-of-expiration was chosen for its low expected residual breathing motion uncertainty for abdominal sites (Berbeco et al. 2006).

Since isotropic resolution is a prerequisite of the utilized image processing, the acquisition was tailored to acquire data with $(2.5\,\mathrm{mm})^3$ voxel size. k-space was filled in 3D manner in order to avoid malicious slice effects, such as slice overlap and inter-slice motion. Additionally, 3D k-space sampling yields higher signal to noise ratio (SNR) compared to sliced acquisitions.

The navigator triggered an echo planar imaging (EPI) readout with an EPI-factor of 21, $T_R/T_E/\alpha$=47 ms/9.8 ms/25°. Binomial pulses (1-2-1) (Hore 1983) were used for selective water excitation, concurrently suppressing the fat signal. Furthermore, moderate sensitivity encoding (SENSE) (P=1.5, S=1.5) was used to further accelerate imaging.

Volunteer	# of 3D dynamics	total scan duration
1	100	17 min
2	150	15 min
3	80	8 min

Table 2.1: Overview of the acquired amount of data for each volunteer.

The amount of data acquired for each volunteer is stated in table 2.1. From the individual total scan duration and the amount of 3D dynamics, it is possible to infer gating efficiencies for each volunteer: while for the first volunteer, an approximate amount of 6 images could be extracted per minute, scanning the other two yielded 10 images per minute, on average. During the scans the volunteers were breathing freely and were not commanded any breathing alteration.

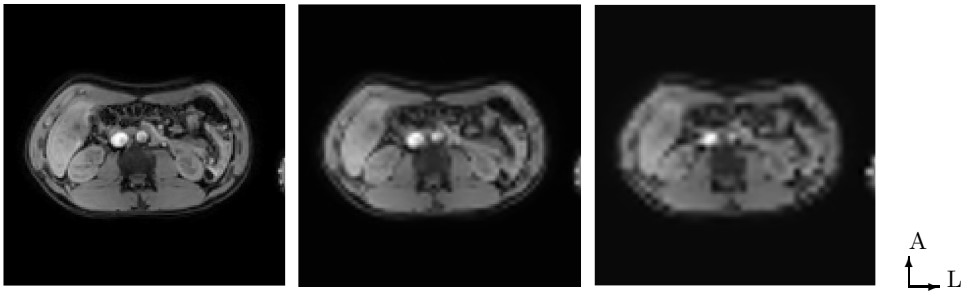

(a) original/$(2.5\,\mathrm{mm})^3$ **(b)** 2x/$(5\,\mathrm{mm})^3$ **(c)** 3x/$(7.5\,\mathrm{mm})^3$

Figure 2.1: Downsampled images resampled back into the original grid. Images exemplarily show the image information loss with higher downsampling factors

2.2.2 Image Processing

To simulate coarser sampling, downsampled data was synthetically generated using MATLAB's (The Mathworks, Natick, MA, USA) tri-cubic reconstruction kernels. The cubic kernel was chosen over linear interpolation to more closely resemble the ideal reconstruction kernel.

The original grid with $(2.5\,\mathrm{mm})^3$ voxel size was downsampled with factors k_i=[1.5, 2, 2.5, 3, 4] to simulate the loss of image content by coarser imaging. After downsampling, the data was again upsampled by the respective inverse factor in order to be able to compare data on a common (the original) grid (see fig. 2.1).

For the registration, baseline intensity variations throughout the imaging stack had to be removed. This was necessary because the T_1-weighted imaging sequence yields the brightest signal for blood. Consequently, since the cardiac cycle has a similar time scale as the dynamic imaging, these signal maxima appeared modulated in vicinal vessels. Accordingly, the median of the maxima found in all individual (magnitude) images was calculated. Subsequently, the intensity values were capped to the estimated median-max multiplied with a manually determined cut-off factor k_{cutoff}=0.8. Finally, the mean of every individual image dynamic was normalized to the mean of the reference image. This proofed to be more robust to grey level variations, compared to normalization to the dynamic range of the reference image.

2.2.3 Motion estimation

Motion throughout the imaging session was estimated with an implementation (Roujol et al. 2010) of non-rigid registration based on optical flow. As derived by

Horn and Schunck (1981), the optical flow's objective function is formulated as

$$\iiint_{\Omega} \left(\nabla I \cdot \mathbf{v} + I_t\right)^2 + \alpha^2 \left(\|\nabla v_x\|_2^2 + \|\nabla v_y\|_2^2 + \|\nabla v_z\|_2^2\right) dxdydz \tag{2.1}$$

The left side of the functional states that every spatio-temporal gray level variation ∇I and I_t is attributed to motion $\mathbf{v}=(\mathrm{v_x},\mathrm{v_y},\mathrm{v_z})^{\mathrm{T}}$. In addition, the regularization term on the right side is introduced to penalize sudden spatial changes of motion, which was validated for organ deformations (Østergaard Noe et al. 2008; Roujol et al. 2011). Accordingly, the unknown DVF is then extracted by minimization of eq. (2.1) with respect to $(\mathrm{v_x},\mathrm{v_y},\mathrm{v_z})^{\mathrm{T}}$.

The optical flow approach was chosen due to its initialization with only a single parameter (α in eq. (2.1)). In practice, α needs to be optimized only once for a particular contrast weighting. Additionally, the voxel-wise nature for the minimization of eq. (2.1) enables parallel processing using graphics processing units (GPUs) (Roujol et al. 2010). This, in turn, reduces the computation time of the algorithm which is favorable for applications with strict latency requirements.

For a complete quality analysis of the algorithm, the reader is referred to the work by Østergaard Noe et al. (2008) and Roujol et al. (2011) who assessed the accuracy of the method against gold standard displacements in 2D and 3D. According to their work, the regularization parameter was set to α=0.3. This value was chosen phenomenologically, in order to avoid instabilities in the motion estimation, which would lead to non-continuous estimations of the DVFs.

Motion was estimated between the reference image (first image dynamic) and every consecutive imaging dynamic. This process was repeated for every 4D stack of the respectively applied resampling factor with index i^{th}.

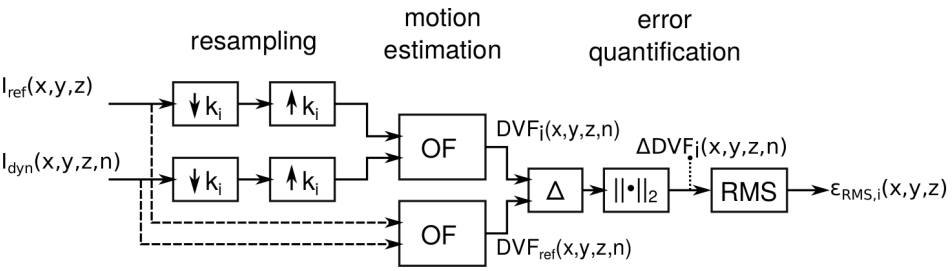

Figure 2.2: Evaluation workflow for motion estimation and error quantification: $\mathrm{k_i}$ indicates the respective factors for the resampling operators (↓,↑), OF means the motion estimation using optical flow. Subsequent $\mathrm{L_2}$-norm ($\|\cdot\|_2$), Δ and RMS operators work on a per-pixel basis. x, y, z are the spatial coordinates, n denotes the temporal index and i is the index for the individual downsampling factors.

2.2.4 Error assessment

As depicted in fig. 2.2, the quality of the motion estimation for the i$^{\text{th}}$ dataset was assessed by taking the differences between the DVF from resampled data and the DVF of the original data. However, the multidimensional, 4D vector fields

$$\mathbf{DVF}_i(\mathbf{x}, n) = \begin{pmatrix} v_x \\ v_y \\ v_z \end{pmatrix} (\mathbf{x}, n) \tag{2.2}$$

require integral metrics for convenient quantification of the differences. For clarity, the analyses are done solely in terms of absolute, component-wise differences, i.e. endpoint error (Baker et al. 2011),

$$\Delta DVF_i\left(\mathbf{x}, n\right) = \|\mathbf{DVF}_i\left(\mathbf{x}, n\right) - \mathbf{DVF}_{ref}\left(\mathbf{x}, n\right)\|_2, \tag{2.3}$$

with n denoting the temporal index of a 3D-dynamic.

Locally, two salient voxels were selected and analyzed over time for the longest dataset (volunteer 1 in table 2.1). Furthermore, for generating global statistics, we make use of the RMS which is applied on the absolute component-wise differences between two DVFs,

$$\epsilon_{RMS,i}(\mathbf{x}) = \sqrt{\frac{1}{N}\sum_{n=1}^{N} \Delta DVF_i(\mathbf{x}, n)}. \tag{2.4}$$

2.2.5 Data selection

In order to limit the sample size, comparatively mobile voxels including continuous and spontaneous motion events were elected for the global statistics.

Using linear regression, coefficients $\beta(\mathbf{x})$ were calculated for every voxel over time as

$$\underset{\alpha(\mathbf{x}),\beta(\mathbf{x})}{argmin} \left\{\alpha(\mathbf{x}) + \beta(\mathbf{x})n = \|DVF_{ref}(\mathbf{x}, n)\|_2\right\}. \tag{2.5}$$

Voxels showing values of $\beta(\mathbf{x})$ greater than 0.02 mm/dynamic were considered in the global statistics. In combination with the metric in eq. (2.5) this threshold extracts the elected dynamic voxels.

In addition to regression coefficients, the RMS of the DVFs could be a feasible quantifier of the target mobility in a voxel over time. However, for the chosen MR acquisition type, it did not prove feasible because of high false-positive rates. These were caused by the previously mentioned pulsation artifacts in the aorta and vena cava, randomly modulating the individual dynamics and thus the extracted DVF.

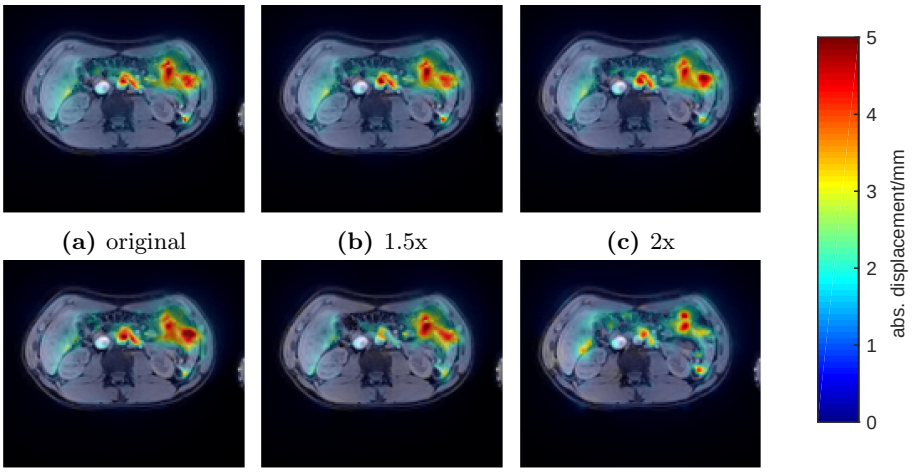

(a) original **(b)** 1.5x **(c)** 2x

(d) 2.5x **(e)** 3x **(f)** 4x

Figure 2.3: Absolute DVF in a selected slice of volunteer 1 for increasing downsampling (a-f). Qualitative similarity is apparent until downsampling with factor 2.5.

2.3 Results

Figure 2.3 shows a selected slice of the anatomy of volunteer 1 in the original image stack. A transparent overlay is applied onto anatomy, representing absolute displacement fields estimated in the last (100^{th}) imaging dynamic for either of the 6 (resampled) datasets.

Over the selected slice, the DVFs extracted from the individually resampled data appear visually congruent. The stretched displacement at the edge of the liver, next to the right kidney, appears consistently throughout all datasets and holds its structure up to a two-fold downsampling before it disintegrates.

Large deformations in the region between stomach and duodenum are prominent in all scenarios and retain shape. However, starting from factor 2.5, a visible blur is introduced to the DVF distribution. At 4x-downsampling, formerly prominent spots significantly decrease in motion magnitude.

In fig. 2.4, the inter-subject difference of mean motion β is apparent. While volunteers 1 and 3 have significant motion hotspots, the second volunteer's anatomy remains mostly steady throughout the scan duration. This reduces points which are in line with the inclusion criterion for the global RMS error statistics (β $>0.02\,\mathrm{mm/dynamic}$).

In fig. 2.4a, motion is predominantly observable in the intestine, whereas in fig. 2.4c, additional variations occurred at the rib cage. The generally static abdomen (kidneys, liver) verifies the gated imaging paradigm.

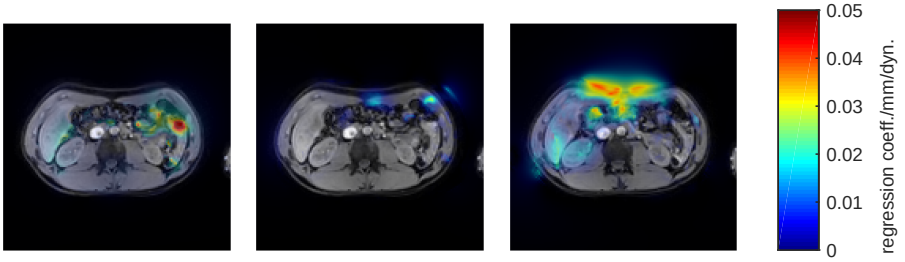

(a) Volunteer 1 **(b)** Volunteer 2 **(c)** Volunteer 3

Figure 2.4: Global error quantification: distribution of the extracted regression coefficients $\beta(\mathbf{x})$ over the anatomies of 3 volunteers.

According to what was observed qualitatively for volunteer 1 in fig. 2.3, quantitative error statistics in fig. 2.5 show the monotonous increase in RMS error with increasing undersampling. This effect occurs repeatedly for the other two subjects. In addition to the average error, higher moments of the error statistics increase equally, which leads to outliers $\epsilon_{\mathrm{RMS,i}}(\mathbf{x})$ >2 mm for downsampling with factors greater than 2.

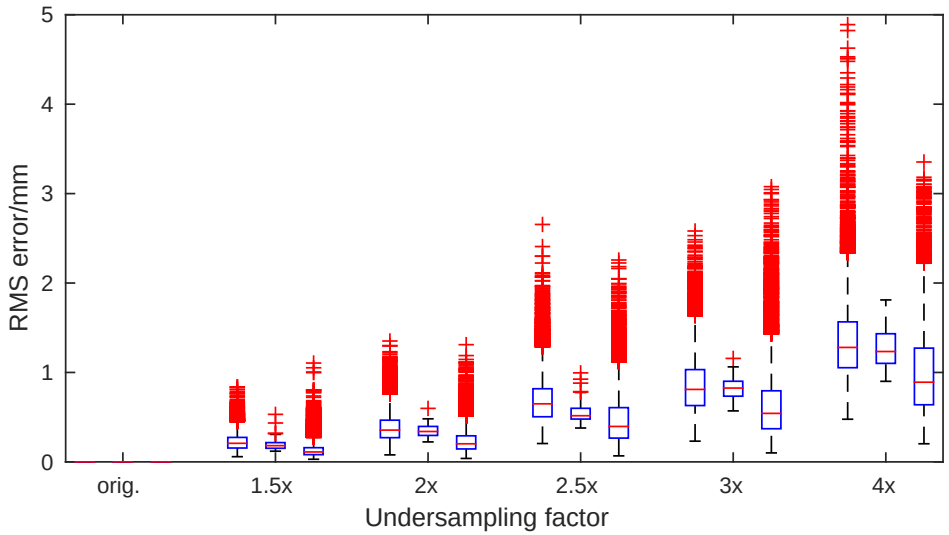

Figure 2.5: Global RMS error statistics: The boxplots illustrate the evolution of the RMS error within the elected voxels ($\beta(\mathbf{x})$>0.02 mm/dynamic) for the various resampling factors and volunteers. In each cluster the RMS error statistics from volunteer 1, 2 and 3 is plotted from left to right. For completeness, a boxplot for the original, non-resampled case was added.

In addition to the global statistics of many points (fig. 2.5), local performance evaluation is shown in fig. 2.6, illustrating the transient impact of downsampling. In the exemplarily selected point at the liver/kidney (fig. 2.6a), a constant drift

of about 2.5 mm/17 min is expressed over time. With coarser sampling starting from factor 3, the deformation appears greatly deteriorated with RMS errors proportional to magnitude. However, until factor 2.5, errors appear independent of the magnitude and stay lower than 1 mm.

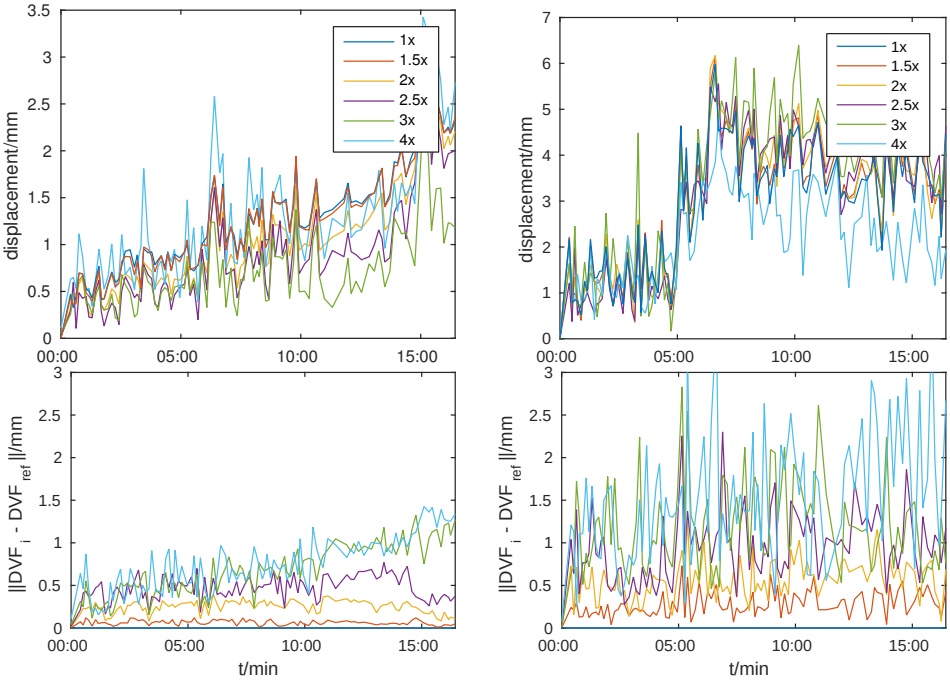

(a) liver/kidney transition **(b)** stomach/duodenum

Figure 2.6: Two manually selected points of interesting DVF evolutions in volunteer 1 for multiple downsampling factors. Absolute displacements (top row) and errors (bottom row) are shown.

Slightly different in the intestinal sample (fig. 2.6b), absolute errors start to exceed 1 mm already at factor 2.5. Undersampling with factors 3, as before, results in a greatly deteriorated DVF with errors exceeding 2 mm.

2.4 Discussion

Although removing image content by spatial downsampling, the used image registration algorithm was able to recover deformation fields to a high degree. In the synthetic experiments the most finely resolved data ($(2.5\,\mathrm{mm})^3$) served as ground-truth; with this, congruent DVF were able to be extracted up to a downsampling factor of 2 ($(5\,\mathrm{mm})^3$), with a global RMS deviations staying beneath 1.5mm. Exemplary samples of local points resulted in errors of less than 1mm.

This observation contradicts the idea that only images of diagnostic quality are

eligible for image registration purposes. Just the opposite, deformable image registration is much more data sufficient. Accordingly, imaging for the generation of displacement data is less demanding on image resolution than e.g. diagnostic imaging.

The fact that estimation of non-rigid motion requires spatial regularization is backing this hypothesis. Adding a spatial smoothness constraint (eq. (2.1), right side) enables stable motion estimation for regions with small image gradients (Bruhn, Weickert, and Schnörr 2005). Additionally, to suppress the impact of outliers, literature suggests the application of low-pass filters similar to those used in this work for image preconditioning in order to obtain better motion estimations (Barron, Fleet, and Beauchemin 1994). The simulated low-resolution MRI proposed here inherently implements both spatial (velocity) regularization and image low-pass filtering.

Most deformable image registration approaches work based on spatial regularization (Sotiras, Davatzikos, and Paragios 2013) and thus reflect the limited deformability of the anatomy. Hence, we believe that our conclusions can be translated for such approaches.

In real-time MRI, where image resolution can and must be traded off against imaging time, the proposed method could be used to significantly accelerate the acquisition. Using 2x spatial undersampling, the imaging time of about 3s for a $(2.5\,\mathrm{mm})^3$-acquisition could ideally be sped up fourfold while retaining the quality of extracted DVF. It is important to note that off-line resampling using the cubic reconstruction kernels is solely an approximation of the effect of an actual low resolution MR acquisition, due to accompanying changes in contrast and point spread function (PSF). However, in first approximation, the used reconstruction kernels are methodologically sound.

Combined with gated MRI, this technique enables fast 3D anatomy updates of abdominal volumes during the exhalation plateau. Used in an acquisition without respiratory trigger, i.e. free breathing, motion estimates would be less impacted by intra-scan artifacts (blurring) due to the shorter acquisition time. Due to respiratory gating in the exemplary data, only medium- to long-term drift motion in the abdomen was monitored. Thus, observed deformations within the body are limited and spatially smooth to a first approximation. The image registration is constrained equally, having a spatial smoothness regularization.

While the imaging and data conditioning was optimized for abdominal imaging for this paper, future studies will test the hypothesis for other body sites. Similar results are expected for slowly changing pelvic sites. However, results may be different when observing steep gradients in DVF over time, such as when regarding abdominal breathing excursions. This would put stress on the differences between the algorithmic and the physiologic constraints. Due to the lack of (real-time 3D) data being eligible to be considered as ground-truth, this scenario has not been considered in this work. A potential data source could be retrospectively binned

4D MRI data.

Possibly, the accepted error could be evaluated per site or per subject with pre-treatment assessments: high-resolution data could be acquired and gradually downsampled until remarkable sites exceed an error threshold. These assessment could take place under worst-case treatment conditions, e.g. during rectal or bladder filling in pelvic cases, in order to test the error for an extreme scenario. The reward would be a highly accelerated MRI acquisition, without relying on the further introduction of signal models.

2.5 Conclusion

This investigation showed, that deformation estimation on coarsely resolved images yields congruent results when compared to more highly resolved images. The examined insensitivity of nonrigid image registration to spatial downsampling can be used as a facility to speed up MRI acquisitions, specifically for real-time therapy guidance. Careful optimization between acceptable registration error and necessary imaging speed will however be necessary, since this trade-off cannot be made in an intuitive way.

2.6 Acknowledgements

The authors thank the ITEA (project 12026, SoRTS), the European Research Council (project ERC-2010-AdG-20100317, Sound Pharma) and Elekta AB (Stockholm, Sweden) for funding.

CHAPTER 3

MRI-based dose reconstruction for abdominal radiotherapy

The following chapter is based on:
Glitzner, M., Crijns, S. P. M., Denis de Senneville, B., Kontaxis, C., Prins, F. M., Lagendijk, J. J. W., and Raaymakers, B. W. (2015b). "On-line MR imaging for dose validation of abdominal radiotherapy". In: *Phys. Med. Biol.* 60.22, pp. 8869–8883

Abstract

For quality assurance and adaptive radiotherapy, validation of the actual delivered dose is crucial. Intrafractional anatomy changes cannot be captured satisfactorily during treatment with hitherto available imaging modalitites. Consequently, dose calculations are based on the assumption of static anatomy throughout the treatment. However, intra- and interfraction anatomy is dynamic and changes can be significant.

In this paper, we investigate the use of an MR-linac as a dose tracking modality for the validation of treatments in abdominal targets where both respiratory and long-term peristaltic and drift motion occur. The on-line MR imaging capability of the modality provides the means to perform respiratory gating of both delivery and acquisition yielding a model-free respiratory motion management under free breathing conditions. In parallel to the treatment, the volumetric patient anatomy was captured and used to calculate the applied dose. Subsequently, the individual doses were warped back to the planning grid to obtain the actual dose accumulated over the entire treatment duration. Ultimately, the planned dose was validated by comparison with the accumulated dose. Representative for a site subject to breathing modulation, two kidney cases (20 Gy target dose) demonstrated the working principle on volunteer data and simulated delivery.

The proposed workflow successfully showed its ability to track local dosimetric changes. Integration of the on-line anatomy information could reveal local dose variations -2.3 to 1.5 Gy in the planning target volume of a volunteer dataset. In the adjacent organs at risk, high local dose errors ranging from -2.5 to 1.9 Gy could be traced back.

3.1 Introduction

In an attempt for higher tumor control and better OAR sparing, new motion management strategies are gaining interest.

Traditionally, geometric margin concepts such as PTV, ITV (ICRU 83 2010) or mid-ventilation (Wolthaus et al. 2006) approaches for uncertainty compensation are used. Additionally, various active motion compensation methods have been recently investigated. Amongst them are guided patient positioning (Borst et al. 2007) as well as real-time beam gating (Shirato et al. 2000; Keall et al. 2006b) and tracking techniques (Keall et al. 2001; Crijns, Raaymakers, and Lagendijk 2012; Keall et al. 2014). While the former are mostly X-ray based imaging techniques, the latter are controlled by feedback variables extracted from external or internal surrogates, which ideally move in phase with the target volume (Ruan, Kupelian, and Low 2011).

Obviously, this in-phase condition is generally non-trivial to maintain, as system lag and imaging uncertainties introduce position errors (Keall et al. 2006a; Glitzner

et al. 2015c). Furthermore, using target surrogates for target tracking, motion of surrounding tissue in the beam path is entirely neglected. Additionally, although several authors have previously investigated dose tracking using surrogate signals (Poulsen et al. 2012; Ravkilde et al. 2014), the assumed (rigid) translations of the entire patient volume in phase with the surrogate signal are not physiologically sound.

The fusion of MRI diagnostics and radiotherapy treatment (Lagendijk, Raaymakers, and Vulpen 2014; Fallone 2014; Mutic and Dempsey 2014; Keall, Barton, and Crozier 2014) enables new options for motion management. With these combined modalitites, volumetric information is available on-line, i.e. during irradiation. This 3D information can serve for both target tracking (plan adaptation) and dose tracking (plan validation) (Kupelian and Sonke 2014). However, although MRI offers unprecedented soft-tissue contrast, volumetric imaging times are in the order of seconds. In the abdomen, real-time MRI in 3D is thus technically challenging, due to the high mobility of the abdominal organs (Langen and Jones 2001; Bussels et al. 2003) causing motion induced artifacts.

The aspiration of this work is to develop a technique to enable joint respiratory motion compensation and detailed 3D plan validation for the treatment of highly mobile abdominal organs using a MR-linac modality. Therefore, the presented method covers two aspects, i.e.

- apply respiratory motion compensation using responsive, real-time radiation gating on an internal surrogate (diaphragm) and
- recover the actual dose deposition by using 3D imaging over the active treatment time.

The unique combination of these fundamentals enables respiratory motion compensated, quality-assessed radiotherapy of abdominal sites. As a proof of concept, we evaluated two (virtual) kidney cases. This site was chosen because of its high mobility (Schwartz et al. 1994) during respiration and its expected benefit from stereotactic, hypofractionated treatments (Stam et al. 2013; De Meerleer et al. 2014) using an MR-linac. Planned and true dose depositions were calculated and compared off-line, integrating recorded treatment machine parameters, MR-acquired images and deformable image registration.

3.2 Methods

In this paper, rapidly sampled MR-navigator echoes were used to sample the respiration and restrict both the treatment beam and the image acquisition to the quasi-static expiration phase of the breathing cycle (Section 3.2.1). During the gating interval, delivery took place and fast 3D images were taken from the target region and its entire surrounding, i.e. all OAR in the beam path. Due to the respiratory motion compensation, the images contained solely cycle-to-cycle and

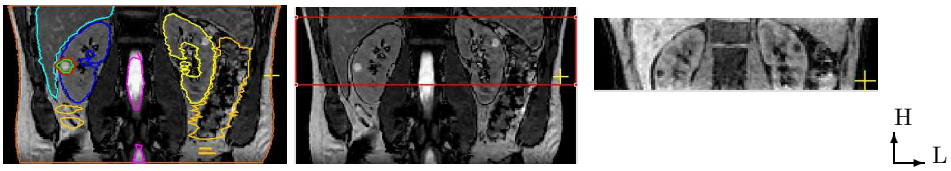

(a) Reference with delineations **(b)** Reference with treatment VOI **(c)** VOI during dynamic imaging

Figure 3.1: Planning images (a and b, 192x192x100, $(2\,\mathrm{mm})^3$) and intrafraction images (c, 144x144x36, $(2.5\,\mathrm{mm})^3$). Kidneys, liver, spinal cord, pancreas and bowels were delineated in addition to the GTV (green) and PTV (red). In the depicted anatomy, a benign cyst was delineated as target volume in the kidney. Anatomic directions: *head* (H) and *left* (L).

long-term variation, such as spontaneous and drift motion. Motion estimations (sections 3.2.2 and 3.2.3) extracted from the 3D imaging volumes are then used to recover anatomy variations in the course of treatment.

By continuous machine logging during the delivery of the generated plan (sections 3.2.4 and 3.2.5) the individual anatomies could be correlated with the machine state at every instance. Subsequently, applying Monte-Carlo (MC) dose calculations (section 3.2.7) on the pseudo-CTs of all individual anatomies (section 3.2.6), the actual delivered dose was reconstructed. In this way, an iterative dose accumulation was performed over the entire treatment time.

3.2.1 MRI acquisition

All imaging experiments were performed on a 1.5 T MRI machine (Ingenia, Philips Medical Systems, Best, The Netherlands) using a 28-channel torso array.

Two different MR pulse sequences were developed. Both of them employed navigator echoes (Wang et al. 1996) for respiratory gating in the exhale phase of the respiratory cycle. The navigator beam was placed on the right liver dome in order to maximize sensitivity to breathing excursions in CC direction.

The images from the first pulse sequence were used for generating the delineation reference (figs. 3.1a and 3.1b). The sequence consisted of navigator-gated, balanced turbo field echo (TFE) shots which were triggered in a narrow gating window of 2 mm (exhalation) in order to maximally suppress breathing artifacts. The shot length was approximately 250 ms including an $\alpha/2$-instance and 10 additional startup cycles to equilibrate the MR signal.

For fast 3D imaging during treatment, a second sequence was developed. It consisted of a navigator echo (5 mm gating window at exhalation) followed by a binomial, water-selective pulse. Subsequently, a multi-shot EPI readout was driven to increase sampling efficiency due to the long navigator and water-selective preparation. The long water-selective pulse was chosen to enhance the performance of

the image registration algorithm used (Section 3.2.2) which greatly benefited from suppressed fat signals.

The EPI readout is prone to geometric distortions due to susceptibility variations (Haacke et al. 1999). Therefore, the EPI train length was limited to 21 k-lines per shot to lower image acquisition times to around 3 s. Additionally, moderate SENSE was employed with undersampling factors of P=1.5 and S=1.5 in the anterior-posterior (AP) and CC phase encoding direction, respectively.

The sequence parameters were $T_R/T_E/\alpha$=47 ms/9.8 ms/25°. Typical gradient characteristics reported by the system were 192 T/m/s for the slew rates, 12 mT/m EPI-blip strength and 22 mT/m readout strength.

As VOI, a 10 cm thick transverse slab was selected (fig. 3.1c) to cover the lower liver/upper right kidney and thus the treatment volume and its surroundings with $(2.5\,\mathrm{mm})^3$ isotropic resolution.

3.2.2 Motion estimation

The isotropic 3D data MRI acquired during treatment is inherently suited for non-rigid image registration. In this work an implementation of optical flow-based registration (Roujol et al. 2010) was employed. The optical flow's objective function by Horn and Schunck (1981) reads

$$\iiint_{\Omega} \left(\nabla I \cdot \mathbf{v} + I_t\right)^2 + \alpha^2 \left(\|\nabla v_x\|_2^2 + \|\nabla v_y\|_2^2 + \|\nabla v_z\|_2^2\right) dxdydz \tag{3.1}$$

with I_t and ∇I being the temporal and spatial derivatives. Next to the motion estimation using image gradients (left side of eq. (3.1)) a data regularization term with a single parameter α penalizes sudden spatial changes of the estimated motion (∇v_x, ∇v_y, ∇v_z,). This regularization has been introduced for therapy guidance on mobile organs (Denis De Senneville, Mougenot, and Moonen 2007) and validated for organ deformations (Østergaard Noe et al. 2008). Apart from the single parameter, a further advantage is the performance of the optical flow algorithm when implemented on GPUs(Roujol et al. 2010). In this work the regularization parameter α, was set to a conservative α=0.3 to avoid non-continuous motion estimates (Roujol et al. 2011). Motion estimation of the continuously acquired volumes (144x144x36, $(2.5\,\mathrm{mm})^3$) took approximately 230 ms using a compute unified device architecture (CUDA) implementation on a Geforce GTX280 (NVIDIA, Santa Clara, CA, USA). The host computer was equipped with 2 central processing units (CPUs) (Penryn quad-core, Intel, Santa Clara, CA, USA) with 8 GB DDR3 SDRAM memory.

3.2.3 Gridding strategies

Generally, motion is estimated between two dynamics. One is the reference (I_{ref}) holding the initial anatomy. The second (I_n) is a version of the reference, which

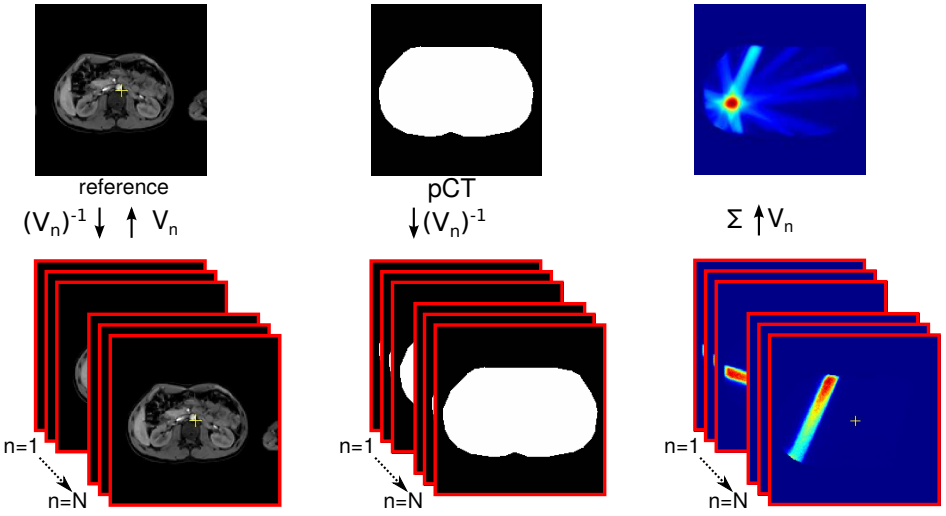

(a) DVF estimation **(b)** pCT generation **(c)** accumulation

Figure 3.2: DVF estimations (a) and regridding for pCT-generation (b) and dose accumulation (c).

underwent physiologic deformation.

Through motion estimation, a pull-back DVF $\mathbf{V}_i(\mathbf{x})$ is calculated for each dynamic image $\mathrm{I}_i(\mathbf{x})$, so that

$$\mathbf{I}_{ref}(\mathbf{x}) \simeq \mathbf{I}_n\left(\mathbf{x} + \mathbf{V}_n(\mathbf{x})\right). \tag{3.2}$$

This projects the content of the n^{th} dynamic's grid to the reference grid. In this work, this transformation is consequently used to warp dose deposited on an intermediate grid back onto the reference. It is accumulated on the reference grid (fig. 3.2c).

In contrast, the push-forward DVF is transforming content from the reference grid onto the dynamic grid, i.e.

$$\mathbf{I}_n(\mathbf{x}) \simeq \mathbf{I}_{ref}\left(\mathbf{x} + \mathbf{V}_n^{-1}(\mathbf{x})\right). \tag{3.3}$$

Herein, as illustrated in fig. 3.2b, this transformation is employed to construct dynamic CT data corresponding to the anatomical changes measured by the continuous 3D MRI as proposed by Boye, Lomax, and Knopf (2013).

Figure 3.3 depicts the difference between push-forward and pull-back DVF. The latter can be estimated by interchanging reference and dynamic images in the

motion estimation algorithm. Ideally, V_n and $V^{-1}{}_n$ are inversely consistent (Yang et al. 2008) such that

$$V_n(\mathbf{x} + V_n^{-1}(\mathbf{x})) + V_n^{-1}(\mathbf{x}) = 0. \tag{3.4}$$

In practice however, inverse consistency is generally not achieved by motion estimation algorithms. Therefore, inverse consistency was approximated by an iterative solution previously described in Heinrich et al. (2012) after calculating both push and pull DVF.

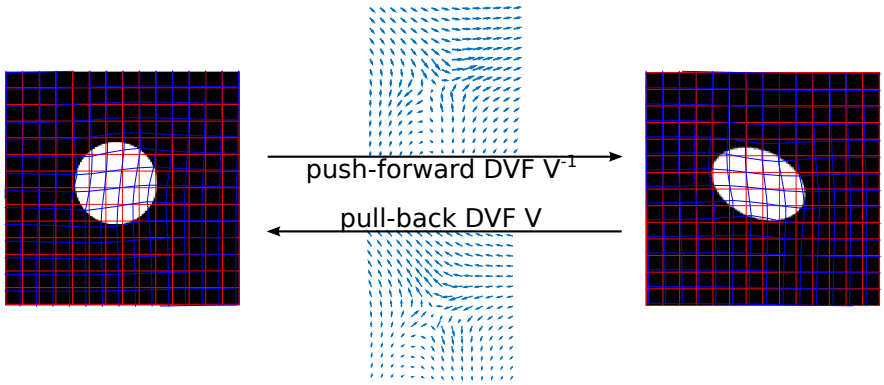

Figure 3.3: Warping between grids; The pull-back DVF provides the mapping back to initial grid of the circle. The inverse, V^{-1}, serves to reconstruct values from the circle's grid onto the ellipse's grid. Deformed indexing grids are shown in blue. Arrows indicate the direction of registration.

Site	Parameter	Value
GTV	D_{99}	$20Gy$
Kidney	D_{25}	$\leq 5Gy$
	D_{mean}	$\leq 8Gy$
Liver	D_{30}	$\leq 2.5Gy$
Bowels	D_5	$\leq 20Gy$
	D_{max}	$\leq 21Gy$
Stomach	D_4	$\leq 22.5Gy$
Spinal cord	D_{max}	$\leq 13Gy$

(a) Planning constraints

Parameter	Symbol	Value
Magnetic field	B_0	$1.5T$
Photon energy	E	$6MV$
Angle increment	$\Delta\Phi$	$24°$

(b) Physical parameters

Table 3.1: Planning constraints and parameterization for the created demonstration cases.

3.2.4 Plan generation

For this proof of concept, renal cell carcinoma (RCC) cases were generated by projecting fictional lesions into two volunteers' right kidneys. Additionally, both

kidneys, spinal cord, liver, stomach, pancreas and bowels were identified as OAR and contoured as seen in fig. 3.1a.

Based on constraints previously published by Stam et al. (2013), a plan was generated using the parameters in table 3.1a. The planned isocenter was set to the center of the tumor. The planning goal was to deliver 20 Gy to the target ($D_{99,GTV}$=20 Gy). A PTV-GTV margin of 2 mm was used. Fluence was optimized by in-house developed software employing an iterative approach by Ziegenhein et al. (2013) using pre-calculated beamlets for 15 equally space beam angles (see table 3.1b). The MC-based beamlet generation (Hissoiny et al. 2011a) took the MR-linac magnetic field B_0=1.5 T into account. Finally, step-and-shoot IMRT plans were created using the adaptive sequencing (ASEQ) method (Kontaxis et al. 2015a).

3.2.5 Plan delivery

The generated plan was delivered on a clinical linac emulator (Elekta AB, Stockholm, Sweden). The emulator featured an Agility 160 MLC (Elekta AB, Stockholm, Sweden) and a realistic model of the gantry and beam generation. During the entire delivery the machine parameters were logged with a sampling interval of 40 ms. This step was required to synchronize the exact machine status (leaf position, diaphragm position, gantry angle, dose rate) to the respective valid anatomy.

3.2.6 Pseudo-CT definition and generation

Generally, for the planning stage, information about the electron density is needed for the fluence optimization. However, since CT data acquisition of the (healthy) volunteers was not feasible, pCTs were synthesized. Based on a two-component model (Kerkhof et al. 2010; Stam et al. 2013), the body outline was extracted from the reference MR image. Subsequently the body was filled with the Hounsfield units (HUs) of water HU_{water}=0, while the surrounding air was set to the HU of air HU_{air}=-2900. This yielded the two-component pCT.

Subsequently, the push-forward DVF V^{-1} extracted from the dynamic data (fig. 3.2a) was used to transform the planning-pCT to the new dynamic grid (fig. 3.2b). This yielded a pCT for every dynamic, pCT_n.

3.2.7 Dose reconstruction

In this work, the navigator echo signal was used to trigger both imaging and the simulated treatment beam. For every pCT instance, an integration time ΔT_n is calculated by summing the valid gating intervals as depicted in fig. 3.4. Together with the machine parameters extraction described in section 3.2.5, a relation between momentaneous anatomy and machine state can be built up. Every acquired 3D volume is thus valid for one or more individual segment(s).

Subsequently, using a MC based dose calculation (Hissoiny et al. 2011b), dose was reconstructed on the respectively valid pCT_n using the individual segment from

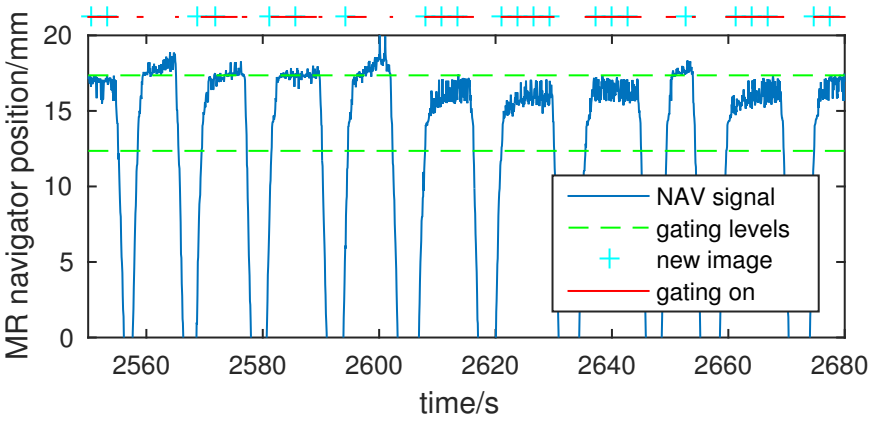

Figure 3.4: Navigator data with acceptance window: between the gating levels, imaging and beam generation becomes active. While the MR volumes are sampled, the plan segments are gradually delivered according to the treatment plan and the gating intervals. The high gating efficiency (≈53 %) is clearly recognizable.

the logged machine data (Luo et al. 2006). This produced dose maps D_n for all acquired anatomies, which were eventually warped back to the original grid using V_n (fig. 3.2c).

For MC calculations, a computer with two 12-core (Intel Xeon E5-2695, Intel, Santa Clara, CA, USA) CPUs and a Tesla K20c (NVIDIA, Santa Clara, CA, USA) GPU was used. One segment took approximately 15 s to calculate with a 5 % variance.

3.2.8 Plan validation

In order to validate the treatment plan, nominal (planned) doses were compared against the reconstructed doses. For error quantification, dose-volume histogram (DVH) points and integral parameters (D_{max}, D_{mean}, D_{min}) were calculated for the target volumes and the surrounding organs at risk. Furthermore, planning constraints were compared between planned and actual delivery. To pinpoint local differences, dose difference maps were calculated and the respective maximal, mean and minimal deviation was extracted.

3.3 Results

Figure 3.5 depicts representative transverse slices of the anatomic reference images for both cases. The simulated kidney lesions differ in location: case 1 is located in a more internal, inferior position as compared to case 2. The visual comparison between the planned dose on the rigid anatomy and the reconstructed dose based on variable anatomy shows no obvious deviation in the selected slice.

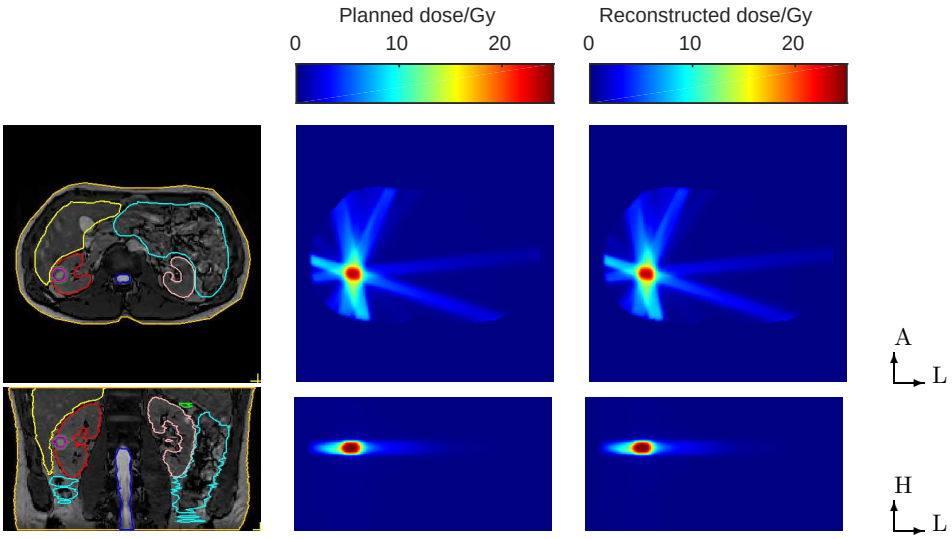

(a) Case 1

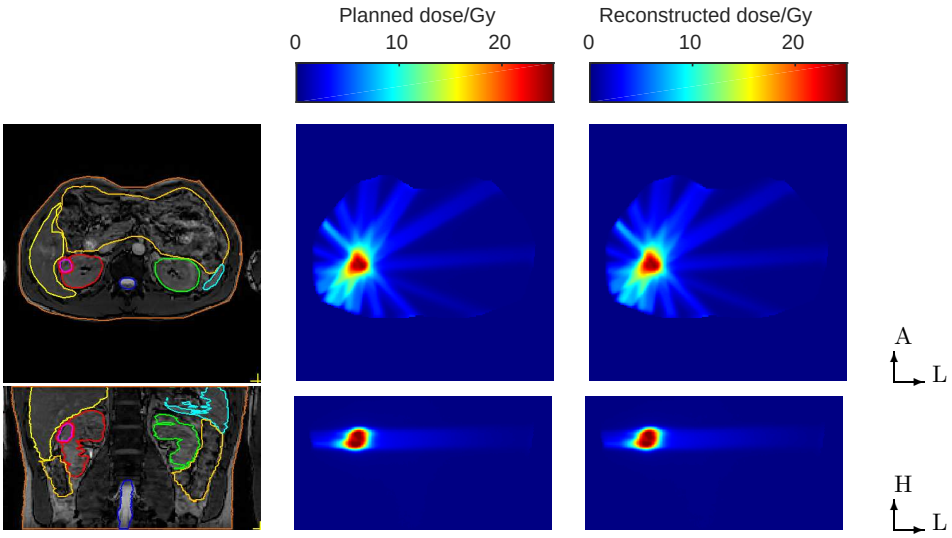

(b) Case 2

Figure 3.5: Cases 1 and 2 in figures (a) and (b), from left to right: selected slices (top row: transversal, bottom row: coronal) in delineated anatomy, the planned dose distribution and the accumulated dose incorporating the moving anatomies. Anatomic directions: *anterior* (A), *head* (H) and *left* (L).

The global DVH-points shown in table 3.2 show similar features: all dose constraints defined in table 3.1a were satisfied both with the static planning case and after validation using the variable anatomy. Only kidney-D_{25} of case 2 is close to its maximum dose of 5 Gy. However, neither in the nominal nor in the reconstructed dose, the constraint is significantly violated and is therefore considered as plan compliant.

For case 1 local differences in table 3.2a show little variation when incorporating moving anatomy. This is consistent with the global DVH point for this case, showing only little differences between static and moving anatomy.

As discussed later, the parameters for the second case (table 3.2b) reveal discrepancies between the DVH points and the local differences. While the differences in the DVH of the PTV are only around 1 %, local underdosage exceeds 2 Gy with overdosages up to 1.5 Gy in the PTV.

As the most vicinal OAR, the statistics for the liver show a similar pattern. Although DVH points do not suggest changes in the actually deposed anatomy, local variations are significant, ranging from -1.3 to 1.9 Gy.

These differences in the liver-kidney region are equally prominent in the difference images of fig. 3.6b. As the primary source for the dose alteration, the beam at 216° (*posterior-anterior*) induces high difference gradients in the kidney-liver transition region. Both underdosage and overdosage in this region is caused by anatomy variations for this beam angle. These variations are especially visible in the transverse and coronal dose profiles in fig. 3.6b and are correlated with the internal motion between kidney and liver. At the exiting portal of the same beam, the exit dose changed due to a variation of the diaphragm position. In comparison, fig. 3.6a shows the same exit dose effects for the posterior entering beams. However, effects in the vicinity of the GTV are minor.

3.4 Discussion

Radiotherapy of mobile sites requires treatment validation. This work pursues a technique for on-line dose tracking for the treatment of abdominal sites using the on-line imaging capabilities of an MR-linac. We successfully devised and implemented a treatment pipeline capable of reconstructing the dose deposition in kidney cases using on-line MR imaging during treatment. By use of fast MR-navigator echoes, the abdomen was decoupled from breathing excursions. Entering the gating window triggered both treatment beam and 3D image acquisition, the image covering an entire transverse slab around the target volume.

The continuous 3D acquisitions can be utilized manifold: Firstly, deposited dose can be calculated integrally for an entire fraction. This enables the option to adapt subsequent fractions according to the intermediate deposition. Also, particularly erroneous parts of delivery causing high dose differences can be traced back in retrospect. Delivery elements which turn out to systematically induce large errors

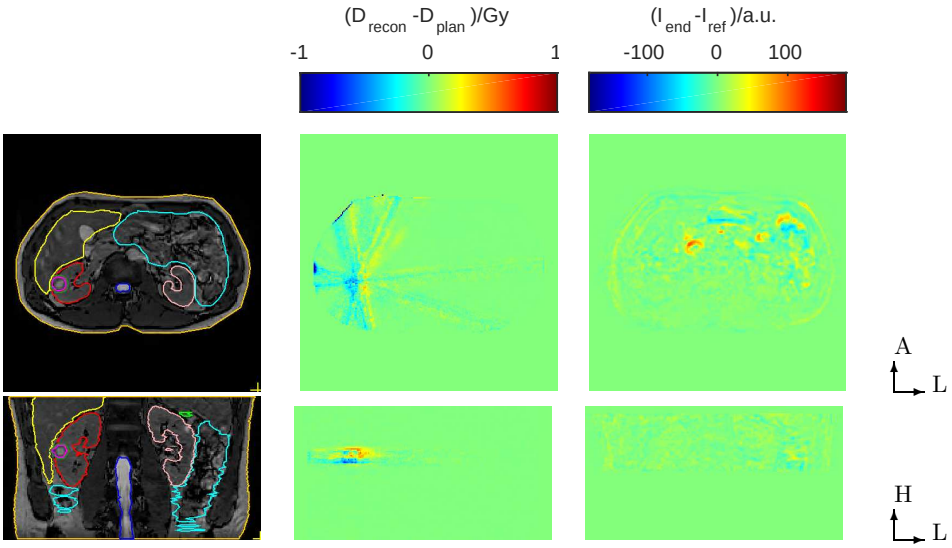

(a) Case 1

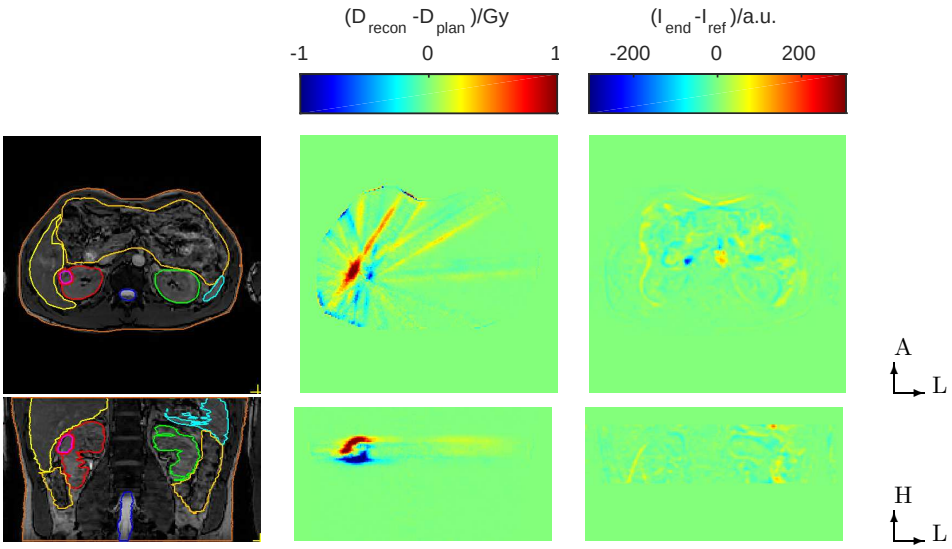

(b) Case 2

Figure 3.6: Visual dose and image comparison of both cases (a and b). Left: anatomic orientation, middle: dose differences between reconstructed delivery and planning (D_{recon}-D_{plan}), right: difference between final and reference anatomy (I_{end}-I_{ref}), indicating the anatomy displacements over the treatment time in transverse (top row) and coronal (bottom row) planes.

in the plan validations can be identified and avoided for the sensitive population.

Secondly, when performing real-time accumulation after each imaging volume, local dosimetric or geometric errors at OAR can be used to trigger exception handling based on predefined levels.

The two cases processed in this work suggest that inter-patient variations are significant. While for case 1 no relevant dose differences were found locally, the second case revealed considerable local differences. Most remarkably, the integral DVH points did not significantly change at any time. This suggests that integral measures (γ, DVH points) alone are insufficient to characterize the validity of the plan outcome in a dosimetric sense.

Evidently, using on-line 3D MR imaging for the dose reconstruction renders it obsolete to model anatomic motion as a bulk translation according to a surrogate signal, as described by Poulsen et al. (2012).

Compared to EPID dosimetry, as described for example by Lin et al. (2012), the presented method resolves the entire beam path, rather than projecting back over an integral pathway. Additionally, projective dosimetry relies on previously (retrospectively) acquired patient anatomies. Using EPIDs in the static B-field of an MR-system, the dosimetry would heavily rely on MC-generated models of the beam trajectory, in order to account for electron return effects (EREs) (Raaijmakers, Raaymakers, and Lagendijk 2005) at tissue-air boundaries.

With the proposed pipeline, anatomy information is available on-line. Using the gated approach, anatomical drifts and other cycle-to-cycle variations, e.g. as shown by Seregni et al. (2006), do not corrupt the anatomical accuracy. Instead of inferred data from a retrospective 4D model as discussed by Sawant et al. (2014), true 3D data is sampled. This yields accurate data representing the momentary state of anatomy.

For a potential clinical deployment, the influence of target motion within the gating window has to be taken into account as shown by Stam et al. (2013). This can be accomplished by trading off gating window width against a residual motion margin. Since the EPI readout in the imaging sequence is prone to geometric distortions, investigations of distortion correction methods will be necessary. The latter were already addressed by e.g., Dragonu et al. (2009) for real-time high intensity focused ultrasound (HIFU) interventions. Moreover, to overcome image distortions, high-bandwidth fast field echo (FFE) sequences will be considered, despite their contrast and artifact behavior, which have an adverse effect on the image registration.

The gating efficiency was estimated to around 50 % for both cases, which would translate into an approximate two-fold treatment time. To address the problem of gating window drifts, we are currently evaluating gating level adaptation schemes. Additionally, ways to validate the dose reconstruction workflow itself are currently under investigation at our institution. Furthermore, ongoing efforts are translating

the current off-line implementation into an on-line pipeline, deployable on the MR-linac.

3.5 Conclusion

We successfully implemented and demonstrated a workflow to perform a respiratory motion compensated, fully reconstructed treatment for abdominal site using the on-line imaging capabilities of an MR-linac. This proof of concept is a step towards the clinical implementation of dose validation using such a device.

Acknowledgements

The authors thank the ITEA (project 12026, SoRTS), the European Research Council (project ERC-2010-AdG-20100317, Sound Pharma) and Elekta AB (Stockholm, Sweden) for funding.

Volume	Dose	static	dyn	diff (%)
GTV	D_{99}*	19.670	19.490	−0.9
PTV	D_{max}*	26.230	26.460	0.9
	D_{min}	11.890	12.110	1.9
	D_{mean}	21.580	21.580	0.0
	ΔD_{max}		0.6	
	ΔD_{min}		−0.7	
	ΔD_{mean}		0.0	
Kidney	D_{max}	25.000	25.110	0.4
	D_{min}	0.080	0.070	−12.5
	D_{mean}*	2.010	2.030	1.0
	D_{25}*	1.216	1.268	4.3
	ΔD_{max}		0.6	
	ΔD_{min}		−0.6	
	ΔD_{mean}		0.0	
Liver	D_{max}	20.400	20.470	0.3
	D_{min}	0.000	0.010	−
	D_{mean}	0.570	0.570	0.0
	D_{30}*	0.191	0.192	0.5
	ΔD_{max}		0.4	
	ΔD_{min}		−0.7	
	ΔD_{mean}		0.0	
Bowels	D_{max}	1.800	1.760	−2.2
	D_5*	0.177	0.179	1.1
Stomach	D_4*	0.033	0.033	0.0
Spinal cord	D_{max}*	1.390	1.430	2.9

(a) Case 1

Volume	Dose	static	dyn	diff (%)
GTV	D_{99}*	20.370	19.990	−1.9
PTV	D_{max}*	26.760	26.490	−1.0
	D_{min}	13.810	13.890	0.6
	D_{mean}	21.990	21.750	−1.1
	ΔD_{max}		1.5	
	ΔD_{min}		−2.3	
	ΔD_{mean}		−0.2	
Kidney	D_{max}	24.530	24.290	−1.0
	D_{min}	0.080	0.080	0.0
	D_{mean}*	3.650	3.570	−2.2
	D_{25}*	5.080	4.991	−1.8
	ΔD_{max}		1.2	
	ΔD_{min}		−2.5	
	ΔD_{mean}		−0.1	
Liver	D_{max}	19.990	20.330	1.7
	D_{min}	0.020	0.020	0.0
	D_{mean}	0.890	0.910	2.2
	D_{30}*	0.221	0.233	5.4
	ΔD_{max}		1.9	
	ΔD_{min}		−1.3	
	ΔD_{mean}		0.0	
Bowels	D_{max}	17.470	16.870	−3.4
	D_5*	2.423	2.419	−0.2
Stomach	D_4*	0.087	0.087	0.0
Spinal cord	D_{max}*	1.670	1.650	−1.2

(b) Case 2

Table 3.2: DVH points and difference statistics for treatment validation of both cases. For each VOI, DVH-points (D_{xx}), spatial integral parameters of absolute doses (D_{max}, D_{mean}, D_{min}) and voxel-wise differences (ΔD_{max}, ΔD_{min}, ΔD_{mean}) are shown. Planning constraints are marked with an asterisk (*).

CHAPTER 4

Tracking performance of the Elekta Agility 160 MLC

The following chapter is based on:
Glitzner, M., Crijns, S. P. M., Denis De Senneville, B., Lagendijk, J. J. W., and Raaymakers, B. W. (2015c). "On the suitability of Elekta's Agility 160 MLC for tracked radiation delivery: closed-loop machine performance". In: *Phys. Med. Biol.* 60.5, pp. 2005–2017

Abstract

For motion adaptive radiotherapy, dynamic multileaf collimator (dMLC) tracking can be employed to reduce treatment margins by steering the beam according to the organ motion.

The Elekta Agility 160 MLC has hitherto not been evaluated for its tracking suitability. Both dosimetric performance and latency are key figures and need to be assessed generically, independent of the used motion sensor.

In this paper, we propose to use harmonic functions directly fed to the MLC to determine its latency during continuous motion. Furthermore, a control variable is extracted from a camera system and fed to the MLC. Using this setup, film dosimetry and subsequent γ statistics are performed, evaluating the response when tracking MRI-based physiologic motion in a closed-loop.

The delay attributed to the MLC itself was shown to be a minor contributor to the overall feedback chain as compared to the impact of imaging components such as MRI sequences. The MLC-latency showed a linear phase behaviour in continuously dynamic applications, which enables a general MLC-characterization. Using the exemplary feedback chain, dosimetry metrics showed a vast increase in pass rate employing γ statistics.

In this early stage, the tracking performance of the Agility using the test bench yielded promising results, making the technique eligible for the translation to tracking using clinical imaging modalities.

4.1 Introduction

In an attempt to further limit radiation exposure of healthy tissue, real-time tracking has been evolved recently. Potentially, using tracking, the PTV can be decreased significantly. Treatment margins added to account for set-up and motion-induced misalignments can be compensated using IGRT, retaining high conformity in the actual tumor volumes with intensity modulated techniques (Giraud et al. 2006). A general review of IGRT can be found in Ruan, Kupelian, and Low (2011).

For MLC tracking, several concepts have been demonstrated for main manufacturers of linac hardware (Tacke et al. 2010; Falk et al. 2012). Multiple position extraction techniques are utilized to assess tumor motion indirectly via surrogates, or directly via fiducials. In order to obtain geometric organ positions, mostly surrogate based positioning has been in use, amongst them optical positioning systems (Sawant et al. 2009) and electromagnetic transponders (Smith et al. 2009) (*Real-time Position Management* (RPM) and Calypso, Varian Medical Systems Inc., Palo Alto, CA, USA). Recently, the first clinical application of MLC-tracking utilized the latter modality on a prostate case (Keall et al. 2014). Furthermore, tracking signals have been extracted from kV and MV imaging data (Berbeco et al. 2005; Cerviño et al. 2009) and recent studies also investigated MLC-tracking

using real-time feedback from MRI (Crijns, Raaymakers, and Lagendijk 2012; Yun et al. 2013).

To this day, the performance of real-time MLC tracking using Elekta Agility 160 MLCs (Elekta AB, Stockholm, Sweden) has not yet been explored. Only virtual tracking using initial synchronization between the delivery and a motion platform has been reported (Davies et al. 2013).

The aspiration of this paper is to assess the system performance of the MLC in a generic sense. For the application in an integrated tracking modality, knowledge of the time delay of an MLC is fundamental, as it is the most sensitive parameter determining the geometric error in motion compensation (Poulsen et al. 2010; Ruan 2010), parameterization of prediction filters and retrospective dose accumulation. The relative contribution of the MLC is needed for evaluating its feasibility in a feedback chain with clinical components such as in an MR-linac system developed in our institution (Raaymakers et al. 2009; Lagendijk, Raaymakers, and Vulpen 2014). Due to the bandlimited character of physiologic motion, the time shift between aperture application and mechanic execution is determined in a physiologically reasonable continuous motion regime. To legitimate a general definition of the delay, the MLC is tested for linear phase behaviour in this range of harmonics.

Additionally, an optical feedback chain consisting of fast imaging, image processing and 1D aperture adaptation is prototyped which serves as a test bench for the extraction of timing characteristics of the MLC and for actual dosimetry. It can easily be adapted to other control variables, potentially sourced from other imaging techniques such as from MRI, electromagnetic transponders or optical positioning surrogates. The final endpoint being radiation depositions in clinical applications, the dosimetric impact of the actual feedback loop is measured in response to a physiologic motion scenario. Tracked and untracked dose maps are compared with integral quantifiers, i.e. tight-radius γ-analysis and relative dose histograms, in order to rate the tracking performance without regarding for uncertainties such as from planning or from positioning.

4.2 Methods

The methods are divided into a general part comprising hardware and evaluation (sections 4.2.1 to 4.2.4) together with the description and measurements of the elements involved in open- and closed-loop MLC control (sections 4.2.5 to 4.2.7).

4.2.1 MLC characteristics

For all experiments, Elekta's Agility 160 MLC as part of a clinical Axesse (Elekta AB, Stockholm, Sweden) linear accelerator is used. The Agility features 80 leaf pairs with 5 mm width at isocenter and dynamic diaphragms to limit the aperture perpendicular to leaf travel direction. For reasons of data presentation and evaluation, an aperture of 20x40 mm^2 was applied, by separating all leaves by 40 mm.

The arising gap is then limited to 20 mm using the diaphragm. The leaf motion is in CC direction, parallel the longer side of the rectangular aperture. The head is thus rotated to 90°. The aperture width of 40 mm is chosen to yield a global dose plateau for each measurement, i.e. a point of permanent irradiation. This is needed to obtain a reference measurement for the relative dosimetry, detailled in section 4.2.3.

4.2.2 Tracking components

The feedback loop comprised an optical path for object detection and a control loop which shifts the aperture in response to object motion. The optical path located the position of a binary image (target) mounted on a linearly (1D, along leaf motion direction) moving object. The target image contained a contrast-rich structure with sharp gradients (see fig. 4.1b) in all directions in order to make it locatable by the image processing explained below. The camera was positioned in such a way, that the target image was moving in a fixed imaging plane perpendicular to the camera's optical axis. Secondly, the control loop polled the extracted object's position continuously and applied it in form of a rigid aperture translation (again 1D in leaf motion direction) to the MLC system.

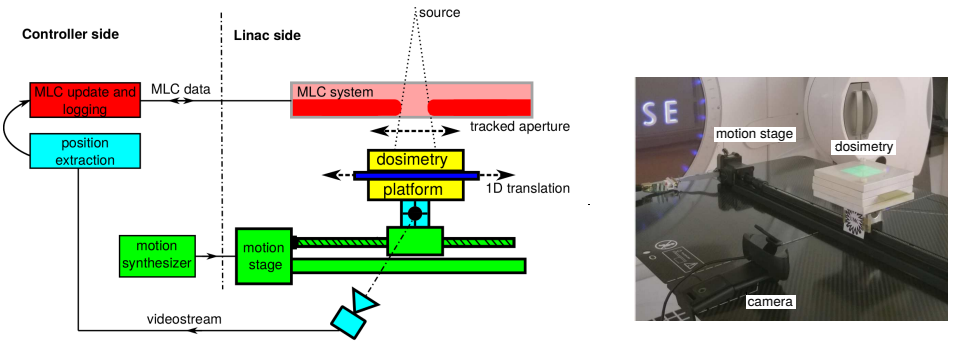

Figure 4.1: Schematic a and picture b of system components of the feedback loop, information flow and motions: The controller is commanding the MLC system and retrieving leaf positions from it. The position extraction locates the object position by processing a video stream from a camera. 1D motion is synthesized and sent to the motion stage which translates the dosimetry set-up and the attached target. See text for details.

The in-house developed tracking software served two purposes, depicted in fig. 4.1: image acquisition and processing and commanding the MLC. In order to obtain the position of the tracked object, a camera (C930e, Logitech, Apples, Switzerland) presents a videostream (640x480, 30 Hz) containing the marked object and passes the stream to the image acquisition module. The camera was accessed using the computer vision library OpenCV (Bradski 2000). In order to obtain a reliable

position extraction of the marked object by the subsequently described tracking algorithms, auto-focus features are disabled on camera-side.

In feedback experiments, the captured images are passed to a processing module without further conditioning. The processing module extracts the pixel location of the marker based on a fast in-house minimum output sum of squared error (MOSSE) filter implementation (Bolme et al. 2010; Crijns et al. 2012), tuned for working in a 64x64 local region. Initially, before each experiment, geometric reference is established by a homing procedure in combination with the motion stage described below and a mean-free cross-correlation filtering. The latter extracts the position of an object marked with a known pattern from the captured images. Because of the relative slowness of this tracking method compared to the MOSSE filter, the correlation is only applied during homing. This algorithm transistion is necessary due to the local nature of the MOSSE filter; the detection region needs to be determined by the global cross-correlation algorithm first. In order to compare the processing performance, the runtimes of both algorithms were measured. Both filters operated on pixel pitch of 0.3 mm/px. The change in object position extracted by the image processing module were used as the control variable for the 1D closed-loop aperture translation and the leaf positions of the translated aperture were applied to the Agility MLC control system via Ethernet with a cycle time of 40 ms. Concurrently, the leaf positions provided by the MLC control system were continuously recorded.

All software was run via a Debian operating system on a computer equipped with 8 GB of memory and a 3.4 GHz quad-core CPU (Core i5-2400, Intel, Santa Clara, CA, USA).

4.2.3 Dosimetry

The dosimetric platform is sketched in fig. 4.1 showing a film sandwiched between two layers of water-equivalent solid build-up material of 2 cm thickness and a square surface of 10x10 cm^2 each. Relative dosimetry is performed using the radiosensitive GafChromic EBT3 film (Ashland Inc., Wayne, NJ, USA), with dimensions of about 10x4 cm^2. The longer side of the film is parallel to leaf travel direction and thus to the direction of motion.

Generally, the film set-up moved in a plane of 1 m source-to-axis distance (SAD) at isocenter. The object holding the film is referenced relative to the isocenter. In other words, an object in initial position (x=0 in fig. 4.2a) is under an isocentric aperture. With each irradiation, a dose of D=1000 MU is delivered using a constant dose rate of $\dot{D}$=400 MU/min at 6 MV.

For planar (2D) dosimetry, the irradiated film is scanned using an Epson 10000XL flatbed scanner (Seiko Epson Corporation, Suwa, Japan). An automatic alignment method centers and rectifies the dose images using rigid transformations.

For 2D evaluation, γ-statistics (Low et al. 1998) and dose difference test were used. The 2D dose distribution are transformed to relative dose maps ranging between

noise floor and dose plateau. To establish a stringent quantifier for the synthetic experiments, a tight γ-pass radius of (1 %/1mm) was set. The dose-window to be evaluated is between 10 % and 100 % to reject low-dose regions, which we consider unimportant for rating the tracking performance.

4.2.4 Phantom motion

Motion is induced using a home-built 1D translating stage. The linear positioning system (LPS) consists of an MDrive 17 (Schneider Electric Motion, Marlborough, CT, USA) driving a stage via a threaded rod (fig. 4.1, green elements). The controller and drivers of the MDrive 17 are integrated and controllable via RS422. The motion stage carried the dosimetry set-up (cf. section 4.2.3) along with the optical target, detectable by the tracking algorithm (see fig. 4.1b). In-house developed software was used to feed the stage with positioning data. The positioning data in the experiments were of two kind: synthetically generated sinusoidal curves and motion extracted from a temporally resolved liver position over multiple breathing cycles (see fig. 4.2).

Sinusoids are applied to the motion stage for determining the overall closed loop response delay. Staying within a pseudo-continuous domain for the tracking system (the control variable does not strongly feature discrete step-behaviour), a parameterization of (A, T)=(15 mm, 6 s) was chosen, where A is the amplitude and T the duration of a sinusoid.

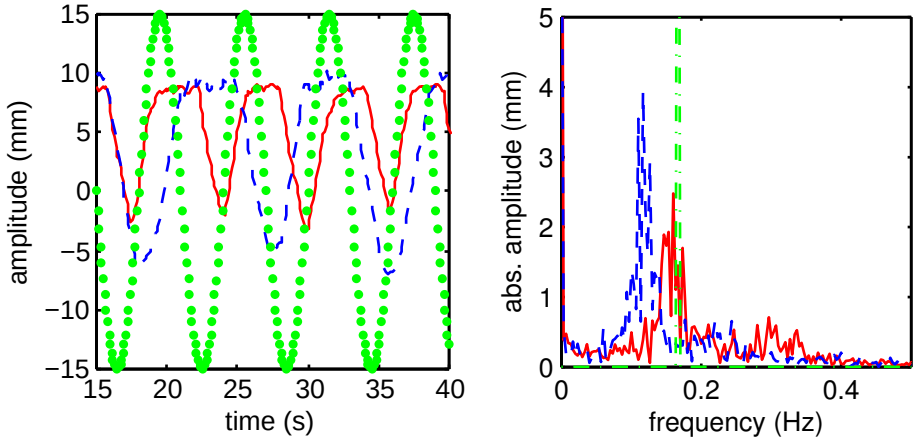

Figure 4.2: Breathing motion data of two volunteers and the (15 mm, 6 s) sinusoid in temporal (a) and frequency (b) domain. Notably, most signal energy is under 0.3 Hz. The spectrum is scaled to fit the physiologic signals.

Physiologic motion patterns were extracted from CC components of DVFs in the liver, extracted from coronally acquired MRI with 10 Hz imaging frequency.

The dosimetric response was evaluated based on these motion patterns in order to yield physiologically characteristic results. In order to present a continuous coordinate update to the motion controller, the data is upsampled by a factor of 2 to 20 Hz using MATLAB's (The Mathworks, Natick, MA, USA) standard reconstruction kernel (linear-phase Kaiser window filter). Consecutively, due to the relatively high noise level in the DVF, a 2.5 Hz-Butterworth low-pass (n=10) is applied to condition the raw motion signal before application to the motion stage. The noise level is caused by the EPI nature of the acquisition and the consecutive DVF extraction by an algorithm using an optical flow signal model (Horn and Schunck 1981). The cut-off frequency of the filter is chosen to leave physiologic components of the spectrum untouched. Thus, it solely filters higher-frequency noise induced by the imaging and motion estimation. The strong drop-off of the motion spectra over approximately 0.3 Hz in fig. 4.2b is an indicator for the frequency cut-off of the sampling field in the open-loop benchmark (cf. section 4.2.7).

4.2.5 Lag determination

The latency of the entire system is broken down to its elements illustrated in fig. 4.3. Two major experimental pathways have been followed throughout the experiment. Experiments regarding the MLC as an isolated element used the open-loop configuration, where the aperture is directly applied to the MLC (see fig. 4.3 lower solid path). In contrast, performing closed-loop experiments (fig. 4.3 upper solid path), the MLC was steered by the feedback control variable extracted by the tracking software.

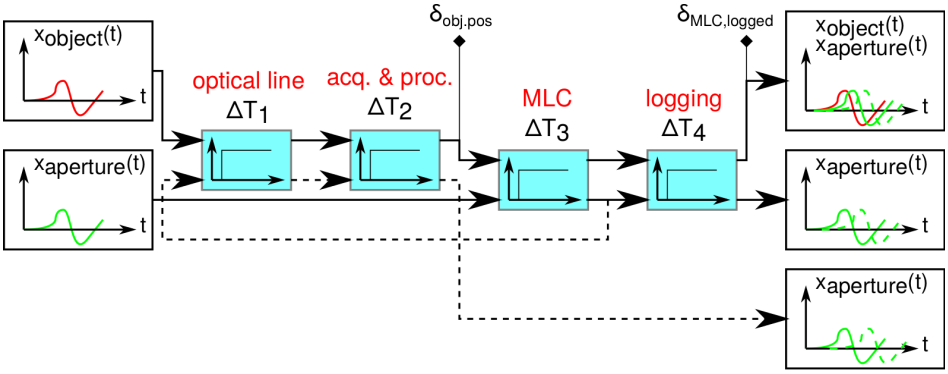

Figure 4.3: System lag components and experimental pathways in the feedback and open-loop configuration. The upper solid path emanating from the detected object motion represents closed-loop (or *tracking*) experiments. The other, lower solid paths show open-loop experiments with directly controlled MLC. For determination of the logging delay, the dashed pathway was employed. Diamonds indicate position data sampled. $\delta_{\mathrm{MLC,logged}}$ and $\delta_{\mathrm{obj.pos}}$ denote logging timing for MLC and object, respectively.

From a control input on the left side of the schematic in fig. 4.3, the signal is sequentially passed through the respective processing steps which take up their individual times $\Delta T_{1,2,3,4}$. These elementary delays are regarded in detail subsequently in sections 4.2.6 and 4.2.7.

4.2.6 Closed tracking loop

For the delay determination of the overall tracking system, the mean time elapsed between detection of the target and the aperture reaching that target has to be evaluated. This chain consists of several abstract elements which are specified in the following.

Regarding again fig. 4.3, object motion has to be captured by the camera hardware. After the readout, data is buffered and streamed via USB and the camera driver module until it is passed to the OpenCV application programming interface (API). The arising time delay is called ΔT_1. The received image is then processed subsequently in order to extract position information with the filtering algorithms presented in section 4.2.2. The runtimes of these filters, from the instance of grabbing the image until presenting the extracted position information to the MLC control system, are denoted ΔT_2. After exposing the current target position to the software interface, the MLC system needs time to approach the desired position. This lag is caused by the runtime of the MLC control system and the electromechanical properties of the MLC and is called ΔT_3.

Finally, for logging purposes, data is being received from the MLC side. Like the object position, the MLC position logging is delayed, taking ΔT_4 to arrive at the control computer.

For measuring the delay of the closed tracking loop, harmonics of the form

$$x(t) = A \sin\left(\frac{2\pi}{T}(t+\delta)\right) \tag{4.1}$$

are applied to the motion stage (cf. section 4.2.4) and tracked by the feedback loop. Logging both position updates and actual leaf positions yields

$$\Delta T_{loop} = \delta_{obj.pos} - \delta_{MLC,logged}. \tag{4.2}$$

Since the position updates and leaf positions arrive delayed by $(\Delta T_1 + \Delta T_2)$ and ΔT_4, respectively, the loop latency is to be corrected with

$$\Delta T'_{loop,corr} = \Delta T_{loop} + (\Delta T_1 + \Delta T_2 - \Delta T_4). \tag{4.3}$$

4.2.7 Identification of lag elements

Subsequently, the measurement of the system elements contributing to the overall delay of the feedback system are discussed.

Optical line delay ΔT_1 is the integrated lag value between a physical change of lighting and its detection in software. Offering transistor-transistor logic (TTL) outputs, a green light emitting diode (LED) is connected to the parallel DB-25 interface. In two separate threads, the light is switched on irregularly and measured by means of (binary) light detection using the same image acquisition software as in the tracking application. Timestamping both incidents yields a mean delay between incident and detection (Schellen, Dernehl, and Kowalewski 2013). The parallel port features a sufficiently fast reponse time in the μs-range (Koolwal 2009), sufficing the immediate switching requirement of this global time referencing step. The LED's electric dynamics is considered to be delay-free.

Acquisition and processing delay ΔT_2 is the time it takes to grab an image from the OpenCV API and process and forward it to the MLC control. As the value is local runtime, the time ΔT_2 is directly logged in each pass.

MLC delay or open-loop lag is the latency of the MLC system only. It is determined by commanding the aperture by a single-threaded program running at a fixed cycle time of 40 ms which corresponds to the real-time frame of the MLC control system. Commands are sent to the MLC in each cycle. At the time of sending, the commanded position is recorded, as well as the actual leaf position retrieved by the logging stream introduced in section 4.2.2.

To quantify the phase of the leaf positioning, an amplitude-period (A,T) parameter field of harmonics is sampled by applying synthesized harmonics directly to the MLC. The sines are in the form of eq. (4.1), with parameter A being in the domain $\{1, 1.5, 2, 2.5, 3\}$ cm and T in $\{3, 4, 5,..., 8\}$ s. Yielding pairs of sampled sine curves, the *commanded* and the *observed*, both curves are consequently fitted to a model as in eq. (4.1) using MATLAB's Curve Fitting Toolbox. To obtain the dynamic MLC lag, the temporal displacement δ for both fits are related; as the observed state is delayed for the logging/subscription lag ΔT_4, the measured phase difference is corrected for the subscription delay time T_4

$$\Delta T_3 = \delta_{MLC,commanded} - \delta_{MLC,logged} - \Delta T_4. \tag{4.4}$$

Logging delay ΔT_4 is indirectly measured by capturing the aperture light field (ALF) in an open-loop experiment. The ALF position is extracted using the tracking method descibed in section 4.2.2. ΔT_4 is then determined by fitting the ALF-mediated aperture position against the subscribed positions. The influence of ΔT_1 and ΔT_2 is regarded for by taking the previously determined values in the LED-delay experiment and in the image processing log data into account.

Qty.	μ	$\widehat{\sigma}$	remark
-	ms	ms	-
ΔT_1	78.7	19.6	multimodal
ΔT_2	20.6	1.7	correlation (100x38)
	5	0.2	MOSSE (32x32)
	11.9	0.4	MOSSE (64x64)
ΔT_3	15.9	6.6	sampled parameter field (fig. 4.4)
ΔT_4	52	-	one experiment (param.-fit)

Table 4.1: Results for average values of dead times $\Delta T_{1,2,3,4}$ with their estimated standard deviations $\widehat{\sigma}$.

4.3 Results

The experiments on the feedback system are evaluated, starting from an elementary consideration of each element in the loop and its individual contribution to the feedback lag. Subsequently, the integral feedback lag is measured and its impact on the tracking experiment based on physiologic motion is shown.

4.3.1 Elementary timings of the feedback system

Table 4.1 shows the resulting lag contributions for each component individually. Very prominent is the relatively long line feed time of the imaging system ΔT_1. Additionally, its distribution deviates significantly. The various tracking algorithms unsurprisingly yield different lags in the ΔT_2-estimation. The correlation, being a global filter, is the slowest. The subscription delay ΔT_4 is extracted from a single parameter fit, thus no parameter statistics are available.

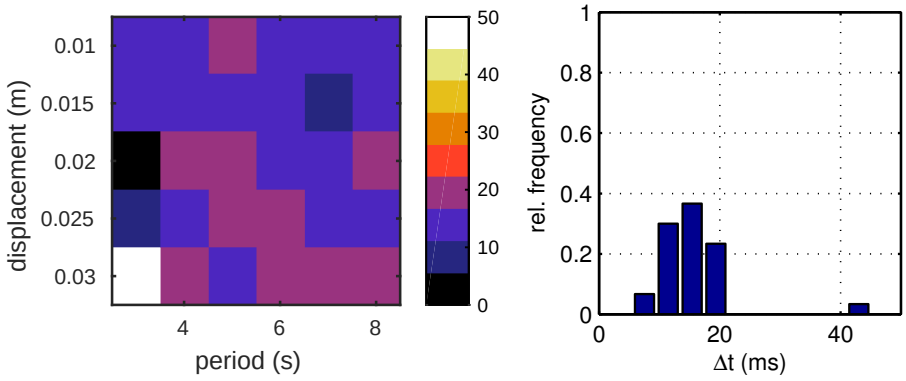

(a) **(b)**

Figure 4.4: Open-loop MLC latencies for the sampled parameter field in a. The distribution of the delay times is shown in b.

The open-loop delays ΔT_3 are depicted in fig. 4.4a in a map representing the pa-

rameter field. Although, a Gaussian distribution cannot be presumed, overlapping median and mean $\Delta\overline{T}_4$=$\Delta\widetilde{T}_4$=15.9 ms imply symmetry of the distribution with a estimated standard deviation of σ=6.6 ms. The minimal coefficient of determination of the obtained fits of the entire parameter field was R^2_{min}=99.63 %. The coefficients of determination indicate proper data fits and consequently significant lag extraction.

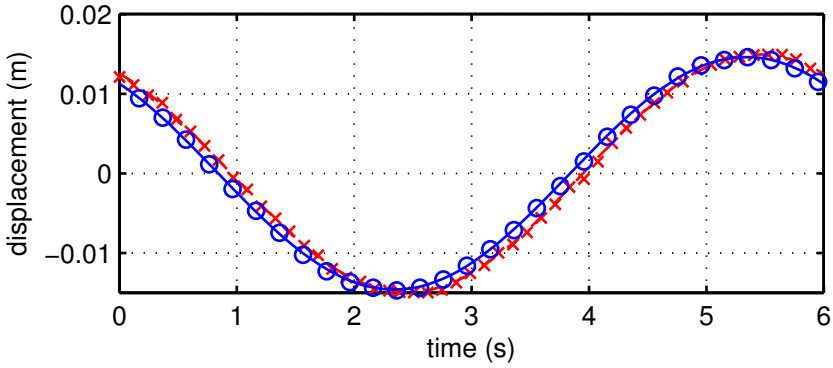

Figure 4.5: Closed-loop logging data and relative lag determination using fitted objection (solid-blue with ∘ data points) and aperture motion (red with ×-illustrated points. Solely every third data point is shown for clarity.

4.3.2 Closed-loop feedback lag determination

Figure 4.5 shows a section of the fitted data from object and aperture position. Both fits had R^2>99.94 %. The extracted lag $\Delta T'_{loop,corr}$ was determined to be 109.3 ms, based on the relative phase between the fitted curves and after correction according to eq. (4.3).

Irradiation under physiologic motion (blue traces in fig. 4.2) yielded the normalized dose distribution in fig. 4.6. As expected, the untracked distribution in fig. 4.6b shows significant smearing around the edges perpendicular to the leaf travel direction. Also lateral deviations are visible. Choosing an aperture relatively larger than the displacement of the tracked object ($w_{aperture}/2>\max\{\|\Delta x\|\}$ yields the anticipated visible dose plateau phase in the center of the distribution.

4.3.3 Film dosimetry

Figure 4.7 integrates the relative dose maps of fig. 4.6 into histograms; fig. 4.7a shows the distribution of dose difference between static object (reference) and untracked object. The multimodal distribution shows two lateral side maxima caused by the comparatively long excursion plateaus of the motion trace. In fig. 4.7b, the distribution morphs into a compact, mean-free Gaussian-like distribution with $\widehat{\sigma}\,(\Delta D)$=1.38 % using tracking.

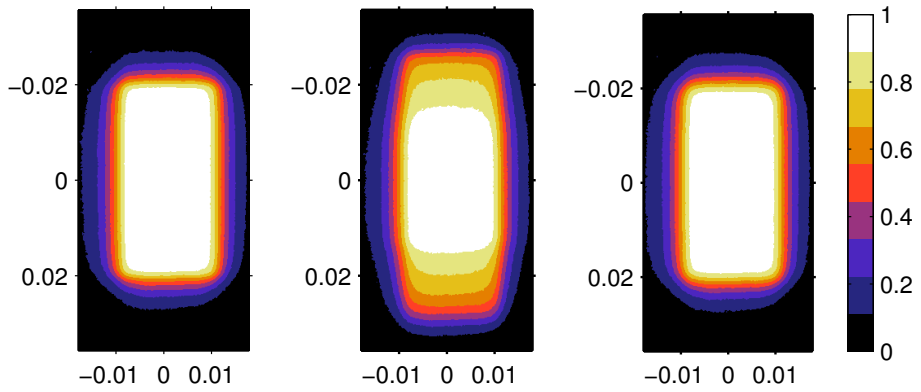

Figure 4.6: Normalized dose distributions under physiologic conditions: in a static (a), untracked dynamic (b) and tracked dynamic case (c). Leaf travel direction is the vertical direction. Axis units in m.

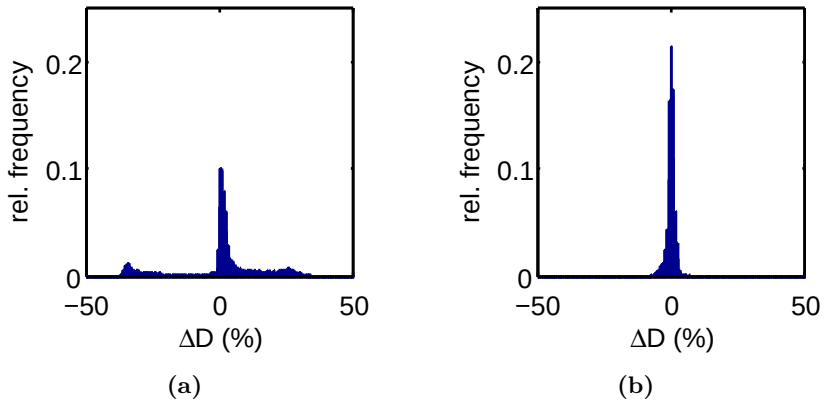

Figure 4.7: Relative difference histograms of untracked a and tracked b relative dose distribution.

In the γ-map of fig. 4.8, the γ-pass rate extracted from the thresholded ($\gamma < 1$) maps of fig. 4.8 changed from 49 % for the untracked case, to 92 % for the tracked case. The concentration of γ-failed points is in regions of large spatial dose gradients, i.e. around the location of the leaf tips. The pass area in both γ evaluations at y=0.02 m shows intersecting dose profiles, the reference dose and the dose accumulating during tracking being at the same level. Due to the ideally strong gradients with the reference aperture a pass region will be observed with a width solely dependent on the geometric component of the γ-statistics.

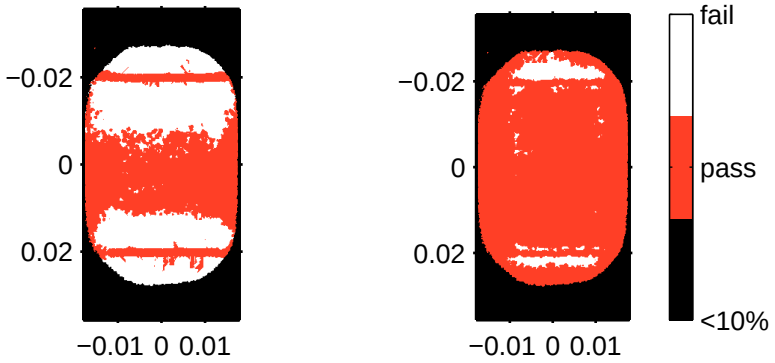

Figure 4.8: Thresholded $\gamma\,(1\,\%1\,mm)$ maps of films without (a) and with MLC tracking (b). The red area designates the region of $D_{rel} > 10\,\%$ where the γ-test has passed, whereas white indicates points of failed test. Axis units in m.

4.4 Discussion

For the dynamic experiments, the Agility MLC was driven in a continuous manner, avoiding inertial effects. This resulted in a low MLC delay of 15.9 ms shown by indirect measurement. Although exhibiting significant variance, the phase featured linear phase behaviour in the sampled parameter field. Considering the real-time frame of 40 ms, this small delay is likely to be caused by feed-forward terms in the MLC control system, imposing a ballistic extrapolation between adjascent control points of two consecutive cycles. These findings complement step-responses for the Varian Millenium MLC by (Poulsen et al. 2010) in which time delay was determined to be constant for a limited MLC adjustment step.

Aiming for potential MLC tracking in an MR-linac, 2D imaging rates are expected to be in a range of 2-4 frames per second; accordingly an upsampled, extrapolated object position variable in order to update the MLC in every control system cycle could yield a dosimetric advantage of low MLC latency compared step-wise MLC response. Furthermore, using 1D navigator echoes, Stam et al. (2012) could get

anatomy information every 15 ms, which could be used as a fast surrogate tracking variable in combination with an organ correlation model.

Compared to the low apparent MLC latency, current clinical position extraction modalities such as approximately 90 ms for Calypso (Smith et al. 2009), 100 ms for MRI (Ries et al. 2010) and >160 ms for kV/MV imagers (Poulsen et al. 2010) contribute to the overall latency to a much higher extent. Notably, for the non-clinical tracking implementation with a customary camera, the most significant contributor to the overall delay of about 110 ms was the imaging API itself. The API delivered images with an average of 78.7 ms, which can be explained by the buffer strategy of the frame capturing cascade of the OpenCV API (Schellen, Dernehl, and Kowalewski 2013). It is however expected that this lag component can be be overcome in a clinical modality using real-time communications as demonstrated by Ries et al. (2010) and Crijns, Raaymakers, and Lagendijk (2012).

Knowing the MLC-inherent logging delay ΔT_4 in addition to the MLC delay, dose can be accumulated retrospectively by knowing both temporal and geometric interplay of MLC and anatomy. The variance of ΔT_4, although being extracted from only a single indirect measurement, is expected to be small, since the position subscription runs with a time frame of the Agility MLC control system.

Dosimetric deviations are distributed in a non-standard distribution for both tracking and static MLC applications. Qualitatively, both the relative differences and the γ-score show the performance improvement of tracking (γ=92 %) versus static (γ=49 %) MLC irradiation. Since the previously published, more relaxed γ statistics with radii of as shown by Smith et al. (2009) 3 mm/3 % are intended to rate the outcome of the entire treatment chain, the stringent $\gamma\,(1\,mm/1\,\%)$-statistics may be more suitable as a representative integrated quantifier for rating the tracking performance of the tracking-system in an isolated manner. Observed dosimetric deviations laterally, perpendicular to the leaf travel direction, is due to radial anisotropy of the beam itself and the dosimetry setup, i.e. differing path lengths through the dosimetry set-up. The latter is adding to the fact that retrospective dose accumulation cannot solely be computed with a simple convolution kernel constructed by system delay, but has to account for the beam characteristics, e.g. by incorporating the aperture and anatomy position into the TPS for retrospective dose calculation published by Poulsen et al. (2012) and clinically used by Keall et al. (2014). This is especially true in flattening filter-free applications. However, while knowledge about machine geometry is comparatively easy to obtain knowing the timing parameterization, more details about tissue position over time has to be integrated into the process either by fast 3D imaging techniques or precise motion models using surrogates. Recently, Bjerre et al. (2013) and Brix et al. (2014) could successfully employ MRI to rapidly infer 3D anatomy motion.

For applying tracking in the second dimension perpendicular to the leaf-motion, on-line sequencing needs to be elaborated. Also, the dependency of the MLC dynamics on gantry and collimator angle needs further investigation. As shown

within this paper, position prediction filters will be needed to be further investigated in order to keep the MLC in the presented continous motion and to compensate for the potentially variable system delay.

4.5 Conclusion

The tested Agility MLC system showed notably low latency times when driven in a continuous manner; extracted timing characteristics indicates good MLC tracking performance with regards to commonly employed imaging and surrogate positioning techniques. Counteracting bottlenecks in tracking cascades will thus have to emphasize on fast and responsive imaging techniques. The shown phase linearity enables generic parameterization of predictive algorithms. An adaptive framework for dMLC tracking employing the Agility MLC could succesfully be employed and first dosimetric experiments based on in-vivo liver motion showed expectably improved dosimetry performance both in relative dosimetry and in a γ-sense.

This work was supported by research funds from Elekta Ltd., UK. We appreciate their efforts in providing experimental research versions of machine firmware which enabled this work.

CHAPTER 5

Auto-adaptive margin generation for MLC tracking

The following chapter is based on:
Glitzner, M., Fast, M. F., Denis de Senneville, B., Nill, S., Oelfke, U., Lagendijk, J. J. W., Raaymakers, B. W., and Crijns, S. P. M. (2017a). "Real-time auto-adaptive margin generation for MLC-tracked radiotherapy". In: *Phys. Med. Biol.* 62.1, pp. 186–201

Abstract

In radiotherapy, abdominal and thoracic sites are candidates for performing motion tracking. With real-time control it is possible to adjust the MLC position to the target position. However, positions are not perfectly matched and position errors arise from system delays and complicated response of the electromechanic MLC system. Although, it is possible to compensate parts of these errors by using predictors, residual errors remain and need to be compensated to retain target coverage. This work presents a method to statistically describe tracking errors and to automatically derive a patient-specific, per-segment margin to compensate the arising underdosage on-line, i.e. during plan delivery.

The statistics of the geometric error between intended and actual machine position are derived using kernel density estimators. Subsequently a margin is calculated on-line according to a selected coverage parameter, which determines the amount of accepted underdosage. The margin is then applied onto the actual segment to accommodate the positioning errors in the enlarged segment.

The proof-of-concept was tested in an on-line tracking experiment and showed the ability to recover underdosages for two test cases, increasing $V_{90\%}$ in the underdosed area about 47 % and 41 %, respectively. The used dose model was able to predict the loss of dose due to tracking errors and could be used to infer the necessary margins.

The implementation had a running time of 23 ms which is compatible with real-time requirements of MLC tracking systems. The auto-adaptivity to machine and patient characteristics makes the technique a generic yet intuitive candidate to avoid underdosages due to MLC tracking errors.

5.1 Introduction

In radiotherapy, dose conformity, the ratio of actual to intended dose deposition, is impaired by the change of patient anatomy during (*intra*) treatment and between (*inter*) treatment fractions. *Intra-fraction* changes occur predominantly in thoracic and abdominal sites which are directly modulated by breathing excursions (e.g. (Moerland et al. 1994; Plathow et al. 2004)). Tracking can be used to adapt the treatment beam to a variable tumor position (Ruan, Kupelian, and Low 2011). Recently, on-line MLC control has become available on the treatment machines of major radiotherapy vendors and first tracked deliveries were performed *in-vivo* (Colvill et al. 2015).

However, the quality of conformity using MLC tracking is to a high extent influenced by the underlying system delay, which can amount up to several hundreds of milliseconds (Hoogeman et al. 2009; Tacke et al. 2010; Depuydt et al. 2011; Fast et al. 2014; Glitzner et al. 2015c; Bedford et al. 2015). Typically, the feedback

controller in MLC tracking processes the incoming signal of an imaging/positioning modality. Subsequently, the (affine) target displacement is extracted from the signal. A planned reference segment, shifted to the new target position in beam's eye view (BEV), is then sent to the MLC controller. All of these components exhibit an inherent time delay which cause lag and thus misalignment between the target and the treatment beam. As a simplification, these time delays are usually quantified using sinusoidal motion patterns, assuming a linear phase behavior of the entire MLC system (Glitzner et al. 2015c). In reality, the electromechanic MLC system will not behave according to a single, pre-set lag but will show a response comparable to fig. 5.1. The prescribed position (blue) will not only cause a shifted MLC response (red). Contrary, the machine response will show complex over- and undershoots, which cannot be explained by a constant lag alone.

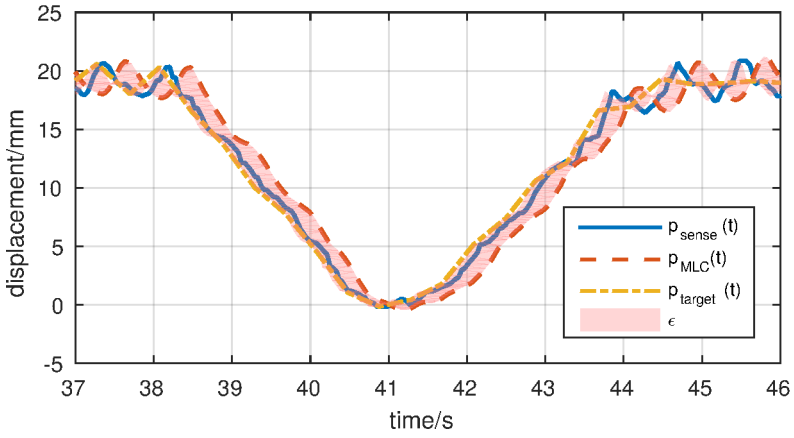

Figure 5.1: Recorded target (p_{target}) and MLC (p_{MLC}) evolution during a tracking experiment. Delayed target positions (p_{sense}) were used as a feedback variable. The integral tracking errors of the various tracking system components are highlighted in red.

Look-ahead predictors are designed to compensate the constant lag effects. In general, however, the quality of the predictor strongly depends on the characteristics of the patient motion, such as amplitude, frequency and phase variations, as well as on its parameterization and the machine performance itself (Ruan 2010; Krauss, Nill, and Oelfke 2011).

Additionally look-ahead predictors can (by definition) not account for the mentioned non-constant-lag effects. The tracking errors arising due to these imperfections can be regarded as stochastic errors. In order to retain target coverage they have to be compensated e.g. by using tracking margins.

In this study a method to automatically compensate for dosimetric errors arising from machine and physiologic uncertainties using auto-adaptive tracking margins is proposed. In contrast to the margins defined by International Commission on Radiation Units and Measurements (ICRU) (ICRU 83 2010) which are applied

to the CTV during the planning process, the proposed method works on a per-segment basis during delivery, i.e. after plan optimization. The real-time process is intended to provide optimal target coverage in the sense of percentual coverage to a selected confidence level. The method uses the capability to read-out the actual MLC positions $\boldsymbol{p}_{\mathrm{MLC}}(\mathrm{t})$ in every control system cycle of 40 ms. These are combined with the retrospectively known $\boldsymbol{p}_{\mathrm{target}}(\mathrm{t})$ to estimate the positioning error $\boldsymbol{\epsilon}(\mathrm{t})$ and integrate it into a tracking margin.

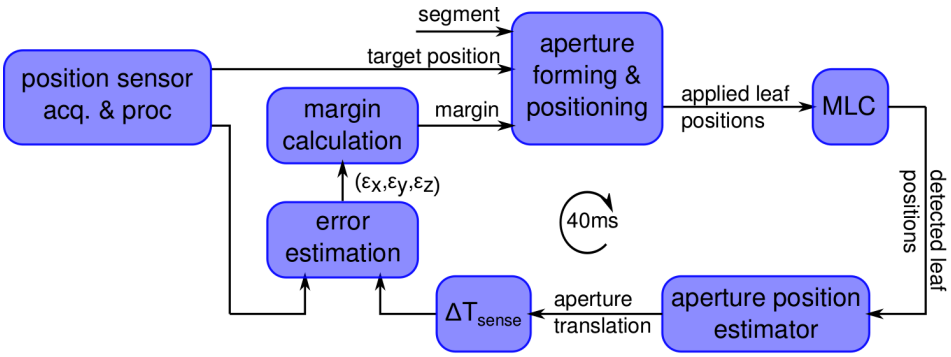

Figure 5.2: Proposed adaptive tracking margin control system.

5.2 Methods

The set-up comprises multiple hardware and software components, as depicted in fig. 5.2. Every block in the component diagram is explained in detail subsequently. All software was based on C++ implementations running on a Linux Mint computer (kernel version 3.16) with two Intel Xeon E5-2620 at 2 GHz and 32 GB memory.

5.2.1 Position acquisition & processing

In order to provide the MLC feedback-loop with a reference variable, the target positions are continuously sent by the position sensing module.

This abstracted block can source data of any kind, such as MV, kV, MRI or marker/transponder information. Eventually, the processing cascade extracts an estimated target position

$$\boldsymbol{p}_{target}(t) = (p_x, p_y, p_z)^T(t)\,. \tag{5.1}$$

Position sensing is likely to be the main source of delay in an MLC control system due to the complexity of acquisition and processing of imaging data. In order to keep track of these delays, the pipeline requires thorough timestamping throughout the processing cascade.

The timestamp of $\boldsymbol{p}_{\mathrm{target}}(\mathrm{t})$ is assumed to be adjusted by the target position's acquisition and processing delay $\Delta\mathrm{T}_{\mathrm{sense}}$. Although some jitter has to be expected,

it is assumed to be minimal on real-time implementations; thus ΔT_{sense} is set to constant values for this proof of concept. Generally, however, the capability of processing non-constant delays can be implemented easily by dynamically adapting the interpolation kernels' shift (*look-back*).

5.2.2 Aperture forming & positoning

In this block, a valid MLC prescription is generated, which comprises position data for the leaves and jaws of the MLC.

In general, segment shapes from the treatment plan and actual target positions are passed on to this block. The planned aperture is consequently shifted to the new target position, incorporating the imposed discretization by the MLC leaves. In this work, an implementation based on Sawant et al. (2008) was employed. This algorithm subdivides the coarse leaf-width into subleaves and translates the initial aperture according to the finer discretization. Upon prescription of a polygon, the leaf-positions are determined by averaging over the subleaf-positions. The diaphragms were steered as in Fast et al. (2014), applying the offset perpendicular to leaf-travel direction directly to the planned jaw-positions.

In this work, the aperture forming and positioning was extended to impose segment margins in real-time. In order to do so, the process receives margin prescriptions in the form

$$\boldsymbol{m}\left(t\right) = \left(\left(m_{\hat{x}+}, m_{\hat{x}-}\right), \left(m_{\hat{y}+}, m_{\hat{y}-}\right)\right)^{T}, \tag{5.2}$$

$\hat{x}$ and $\hat{y}$ denoting the axis parallel and perpendicular to the leaf-travel direction, respectively. The side, on which the margin is added on the respective axis relative to the MLC's isocenter is indicated with + and -. This enables prescriptions of individual margins for both sides of both the principal axes of motion.

The tracking margins were calculated and imposed on the planned segment using the following sequence: First, the planned segment is transformed into a polygon which in turn is rasterized using the OpenCV library (Bradski 2000). Rasterization yields a grid with an isotropic resolution of 0.25 mm in both leaf travel and leaf count direction. Secondly, using morphologic dilation in the two principal directions ($\hat{x}$ and $\hat{y}$), an expanded raster is created. Using OpenCV, the vertices of the raster's outline are determined and translated into a polygon (see fig. 5.3). The resulting polygon is then applied to the MLC using the leaf-shaping algorithm. The spacing of the MLC's diaphragms is modified similarly, using the margins perpendicular to the leaf travel direction.

The dilation kernel is calculated using the grid resolution of the margin generator and the margin size in the individual directions. At a grid resolution of 0.25 mm, a typical kernel element would, assuming a margin of (-4 mm, 2 mm), contain 25 elements: 16 in negative direction, one center element and 8 in positive direction.

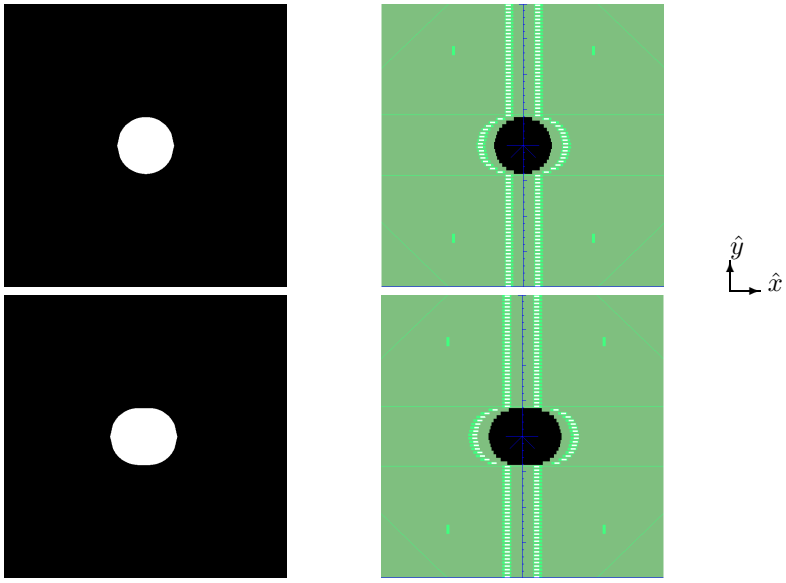

(a) rasterized polygon segments **(b)** prescribed segments

Figure 5.3: (a) shows the effect of margin-controlled dilation on rasterized polygons; the original aperture (left) is dilated in $\hat{x}$-direction. From the contours of the dilated shape, a new valid MLC-segment is calculated by the leaf-shaping algorithm (b).

5.2.3 Error quantification

Once an aperture is applied to the MLC, the on-board control system drives the leaves and jaws in order to reach the new position in a time frame of 40 ms.

Due to mechanical inertia, the MLC-system will answer to a prescribed position change with delay. This change can be described with an MLC-latency ΔT_{MLC} for sinusoidal reference signals (Glitzner et al. 2015c)

$$\boldsymbol{p}_{MLC}(t) = \boldsymbol{p}_{sense}(t - \Delta T_{MLC}), \tag{5.3}$$

with $\boldsymbol{p}_{\mathrm{MLC}}(\mathrm{t})$ and $\boldsymbol{p}_{\mathrm{sense}}(\mathrm{t})$ being the center of gravity (COG) positions of the actual and the ideal aperture, respectively.

However, tracking physiologic motion is more complex. Thus a parameterization of ΔT_{MLC} obtained by the phase difference between two sine curves is insufficient and impossible to extract for a general case. In order to determine the error due to MLC-latency, the actual MLC-position is read out every control system cycle (CSC) (40 ms) using the MLC control system. Neglecting the latency of this readout, the

difference to the prescribed position $\boldsymbol{p}_{\text{sense}}$ determines the actual tracking error

$$\boldsymbol{\epsilon}'(t) = \boldsymbol{p}_{MLC}(t) - \boldsymbol{p}_{sense}(t). \tag{5.4}$$

In addition, the discussed signal acquisition and processing latency $\Delta\text{T}_{\text{sense}}$ has to be taken into account into account. The sensed position is considered as a shifted version of the actual target position in the BEV, which reads

$$\boldsymbol{p}_{target}(t) = \boldsymbol{p}_{sense}(t + \Delta T), \tag{5.5}$$

with $\boldsymbol{p}_{\text{target}}$ being the real target position at time t. The tracking error including $\Delta\text{T}_{\text{sense}}$ thus reads

$$\boldsymbol{\epsilon}(t) = \boldsymbol{p}_{MLC}(t) - \boldsymbol{p}_{target}(t) = \boldsymbol{p}_{MLC}(t) - \boldsymbol{p}_{sense}(t + \Delta T_{sense}). \tag{5.6}$$

Considering causality, ϵ(t) is only known $\Delta\text{T}_{\text{sense}}$ after its occurrence

$$\boldsymbol{\epsilon}(t' - \Delta T_{sense}) = \boldsymbol{p}_{MLC}(t' - \Delta T_{sense}) - \boldsymbol{p}_{sense}(t'). \tag{5.7}$$

Thus, for a given time t′, the sensed object position is compared to a shifted MLC-position, yielding an estimated error for that moment.

The errors were measured and extracted independently for each principal direction $\hat{x}$ and $\hat{y}$.

5.2.4 Error statistics

The estimated error $\boldsymbol{\epsilon}$(t) is recorded over an adjustable time period to build up the statistics, necessary to extract statistical features for quantifying an error margin. Figure 5.4a displays a representative ϵ-distribution of a tracking experiment using a physiologic tracking variable. The histogram shows the apparent skewness of the multi-modal distribution.

Since histograms inherently suffer from binning uncertainties, kernel density estimators (KDEs) were used to construct continuous densities p_ϵ(x) from the sample population. KDEs work as a sum of primitive kernels K_σ (Elgammal et al. 2001) centered about each measured sample ϵ_{n} as

$$p_\epsilon(x) = \sum_{n=0}^{N} K_\sigma(x - \epsilon_n). \tag{5.8}$$

The technique has been already employed in MLC tracking target prediction by Ruan (2010). As a primitive, a zero-mean Gaussian kernel was chosen, which needed to be parameterized by its σ, i.e. its bandwidth, which was calculated using a rule-of-thumb (Bowman and Azzalini 1997). As the control system receives

updates of the actual target and aperture position every 40 ms, a (cyclic) first in first out (FIFO) buffer of typically N=500 is updated concurrently and used to populate eq. (5.8). Accordingly, an error statistics of the past 20 s is established, which is then used as an estimate of the current tracking error.

5.2.5 Dose model

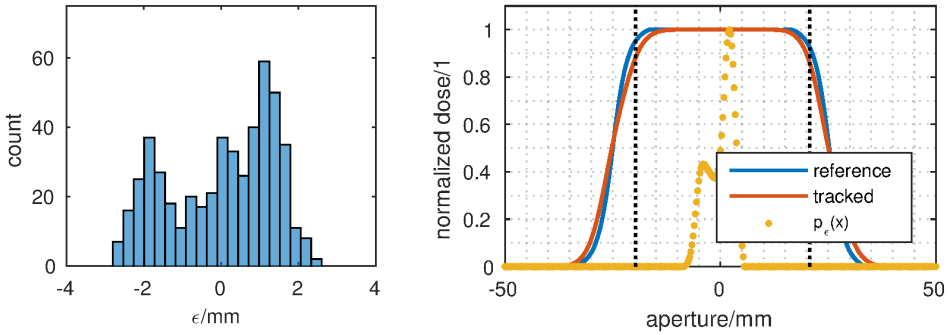

(a) discrete histogram

(b) smearing

Figure 5.4: (a) Exemplary aperture positioning error (ϵ) histogram for physiological motion. (b) shows the degraded profile (red) due to the error distribution (yellow). The dashed lines indicate $\hat{x}$, where $D(\hat{x}) = 0.9$.

In this work, the geometric error statistics are integrated into a dose model to extract a margin description, which is able to compensate tracking errors to a predefined extent and can be used as an input for the aperture adaptation algorithm proposed in section 5.2.2.

For each axis, tracking error statistics p_ϵ can be translated into dose errors by convolution with the reference dose D_{ref}

$$D_{dyn}(x) = (D_{ref} * p_\epsilon)(x) = \int_{-\infty}^{+\infty} p_\epsilon(x - x') \cdot D_{ref}(x')dx' \tag{5.9}$$

in analogy to studies about static treatment beam and moving anatomy (Beckham, Keall, and Siebers 2002; Bortfeld, Jiang, and Rietzel 2004). While, therein, the MLC-segment remained static, both segment and (tracked) anatomy are under motion in this work.

5.2.6 Reference dose model

Ideally, $D_{ref}(x)$ in eq. (5.9) is a static, rectangular dose distribution $D_{static,ideal}$. However, beam limiting devices such as MLCs do not have ideal cut-off behaviour at segment limits, but exhibit a continuous roll-off, i.e. the penumbra.

To account for the effect in the dose model, the penumbra has to be described and estimated. Similar to convolution-adapted ratio of tissue-air ratios (CARTAR)

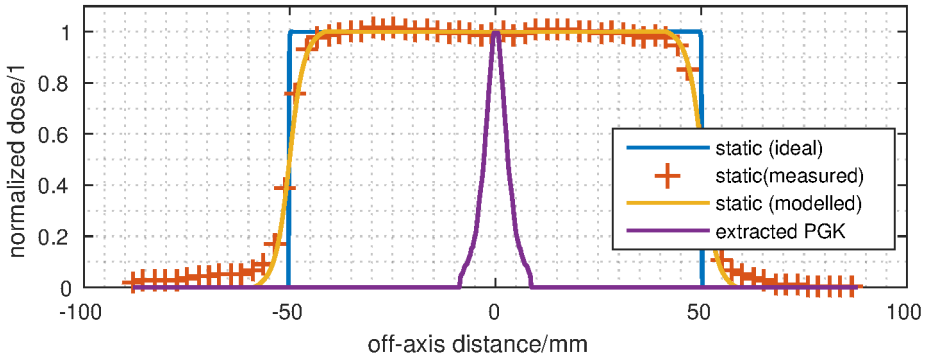

Figure 5.5: Schematic of penumbra extraction: The PGK (purple) was extracted from the ideal static dose profile (blue) and the measured static dose profile (red,+). This results in a model description of the real static dose profile (yellow).

of Low et al. (1995), the penumbra due to scatter of beam limiting devices is estimated as a penumbra-generating kernel (PGK). It is assumed to be invariant to shifts with respect to the isocenter and radially symmetric.

As depicted in fig. 5.5, the PGK is used to generate $D_{static,real}$. It modifies an ideal rectangular (block) dose $D_{static,ideal}(x)$, such that

$$D_{static,real}(x) = (PKG * D_{static,ideal})(x). \tag{5.10}$$

It is possible to deconvolve a static measurement $D_{static,meas}(x)$ with the synthetic $D_{static,ideal}(x)$ to obtain PKG(x). To do so, $\mathcal{F}\{D_{ref,ideal}(x)\}$ needs to be conditioned. Here, we used waterlevels (Richard, Borchers, and Clifford 2013) for regularization of $\mathcal{F}\{D_{static,ideal}(x)\}$.

The PGK was estimated accordingly by deconvolution of a calibration film measurement of a 10x10 cm^2 square field. Subsequently, the extracted PGK was loaded into the tracking software and used for the margin extraction described in the following section.

5.2.7 Margin extraction

Using the dose model of section 5.2.5, a relation can be established between the reference dose and the dose distribution which is actually being delivered considering the (known) error probability.

By calculating both error-imposed and intended dose distributions, a geometric difference between the two distributions can be estimated. The dose-level at which this difference is estimated is denoted *confidence level* $\hat{D}$ and describes the relative level of reference dose, the control-loop will aim to recover in order to compensate the loss of dose due to tracking errors.

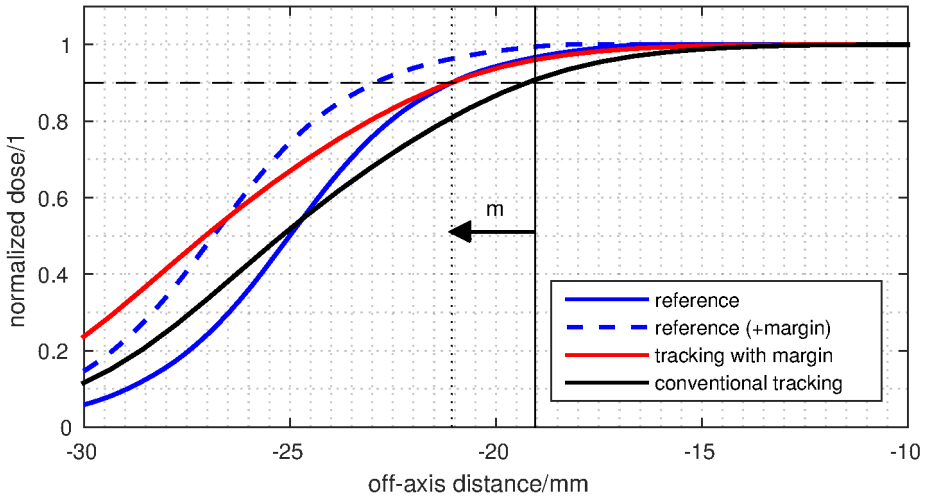

Figure 5.6: Margin expansion in tracked distribution: tracked delivery causes a loss of dose in the shoulder of the reference distribution. This can be observed in the transition of the static dose line (solid blue) to the tracked dose line (black). In order to compensate this loss to a defined confidence level (90% of intended dose, dashed horizontal line), the initial segment has to be expanded about a margin m, indicated by the arrow.

In fig. 5.6, the confidence level is set to $\hat{D}$=0.9. The expansion widths in the same figure is found by solving

$$D_{ref}(x) = D_{dyn}(x+m) = \hat{D} \tag{5.11}$$

for m. Subsequently, the margin is applied by dilating the static reference aperture about m, i.e. the difference between ideal and real dose. In the example of fig. 5.6, m equals approximately 2 mm.

5.2.8 Experimental set-up

Film dosimetry

The performance of the margin compensation was measured using radiosensitive film (Gafchromic EBT3, Ashland, NJ, USA). To calibrate the film, depth-dose curves were acquired. The beam was parameterized with 6 MV, a dose rate of 550 MU/s and an aperture of 10x10 cm^2 at isocenter. The gantry was set to 90°, irradiating the horizontally oriented film (aligned with the beam axis) which was sandwiched between two 5 cm square blocks of solid water at 100 cm surface distance from the source. Depth-dose curves of four doses (50, 150, 400 and 700 MU) were exposed to capture a wide dynamic range of the film. After exposure the films were scanned using an Epson Expression 11000XL (Seiko Epson Corp., Nagano,

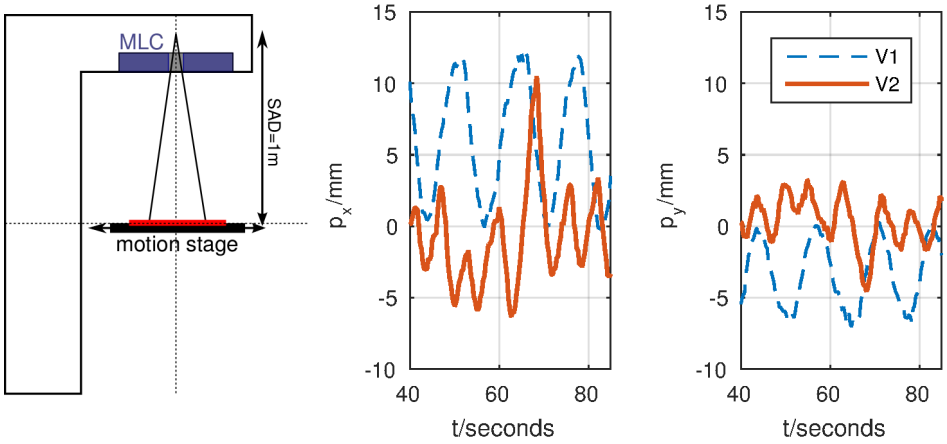

(a) hardware placement **(b)** x-displacement **(c)** y-displacement

Figure 5.7: (a) shows the measurement set-up with MLC (purple), motion stage (black) and film set-up (red). (b) and (c) display the x- and y-components of the motion traces of two volunteers (V1 and V2) applied to the motion stage.

Japan) in transmission mode with 96 dpi spatial resolution and 48 bit color depth (16 bit per channel). Film calibration was done using a fit to a previously measured dose-depth-curve using in-house developed software of The Royal Marsden, London, UK. A one-channel calibration using the green color channel was chosen because it yielded the best fit.

Motion set-up

For the tracking experiment, the imaging plane was at 100 cm source-to-imager distance (SID). The radiosensitive film was placed under 2 cm of solid water build-up and on 5 cm solid water backscatter material. A 5 cm circular aperture was applied as a reference segment. The gantry was set to 0° and the collimator angle was 90°. The film was irradiated with 550 MU with a 6 MV beam at 550 MU/min.

The physiologic motion data was obtained from the imaging data of two volunteers. The volunteers underwent fast 2D MRI for 5 min, yielding coronal MR images with 10 Hz temporal and 2x2 mm^2 spatial resolution and 6 mm slice thickness.

To extract the motion information, the image dynamics were then non-rigidly registered to the first image in the series (reference image) using the method described by Zachiu et al. (2015). Consequently a point located in the liver dome of each volunteer was selected from the DVF to obtain a single motion trace (figs. 5.7b and 5.7c). A point in the liver dome was selected to obtain a challenging target for the MLC tracking system, with displacements stemming from the highly modulating breathing excursions and heart beat. The extracted point served as a motion surrogate for the MLC tracking. This 2D displacement was applied to the

MLC using the aperture positioning algorithm of section 5.2.2.

No breathing instructions were given to the volunteers at any time. The amplitude of motion was comparable to previously reported displacements of the diaphragm (Korin et al. 1992). However, the volunteers featured different classes of breathing excursion. While $V1$ showed sleep-related regular displacements, $V2$ showed a pattern irregular in frequency and amplitude. The 10 Hz motion traces were upsampled to 64 ms intervals using a linear interpolation kernel in MATLAB (*The Mathworks*, Natick, MA, USA).

An in-house 4D motion stage (Davies et al. 2013) was used to move the radiosensitive film, simulating patient motion at 1 m SAD. In addition to executing the motion pattern, the motion stage also provides a position feedback ($\approx$ 1 ms latency (Fast et al. 2014)) signal with 30 Hz update rate, which is used as tracking variable.

On-line measurements

To test the adaptive tracking margin generation and its dosimetric gain, the position feedback was artificially delayed, simulating the latency of a realistic imaging system, comprising acquisition, processing and transmission of imaging data. A latency of 300 ms was thus set for both volunteer trajectories. Accordingly, ΔT_{sense}=300 ms was constantly set for estimating the tracking margin (fig. 5.2). Throughout, coverage values of $\hat{D}$=0.9 were tested and delivered on-line on an Elekta Synergy (Elekta AB, Stockholm, Sweden) research linac. The real-time software controlled the equipped Agility MLC using a research tracking interface provided by Elekta Ltd., UK.

Film analysis

For each volunteer, four films were irradiated to capture the static, untracked, tracking and margin-compensated tracking case. The doses of all films were referenced to the average dose value in a 15×15 mm^2 area in the central plateau of the respective static exposure. For qualitative analysis, difference maps between untracked, tracked and (static) reference dose distributions were generated.

To show the compensation performance of the margin generator in 2D, contour lines at $\hat{D} = 0.9$ of the static refernce, tracking and margin-compensated tracking exposures were calculated. In 1D, a profile was sampled along the principal axes of motion of the breathing trajectories. The principal axes of motion were extracted from the untracked exposures using MATLAB's (The Mathworks, Natick, MA, USA) principal component analysis (PCA).

Quantitatively, dose-area histograms (DAHs) were generated to measure the dose recovery. To measure the dose recovery performance in the entire circular aperture, an area defined by lower dose threshold of $D < \hat{D} = 0.9$ was selected. To specifically select the shoulder area of the 2D dose distributions, thresholds of

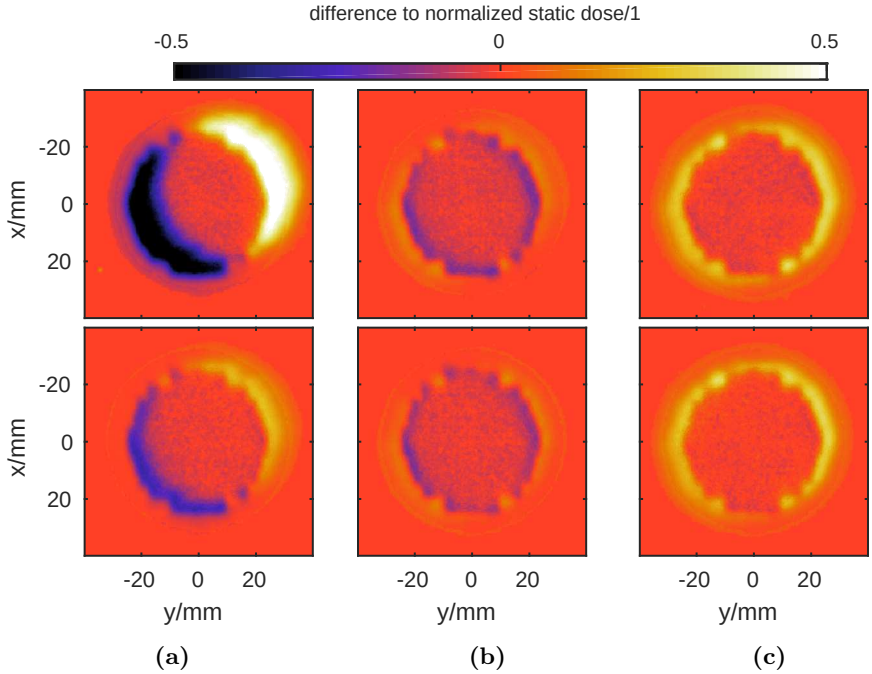

Figure 5.8: 2D dose distributions for two volunteer datasets (upper row and lower row, respectively) relative to the static reference. (a) displays the untracked case. In (b), tracking responses are shown. (c) shows results with margin expansion.

$\hat{D} < D < 0.97$ were chosen. In the selected areas, $A_{90\,\%}$, the relative area with more than $\hat{D}$=0.9, was calculated.

5.3 Results

The dose responses from the tracking experiments with imposed imaging delay of 300 ms are displayed in fig. 5.8. fig. 5.8a illustrates the mean position of the two motion traces, with respect to the reference position. While the first volunteer shows a mean position in the upper right, the mean position of the second motion trace is close to the static reference profile.

The quality of standard tracking is depicted in fig. 5.8b. It is obviously dependent on the variation of the displacement (see figs. 5.7b and 5.7c). The blue-yellow halo at the outline of the intended (static) dose is the 2D analogy of tracking errors introduced in section 5.2.4. Yellow zones correspond to an overdosage outside the target, while blue areas mark the critical underdosages compared to the reference profile, which are to be alleviated. With a coverage measure of $\hat{D}$=0.9, these critical underdosages could be covered. This effect is qualitatively shown in fig. 5.8c. The cost of the increased coverage is an added overdosage outside the target area.

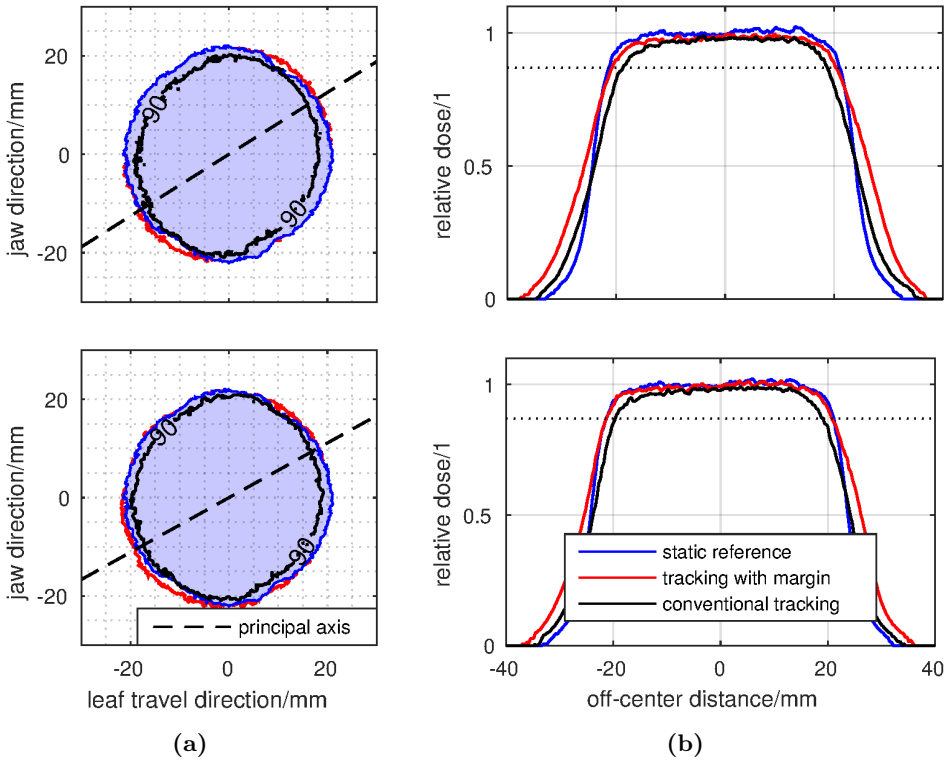

Figure 5.9: 1D/2D-dose profiles: left column (a) shows the 90 % contour line of the dose profiles in the case of reference (blue), tracked (black) and tracked with margin (red). The dashed lines show the principal motion axes. (b) displays the 1D profiles extracted from this. The dotted line indicates the 90% dose level.

In order to test the coverage quality with respect to $\hat{D} = 0.9$, 90%-contour lines from the doses of the test subjects are displayed in fig. 5.9a. The intended overlap between the 90% line of static reference and the margin-expanded tracked case is met in both cases. Deviations from this overlap can be observed at the intersection of an axis at 45°, which are likely caused by imperfect leaf-shaping due to the discrete size of MLC-leaves.

In fig. 5.9b, dose profiles along the axis of principal motion are displayed. As predicted by the dose model, the dose loss in the shoulders of both distributions could be compensated towards the selected confidence level. Spatial deviations between the 90% lines of static and margin-compensated tracking case are possibly caused by differences in output factor due to the moving aperture. These differences are especially visible in the profile of the first subject (fig. 5.9b, top).

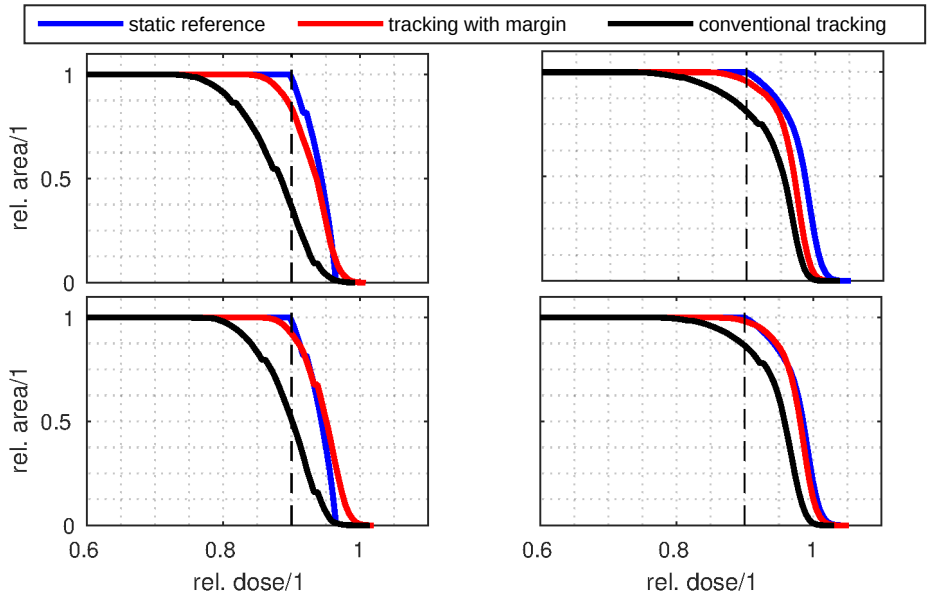

(a) $\hat{D} < D < 0.97$ **(b)** $\hat{D} < D$

Figure 5.10: DAH of both test cases (top and bottom row): (a) depicts the DAH-statistics in the shoulder of the dose distribution. (b) displays the DAH calculated over the area with reference dose $D > \hat{D}$.

Figure 5.10a shows the DAH in the shoulder of the 2D distribution above $\hat{D}$ of the reference dose distribution. Here, the amount of underdosage due to tracking errors is most crucial. Ideally, the margin-expanded tracking would show a rapid roll-off at 90 % relative dose, comparable to the static dose. In reality, the roll-off will shift, dependent on the accuracy of the compensation. For the two test cases, the DAHs confirm the improved coverage. While the uncompensated (no margin) tracking exerts an early roll-off in the shoulder of the DAH, early dose losses can be avoided using the margin expansion. However an early roll-off at about 85 % of the relative dose can be observed for both cases. The increased coverage is confirmed in the DAH of fig. 5.10b. However, the larger evaluation area which includes the dose plateau, reduces the coverage gain.

In table 5.1, quantitative DAH-parameters extracted from fig. 5.10 are shown. In the shoulder of the reference distribution ($\hat{D} < D < 0.97$), the $A_{90\,\%}$ point shows an increase of 47 % and 41 % for the two on-line experiments when comparing tracking with and without margins. The evaluation over the entire dose plateau ($\hat{D} < D$) shows an improvement in coverage of 14.5 % and 11.8 %, respectively.

Table 5.1: Quantitative coverage assessment: $A_{90\,\%}$ DAH-parameters of the dose coverage in conventional (index c) and margin-compensated (index m) tracking.

	$\hat{D} < D < 0.97$			$\hat{D} < D$		
volunteer	$A_{90\,\%,c}$	$A_{90\,\%,m}$	difference/%	$A_{90\,\%,c}$	$A_{90\,\%,m}$	difference/%
1	0.36	0.84	47.36	0.82	0.96	14.47
2	0.51	0.92	41.15	0.86	0.98	11.75

5.4 Discussion

The concept of on-line margin determination could be successfully implemented and tested on real-time hardware, with a mean running time of 22.89 ± 3.46 ms. This time included the estimation of the error distribution, margin extraction, segment dilation and segment prescription to the MLC. The experiments show that margin generation adapted to the requirements of a particular motion scenario is feasible.

The on-line motion tracking experiment showed good agreement to the expected coverage improvement with the used reference model. Due to the generally faster inhale velocities, larger errors occur in that direction as compared to the opposing (exhale) direction. The estimator is able to successfully account for these error anisotropies with an accordingly anisotropic margin.

In addition to the dose distribution data, DAH-evaluation showed a significant recovery of the dose within the area over $\hat{D}$ with an increase of $\mathrm{A}_{90\,\%}$ of 47.4 % and 41.1 % in the shoulder and 14.5 % and 11.8 % in the dose plateau of the reference dose.

Despite the adaptivity and the compliance of the measurements with the theoretical predictions, the results were obviously degraded by an imperfect dose model. This is observed best in fig. 5.9b, where the shift of aperture causes two effects: firstly, a changed dose plateau, which can be caused by unmodelled changes in scatter behavior of the linac head. Secondly, the otherwise overlapping 90 %-contours in fig. 5.9a show imperfect matching at the vertices of the circular aperture. At these points the leaf discretization becomes relevant during tracking, thus producing significantly different dose contours when comparing static and tracked doses.

The depth-dependency of the PGK showed by Low et al. (1995) is not addressed in this work. Due to the planar measurement, the measurement depth was kept constant for the experiments. However, when tracking targets immersed into a bulk (such as the abdomen), characterization of the depth-dependent penumbra might be prerequisite and its impact should be assessed. It is expected, that the PGK increases slowly with increasing depth (Metcalfe et al. 1993).

As shown by Falk et al. (2010), MLC-tracking enables a significant reduction of

safety margins at the planning stage. For residual tracking errors, the auto-adaptive character of the adaptive margin technique enables a generic compensation of induced underdosages, independent of the specific MLC tracking system or patient characteristics. An important constraint, however, is the validity of the training data within a unique set of machine and target geometry. If this correlation changes (e.g. by rotating the gantry, MLC angle), the training data is invalidated and the margin generator has to be retrained for the particular BEV. Another way to approximate stable training data is to change the machine-target geometry slowly enough to approximate a quasi-static transition. This could be performed e.g. by setting a fixed MLC angle along the main direction of displacement due to breathing, i.e. in CC direction. This implementation can be found in the Elekta MR-linac (Lagendijk, Raaymakers, and Vulpen 2014) and keeps the main motion axis parallel to the MLC leaf-travel direction. Accordingly, error statistics of the axis where the largest margin is applied can be considered to change very slowly (quasi-statically) with moving BEV. Although, the compensation of geometric error is only restricted by the field size of the MLC, additional safety interlocks should be triggered, once the geometric error exceeds a well defined level.

An important feature of the tracking margin generator concept is its design to retain target coverage based on machine error parameters, not on patient characteristics. The increased target coverage, obtained by the expanded segments, is accompanied by an overdosage in the area outside the original segment. This in turn implies that surrounding OAR, which are potentially spared with high conformality in the planning phase, may receive higher doses than intended due to the segment expansion. Equally, doses higher than 100 % can occur in target regions, when multiple segments of e.g. IMRT constructively interfere. In order to regularize these effects, leaf shaping algorithms which penalize OAR overdosages (Moore, Ruan, and Sawant 2016; Wisotzky, O'Brien, and Keall 2016) can be employed.

Intrinsically, despite the interference effects, the overall dose burden to OAR is expected to be significantly lower comparing to non-compensated methods such as the ITV concept (ICRU 83 2010). These integral dosimetry measurements should be addressed in future studies evaluating 3D dose distributions for tracked deliveries with and without automatic margin expansion on clinical IMRT-plans, e.g. using a dosimetry phantom such as Bedford et al. (2015). For practical purposes and because of the superior spatial resolution, film was used in this proof of concept.

The herein described on-line margin generator can be considered as an independent block between aperture prescription and MLC-hardware. If the target motion is predictable, a predictor module will be used to gap the deterministic latencies. Such predictability is exposed by structured motion (Ruan, Kupelian, and Low 2011) caused by regular breathing in the abdomen and thorax. A prediction module potentially increases the gradient in the slopes of the profiles fig. 5.9. The margin generator can then be attached to such a prediction module to correct for the non-deterministic (but stochastic) residual errors.

5.5 Conclusion

We developed and tested a margin generator for tracking error compensation in MLC tracking. The margin generator auto-adaptively imposes a tracking margin in order to retain a desired coverage level. The margin calculation uses statistics based on the patient motion and the ability of the machine to follow these excursions. This enables automatic adaptation to per-patient settings, disregarding tracking margins in the treatment planning stage. The proof-of-concept could show the feasibility of such a strategy. Future work will investigate the impact of this per-segment expansion on a delivered plan. Equally, the margin generator could be coupled with predictor algorithms. This would enable complementary compensation of systematic (predictable) and stochastic (unpredictable) errors.

Acknowledgements

MG, BDdS, JJWL, BWR and SPMC thank the ITEA (project 12026, SoRTS), the European Research Council (ERC-2010-AdG-20100317, Sound Pharma) and Elekta AB (Stockholm, Sweden) for funding.

MFF, SN and UO acknowledge support of the MLC tracking research from Elekta AB. MFF is supported by Cancer Research UK under Programme C33589/A19908. Research at The Institute of Cancer Research is also supported by Cancer Research UK under Programme C33589/A19727 and NHS funding to the NIHR Biomedical Research Centre at The Royal Marsden and The Institute of Cancer Research.

The authors would like to thank Dr. Michael Thomas (The Royal Marsden, London) for his contributions to the film dosimetry.

CHAPTER 6

Summary

On-board and on-line MRI in radiotherapy enables entirely new motion compensation paradigms in the field. Previously, multiple imaging modalities were employed in an alternating or concurrent fashion to cover the different requirements of imaging speed, quality and resolution for motion compensated IGRT. MRI offers superior flexibility in temporal and spatial domains along with unmatched soft-tissue contrast. Therefore it consolidates all aspects of IGRT into one device, the MR-linac. This thesis discusses attempts to detect and mitigate target motion within the context of the current MR-linac design.

The sensitivity of deformable image registration to changes in image resolution was investigated in **chapter 2** in order to achieve accelerated on-line MR imaging. 3D datasets of the abdomen in exhale-state were thus acquired over long durations, obtaining ground-truth datasets. Afterwards, these 4D datasets were gradually downsampled in all spatial directions to simulate a decrease of resolution and thus an approximately quadratic decrease of image acquisition times. The results showed that deformable image registration is remarkably data sufficient in terms of image resolution. When degrading the image resolution by a downsampling factor of 2 ($(5\,\mathrm{mm})^3$ voxel), the motion estimation differed only as much as 1.5 mm RMS over a representative set of voxels. Furthermore, local variations of salient pixels showed absolute errors of around 0.5 mm only, compared to ground-truth. These results suggest that low-resolution imaging is sufficient for the purpose of motion estimation. Therefore a promising and relatively uncomplicated way to accelerate on-line MRI has been found.

Chapter 3 addresses the ability of the novel on-line imaging feature of an MR-linac to observe the anatomy during ongoing treatment. The MRI was used in a multiplexed manner, using fast 1D imaging for respiratory motion compensation and 3D imaging to volumetrically observe the anatomy during treatment. Two

plan deliveries were simulated on the continuous MRI datasets of volunteers. Subsequently, the dose deliveries were reconstructed based on the observed anatomic motion during MR imaging. The feasibility of dose tracking using the proposed method was shown by comparing the reconstructed doses to the initial plan dose. While DVH statistics of target and OAR structures did not reveal significant differences during delivery, point-wise differences showed large local deviations of -2.3/+1.5 Gy (-11.5 %/+7.5 % of the target dose) in the PTV. Furthermore, the dose reconstruction showed local variances of up to 10 % of the target dose in OAR such as the liver. The implemented technique proves the feasibility for tracking local dose differences using on-line MRI in highly mobile regions, such as the abdomen. Furthermore, it was shown that global metrics such as DVH alone are not able to resolve these local differences and are thus insufficient for a detailed quality assessment of a delivered plan evaluated using on-line MR imaging during treatment.

The MLC built into the MR-linac is designed to rapidly adapt its aperture in dynamic delivery such as volumetric intensity modulated arc therapy (VMAT). Optimally, the same agility can be employed to adaptively track the target position during a treatment with on-line imaging. For the investigation in **chapter 4**, an exemplary imaging pipeline was implemented, simulating fast on-line imaging. A simple MLC aperture was locked onto a target moving in a sinusoidal fashion, covering a relatively large parameter field in amplitude and period. Indirect measurement yielded an isolated MLC hardware lag of 15.9±6.6 ms and a loop delay of about 110 ms for the entire imaging pipeline. The lag due to the inertia of heavy MLC leaves was shown to be remarkably low and accounted only for a minor fraction of the lag of the imaging and data processing. The dosimetric advantage of tracking physiologic motion was tested using dosimetric film which was moved according to a motion pattern extracted from a volunteer's abdominal cine-MRI. Both local and global dosimetric measures showed large improvements. γ passrates (1 %/1 mm, 10 % low-dose exclusion threshold) as low as 49 % due to the physiologic motion could recover to 92 % by turning on target tracking using camera-based feedback.

The imperfect response of the dynamic system during MLC tracking causes geometric mismatches between target position and position of the MLC aperture. In **chapter 4** several errors could be determined with high certainty, such as latencies due to image processing. Others, such as the inertia-limited response of the MLC system to more complicated motion than simple sinusoids, are less deterministic and are better described by a statistical measure. For **chapter 5**, a tracking error mitigation technique based on such a statistical error description was implemented. An algorithm with 23 ms running time evaluated the statistical error between actual target position and current MLC aperture position in real-time. Subsequently, the dosimetric impact of such a geometric error was estimated. Similar to the PTV margin concept, a tolerated dose error (10 %) was preset and used to derive an on-line tracking margin which was imposed onto the prescribed segment. The real-time loop was tested on a modelled imaging pipeline with 300 ms latency, actual MLC hardware and motion according to two volunteers'

breathing excursions extracted from fast MRI. The algorithm showed its ability to limit the target dose error attributed to delays and machine imperfections to the preset value of 10 %. In the edges of the dose distribution, the area receiving more than 90 % of the target dose could be increased by more than 40 % as compared to the measurement without tracking margins. This indicates a large increase of target coverage using tracking margins. According to the target coverage optimization, the accompanying overdosage effects were optimally limited.

CHAPTER 7

General discussion

The ability to spatially resolve the anatomy at the treatment site is a prerequisite of IGRT, and improving this capability has been one of the driving forces of innovation in radiotherapy. In current radiotherapy practice MRI is increasingly employed complementary to CT for its high contrast in soft tissue. With its wide parameter field, MRI can be tuned to obtain near-ideal contrast on many target sites, which results in optimal distinction of target volumes and surrounding tissue for treatment planning. The integration of MRI thus comes close to the currently achievable clinical optimum.

With motion compensation on the MR-linac, there are different requirements to increase target conformity in different treatment sites. For continuously and periodically moving targets in the thorax and abdomen, active, real-time motion mitigation strategies such as gating and MLC tracking are naturally suitable solutions. These automatic methods are increasingly gaining ground clinically (Keall et al. 2006b; Giraud and Garcia 2010; Booth et al. 2016). In other treatment sites, the occurrence of motion is sparse and unpredictable. These types of motion are caused by physiologic processes (Ghilezan et al. 2005; Kleijnen et al. 2016) or changes in patient position (Heijst et al. 2016). To estimate the geometric and thus dosimetric impact of such variations, continuous volumetric observation of the target and its surroundings is a sensible alternative. This paradigm especially holds for hypofractionated schemes, where occasional motion can potentially lead to large dose variations. The detected variations can be taken into account in a subsequent, periodic re-planning or decision phase. Depending on the fractionation scheme, these corrective phases must be applied between or within treatment sessions.

In an on-line setting, MRI grants access to a treatment regimen in which it is possible to continuously observe volumetric data with unmatched soft tissue contrast

during treatment and without the need for internal or external position surrogates. This transition has the potential to not only track the target position over time, but also to resolve the entire irradiated tissue surrounding the target, i.e. to *see what you treat*. Technical solutions are needed to account for the specific requirements of the individual treatment sites and the parameters of on-line MRI.

7.1 On-line motion monitoring

This thesis proposes technical solutions regarding the temporal constraints of the MR imaging, translating it from a purely diagnostic modality to an on-line IGRT modality.

As an input for treatment planning, a regular time slot for MRI takes about 30-40 min. The session incorporates sequences of different contrasts for complementary planning information. Using on-line MRI in a real-time setting, these acquisition intervals are neither desirable nor acceptable, as anatomy changes occur within periods of minutes down to sub-seconds. The requirement to resolve these events near-*Nyquist*[1] puts hard constraints on the imaging sequences, dramatically reducing their degrees of freedom in terms of contrast and resolution. Compared to diagnostic imaging, however, the requirements with regard to image content also change for motion tracking imaging.

Rather than providing highlighted anatomic features to a human observer, imaging for motion tracking serves as an input for automatic motion estimation methods such as deformable image registration (DIR) to extract anatomy changes from the continuous image stream. **Chapter 2** demonstrated that, while image resolution is a key figure for human observers, it is an insensitive parameter for the quality of motion tracking by means of DIR. Unsuitably slow MR imaging sequences can thus be boosted to acquisition speeds suitable to resolve anatomic changes, especially in 3D. To this day, despite suggestions otherwise (Plathow et al. 2005; Sawant et al. 2014), native 3D MRI covering large VOIs is generally unsuitable to track anatomy affected by fast processes such as breathing. While CT acquisitions simply blur, motion during conventional image encoding in MRI results in ghosting of the moving structures into the entire field of view (FOV). The generated data is thus difficult to read for a human observer and even more difficult to interpret by means of DIR, rendering it useless for subsequent processing blocks such as dose reconstruction. In these cases, knowledge of the physiology of respiration can be taken advantage of as shown in **chapter 3**, where the MR image acquisition is triggered in the relatively motionless end-exhalation plateau. For dose delivery, the same principle, i.e. beam gating, was used. Respiratory gating is already clinical practice in both MRI and motion compensated radiotherapy and has a transparent working principle. Therefore, the presented gated delivery and imaging technique is expected to be translated onto the MR-linac, providing motion compensation and continuous dose tracking in abdominal and thoracic sites.

[1] The Nyquist-Shannon sampling theorem states that the sampling frequency has to exceed the frequency of the sampled signal at least twice.

7.1.1 Motion models

Rapid acquisition of 3D data is limited by the physical constraints of MRI. To resolve these complications, motion models are employed which estimate volumetric images by use of inference. In the training phase, motion models are established based on retrospectively sorted 4D image series, ideally acquired right before each treatment session. In the inference phase, fast internal or external surrogates of lower dimension are used to control the model. The motion model then returns full 3D images, according to the state of surrogate. Techniques strictly interpolating retrospectively acquired 4D datasets are hampered by the assumption of reproducibility between the training phase and subsequent inference phase, which may not be justified due to baseline variations or changes in breathing pattern (Plathow et al. 2006; Siebenthal et al. 2007a). Parametric correspondence models which have the ambition to overcome this strong reproducibility requirement are currently under development (King et al. 2012; Stemkens et al. 2016b).

Used on-line, motion models for either target tracking or dose reconstruction will be required to provide a channel for a real-time confidence metric. A well designed confidence metric would rapidly detect the quality of data provided by the motion model and indicate a faulty state to both the operator and the motion compensation algorithm. This sanity check is necessary to prevent faulty target positions or erroneously inferred image volumes from being propagated into the feedback loop. The only reasonable action in response to a detected loss of inference would be an immediate beam-off, followed by an observation-only phase or model retraining. In current literature, potential confidence metrics calculated from the surrogate itself or additionally acquired validation data were reported (King et al. 2012; Stemkens et al. 2016b). The metric was obtained by comparing this acquired ground-truth data against the inferred data. In addition, motion can be observed using redundant sensors, such as respiratory bellows (Santelli et al. 2011) or optical systems (Freislederer et al. 2015) to independently test the motion model for exception states. As this data is sampled rapidly, a fast quality indicator can be realized, providing a metric for responsive exception gating in case of unforeseen events, such as coughing or whole body motion.

To adapt to slow changes such as drift, the motion model should provide means for continuous retraining using data which reflects a particular situation as well as possible. To this day, model updates are achieved either by integrating the incoming surrogate data or using additional, concurrently sampled data (Celicanin et al. 2015; Baumgartner et al. 2017).

7.1.2 Rigid target tracking

Contrary to 3D dose tracking, imaging for target tracking is more data sufficient in the sense that only the target position is of interest. For target tracking applications, fast 2D imaging is therefore a sufficient alternative to 4D inference models. New schemes for excitation and sampling combined with reconstruction techniques have shifted sliced 2D MRI into frame rates that fulfill the *Nyquist* criteria for resolving fast physiologic processes such as breathing (Pruessmann et al.

1999; Larkman et al. 2001; Breuer et al. 2005; Zhang, Block, and Frahm 2010; Borman et al. 2016). It is noted that, in order to optimally cover the main components of target motion, preknowledge about motion physiology can be employed, e.g. by choosing the optimal slice position for a specific site (Moerland et al. 1994; Heerkens et al. 2014).

7.1.3 Automatic motion estimation

Considering the fast image acquisition frequency, the use of automatic DIR is a requirement for the processing of on-line MR images. Despite the vast literature body (Oliveira and Tavares 2014), the validity of DIR for radiotherapy is still subject to discussion (Schultheiss, Tome, and Orton 2012).

A major pitfall of DIR is geometric validation since it is hard to obtain for a general case. However, individual DIR implementations can be tested for geometric accuracy by comparing the estimated motion to the displacement of a geometric ground-truth in dynamic datasets. Manually or automatically detected point pairs based on anatomic landmarks can be used for point-wise comparisons (Østergaard Noe et al. 2008; Paganelli et al. 2013). Furthermore, volume metrics such as Dice similarity coefficient or contour difference statistics provide quantitative assessment of geometric validity of the motion estimation. The accuracy of DIR can be controlled not only by the parameterization of the DIR functional, such as α proposed by Horn and Schunck (1981). In fact, it can be influenced greatly by the variable contrast and resolution of MRI. Tailoring the MR contrast for DIR is an interesting field of research, providing the additional degrees of freedom necessary to obtain optimal geometric accuracy.

After validation for a specific image contrast, the on-line evaluation of DIR performance is crucial for both real-time guidance and dose reconstruction. Therefore, quality indicators are necessary to rate the performance of DIR during therapy. Using a pre-set upper boundary, RMS difference metrics between images obtained by rigid registration and by DIR can be used to monitor the quality of the registration. Together with continuously displayed difference images, an on-line quality indicator can easily be implemented. However, while feasible in sliced acquisitions, continuously probing 3D difference images in all dimensions is not feasible for a human operator. Thus, automatic metrics that quantify the performance of DIR, such as inverse consistency errors and transitivity errors, have been proposed in the literature (Bender and Tomé 2009; Bender, Hardcastle, and Tomé 2012). Monitoring these indicators allow on-line watchdogs or the operator to inhibit further DIR-based treatment, in case of doubtful quality.

7.2 On-line motion compensation

Changing the treatment based on the stream of motion information closes the feedback loop. Generally, two adaptation regimen can be distinguished at this point, i.e. real-time machine feedback and plan adaptation schemes, which will be discussed below. Technically, the response time requirement is the main difference

between the two approaches, as the real-time feedback response demands quick, automated decisions based on the incoming data. However, with increasing automation and machine autonomy, immediate clinical risks are increasingly hard to identify and clarify. In addition to the real-time feedback for therapy control, new channels for treatment safety and QA measures have to be devised accordingly in order to translate the autonomous treatment control into the clinic.

7.2.1 Real-time machine feedback

As an input for real-time therapy decisions, rapidly acquired MR images are optimal. **Chapter 3** showed that navigator echoes and beam gating are a viable entry point for motion compensated treatment on the MR-linac, both from a delivery and an imaging point of view. The clinical feasibility of MR-guided gating has been demonstrated using the ViewRay system, tracking the position of a precontoured target on 2D slices and triggering the beam based on the target translations (Kashani et al. 2014; Santanam et al. 2015).

For the MR-linac design herein, real-time feedback based on slices is being investigated. Applications of MRI-guided high intensity focused ultrasound (HIFU) (Hynynen et al. 1996) showed that target tracking using DIR on images acquired from similar, diagnostic field strengths are technically feasible. In conjunction with rapidly updated MR images, Ries et al. (2010) demonstrated a pipeline for real-time therapy feedback in abdominal HIFU interventions using fast imaging and automatic motion estimation based on DIR. The target tracking paradigms therein are almost seamlessly portable onto the MR-linac. In the preparation phase, user interaction will be limited to selecting one or multiple motion surrogate points on pre-treatment intervention planning images. Accordingly, the deformation vectors extracted by DIR in these points will trigger and steer machine action by means of beam gating and tracking.

The individual delays of the subcomponents in the cascade of a therapy feedback loop, i.e. image acquisition and transport, image processing and the eventual machine action (**chapter 4**), cause a latency between an anatomic action and the machine's reaction. This latency causes a geometric mismatch and thus eventually a dosimetric mismatch, largely depending on the length of the delay. Therefore, the detailed analysis of latencies is necessary to characterize the real-time performance of the feedback loop.

At the lower end of machine complexity, the latency of beam gating (**chapter 3**) can be treated as a mere addition of the separate latencies of each individual module. Using highly parallel GPU implementations, the running time of motion estimation in 2D can be limited to values as low as 10 ms (Roujol et al. 2010). Also, gating the electron gun of a linac shows good beam switching performances of under 50 ms, as shown in fig. 7.1b. However, considering the performance figures of MR imaging reveals the latency bottleneck of the feedback pipeline: in addition to a 60 ms offset due to transport and reconstruction, an estimated $T_{acquisition}/2$ has to be added for the actual imaging process (fig. 7.1a). Furthermore, upon feedback,

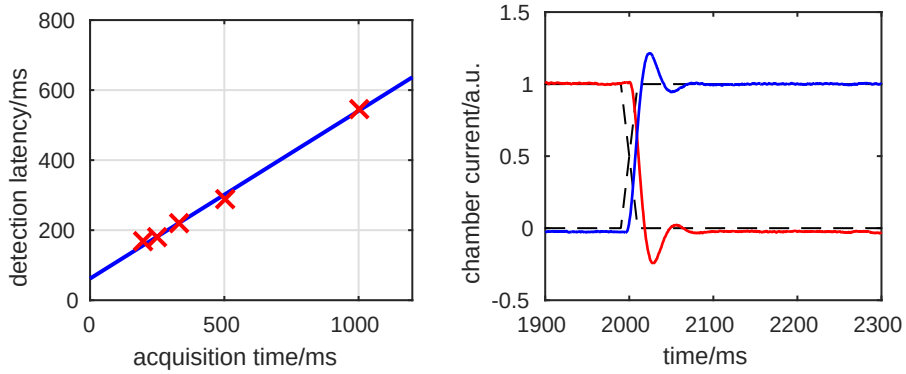

(a) Acquisition latency **(b)** Gating latency

Figure 7.1: (a) depicts the latencies of the on-line MRI of an MR-linac. The plot shows the measured latencies as a function of imaging rate (×) and a linear fit (solid blue) (adapted from Glitzner et al. (2017b)). (b) shows the response between a TTL gating command on the electron gun (GATE EN, dashed) and the delayed response of an ionization chamber in the beam path. The impulse response of the chamber is apparent for both ON (blue) and OFF (red) events (*unpublished results).*

the average age of a sampled target position point, $T_{acquisition}/2$, also has to be accounted for (Poulsen et al. 2010). After summation, the mean contribution of MRI to the feedback latency is then (60 ms + $T_{acquisition}$), i.e. 310 ms for 4 Hz MRI. Including the beam switching delay for gating, this estimation of the latency of the overall feedback loop is in the range of 350 ms, comparable with previously reported values of MRI-guided IGRT (Santanam et al. 2014; Santanam et al. 2015). A preliminary estimation of the total feedback latency of MLC tracking yields similar results, considering the small MLC hardware latency of under 20 ms as a reaction to periodic motion as shown in **chapter 4**.

With a loop latency of under 500 ms, gating and tracking on the MR-linac is feasible for motion compensation, according to the AAPM Task Group 76 report (Keall et al. 2006c). However, considering the large latency contribution of imaging, acceleration techniques for acquisition and reconstruction have to receive most attention, as they promise the best leverage to reduce the overall latency in an MRI-guided feedback loop. A very suitable method for acquisition time reduction using reduced spatial sampling was presented in **chapter 2**.

For the evaluation of MLC tracking on the MR-linac, new dosimetric parameters have to be taken into account. Besides the influence of the static magnetic field on the dose distribution, the photon beam of the MR-linac is, in contrast to conventional linacs, flattening filter free (FFF). In MLC tracking on conventional linacs, the photon fluence through a segment is assumed to be independent of the position of the segment. The flatness of the beam is thus, together with the rigid body

motion, the major assumption of performing MLC tracking. Accordingly, the impact of the FFF configuration on the MR-linac has to be taken into account when evaluating the tracking capability. To this point, simulation studies investigating the feasibility of tracking on the MR-linac did not find any adverse effects caused by the new dosimetric parameters (Menten et al. 2016).

7.2.2 Real-time machine errors

The increasing degree of real-time automation requires well-defined limits, i.e. action radii, up to which the feedback loop can operate and compensate or tolerate errors. As for the case of motion models and automatic motion estimation, indicators for machine errors are necessary, as well as counter measures compensating for these errors in real-time. The error indicators will give real-time reports about the quality of motion compensation to both the feedback loop and the operator. A detected breach of quality, e.g. due to patient reflexes, will instantaneously trigger an inhibit by the feedback loop itself or the operator.

To a certain extent, the feedback loop must be allowed to tolerate and autonomously compensate for machine errors. In **chapter 5**, an error metric was developed, which evaluates the performance of an MLC tracking system in real-time. The method autonomously compensates geometric errors by adding an appropriate error margin on top of the desired aperture. Applied in a treatment, however, only finite error margins can be tolerated to retain the OAR sparing, which was the incentive for MLC tracking in the first place. An obvious break condition could be an action VOI, shaped as a structure similar to an ITV: once parts of the projected aperture exceed the structure, the beam is automatically switched off and user interaction is required.

Assuming structured, periodic motion such as breathing and knowledge of the latencies of at least parts of the feedback chain, enables the application of prediction algorithms (Ruan 2010; Ruan, Kupelian, and Low 2011). Based on models of retrospective data [x(t), x(t-t_1), x(t-t_2),...,x(t-t_N)], these methods extrapolate the future position $\hat{x}(t+T)$ of a motion surrogate at time T ahead and can thus reduce the dosimetric errors due to latencies. One way to evaluate the quality of the prediction, an estimated target position $\hat{x}(t+T)$ can be compared to the actual value x(t+T) at time T later. Considering the approximated loop latency of 350 ms, this makes the performance indication fast and simple. Observed prediction errors can then be either tolerated or can serve as an input to on-line adapted margins presented in **chapter 5**. Continuous exceedance of set tolerance range, on the other hand, will point to a violation of initial requirements (e.g., periodic motion) and will raise an inhibit. The operator will then have to re-evaluate the purpose of the prediction, especially compared to a non-predicted scenario.

7.2.3 Dose reconstruction

In **chapter 3**, it was shown that on-line MRI can be used to reconstruct the difference between previously delivered doses and the planned dose. Analysis of

the differential dose helps to grade the quality of an already delivered fraction in a dosimetric sense, by comparing the planned dose to the actually delivered dose. This enables patient specific, dose-based plan QA and can assist planning decisions, e.g. by indicating a need for additional motion compensation or a necessary change of margins. Furthermore, the already applied differential dose map can be taken as an input for the adaptation of the treatment plan for the remaining therapy course, as discussed later on. As the continuous acquisition of 3D datasets can be challenging for rapid anatomy changes, the sub-second resolution requirement in abdomen or thorax is a prime case for parametric motion models. Figure 7.2 depicts the 4D dose reconstruction of a single radiotherapy fraction to the kidney using a currently developed motion model (Stemkens et al. 2016a).

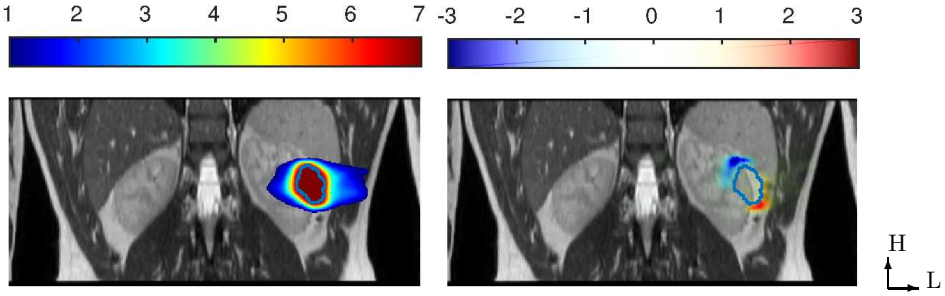

(a) d_{plan}/Gy **(b)** ($d_{reconstructed}$-d_{plan})/Gy

Figure 7.2: Post-fraction dose reconstruction using a 4D motion model. (a) shows the colorwash of planned dose d_{plan} for the fraction on the mid-position anatomy. The PTV is contoured in blue. Anatomy drifts during treatment resulted in a shift between reconstructed dose ($d_{reconstructed}$) and planned dose (b) (adapted from Stemkens et al. (2016a)).

Dose reconstruction heavily relies on DIR for two purposes. Firstly, to generate a new ED map from an initial CT dataset, adapted to the change in anatomy, detected by the MRI. Secondly, to warp the dose calculated on the temporary CT grid back onto the planning grid. The use of DIR for dose reconstruction is debated in radiotherapy, partly because of geometric uncertainties in general but also because physiologic effects such as weight loss, tumor regression, swelling or bowel filling cannot be fully reflected in the functionals of DIR used for dose reconstruction. Furthermore, from a biological point of view, the effect of variable tissue density must be added to that list, potentially causing misleading motion estimations and thus erroneous dose reconstructions (Schultheiss, Tome, and Orton 2012).

Nevertheless, dose reconstruction is a principal workflow element as radiotherapy makes the transition to hypofractionated, ablative therapy schemes. Compared to conventional IGRT, on-line DIR-based dose reconstruction can finally reject unreasonable assumptions such as rigid body shift or internal target shifts. To improve confidence in the technique it is crucial to extend the geometric validation of DIR and include comprehensive dose reconstruction benchmarks into the regular QA process. This process should contain an end-to-end dose reconstruction workflow,

i.e. physical deformation, radiation, DIR, dose reconstruction and dose readout. It is crucial, however, that the dosimetry setup does not interfere with the sensitive DIR. Potential point-wise sampling methods such as MOSFETs and ionization chambers (Jaffray et al. 2010), however, would have direct impact on the quality of DIR, as they inherently generate image contrast in the MRI. In contrast, dosimetric gels are ideal candidates for end-to-end QA, allowing for both deformation and volumetric readout using MRI without interference of external sensors (Schreiner 2004; Yeo et al. 2013).

7.2.4 Plan feedback

With sufficient spatio-temporal resolution and spatial coverage, reconstructed differential doses can be fed back to the planning system. Ideally, in an on-line setting, an entirely new plan is automatically created, accounting for the already delivered dose and the anatomy in its last known state. The branching point and frequency of plan recalculation strongly depends on the data processing speed. It ranges from interfraction down to an intrasegment resolution. A solution for an intersegment adaptive replanning system was recently developed by Kontaxis et al. (2015b), which proved its ability to account for intrafraction anatomy changes in an off-line setting (Kontaxis et al. 2015a).

To translate this technique into an on-line setting, acceleration of the computationally expensive generation of beam influence data is necessary (Bol et al. 2012). Until on-line replanning is able to be performed following every differential anatomy change in real-time, combination schemes situated between direct machine control and plan adaptation will be useful and necessary to test subcomponents such as dose reconstruction. These intermediate solutions are feasible and practicable preparation steps towards the ideal, and can be used for triggering off-line re-plan decisions (Fast et al. 2016; Kamerling et al. 2016).

7.3 Conformity by autonomy

This thesis discusses options to achieve better conformity during EBRT treatment using MRI as a concurrently running imaging of diagnostic quality. The wording *on-line* is used throughout and is synonymous to *concurrent*, in contrast to *on-board* in current clinical EBRT.

In current clinic, the benefit of *seeing what you treat* is obvious, especially with regards to set-up uncertainties, since it allows to align the plan directly on the target. The tendency of the field towards hypofractionated and ablative treatment courses defines a new regimen with ever less tolerance for uncertainties. As the dose per fraction increases, small changes in anatomy *intra-fraction* could cause significant dose errors. Equally, the general use of excessive, toxicity-inducing planning margins becomes unviable. In order to retain optimal conformity, on-line imaging must be employed and fed back to a responsive therapy control system, which autonomously decides on delivery adaptations according to the anatomy changes.

Respiratory gating for treatment in the abdomen or thoracic sites is the most basic and comprehensible method of on-line autonomous delivery adaptations and owes its clinical success to its simplicity of both the technique and the underlying motion. MLC tracking has the aspiration of increasing the treatment efficiency. However, it is conceptually complex, as the treatment beam is not only turned on and off, but also moved on-the-fly. For a potential translation into the clinic, this adaptivity requires a tightly constrained workflow and a fully characterized machine undergoing stringent QA (Sawant et al. 2010). Additionally, the discussed on-line safety measures (sections 7.1 and 7.2) allow to monitor the quality of the machine decisions in real-time, causing immediate exception gating when decisions are out of bounds. The potential failure effects can thus be kept to a clinically reasonable limit, while benefiting from the large increase in dose conformity. Compared to the surrogate-based gating and tracking methods currently used in clinical trials, the MR-linac boasts superior image quality and image content. In addition to the subsequently expected technical improvement, further clinical confidence is added by providing continuous, high-contrast images of the target anatomy to the operator.

Dose reconstruction based on on-line MRI potentially allows to continuously observe delivered dose distributions. Initially, manual replanning can thus be achieved by subtracting delivered doses from originally planned doses. This is particularly useful for sites moving sparsely, rather than periodically. Fraction by fraction, the delivered dose then converges to the planned dose, under constant supervision of the clinician. Clinically advantageous, ablative treatment courses will require to speed up the creation of new treatment plans according to rapidly detected dose differences. Ultimately, as replanning occurs *intra-fraction*, manual plan validation would become unfeasible. This regimen requires automatic on-line replanning, autonomously and continuously generating new, optimal treatment plans. Compared to the previously discussed purely geometric concepts such as gating and tracking, the level of complexity increases due to the large number of involved subcomponents (section 7.2.4). However, analogous to the geometric concepts, the quality of service of every individual subcomponent can be monitored by QA measures and watchdog procedures. Initially, the output of dose reconstruction alone will have to be offered to the clinic for manual plan feedback in order to gain confidence in the workflow. From this point on, as seen for gating and tracking, small cohort patient studies will have to be performed to realize the potential of the technique in terms of clinical endpoints.

HOOFDSTUK 8

Samenvatting

Met de komst van MRI on-line, d.w.z. terwijl de patiënt bestraald wordt, zijn geheel nieuwe benaderingen mogelijk voor het compenseren van beweging bij radiotherapiebehandelingen. Conventioneel worden verschillende beeldvormingstechnieken ingezet, na elkaar of tegelijkertijd, om de verschillende doelen te bereiken die nodig zijn voor bewegingsgecompenseerde IGRT. Het gaat hierbij met name om snelheid, kwaliteit en resolutie van de imaging. MRI biedt een superieure flexibiliteit in zowel het temporele als spatiële domein, alsmede een zeer hoog contrast de weke delen. MRI vormt daarmee een ideale kandidaat om alle genoemde aspecten die benodigd zijn voor IGRT in één apparaat te verwerken: de MR-linac. In dit proefschrift worden verschillende manieren beschreven, in de context van het huidige ontwerp van de MR-linac, die de beweging van doelvolumina proberen te detecteren en het effect van deze beweging te verminderen.

Sensitiviteit van DIR voor veranderingen in beeldresolutie wordt beschreven in **hoofdstuk 2**, waarbij het doel was om versnelde on-line MRI mogelijk te maken. We hebben 3D datasets van het abdomen gemaakt, in uitademing, over een langere periode, die de ground truth datasets vormden. De volgende stap was om de 4D data te downsamplen in de drie spatile richtingen om een afname in resolutie te simuleren, en daarmee dus een afname in acquisitietijd te krijgen, die bij benadering kwadratisch is. De resultaten van dit hoofdstuk laten zien dat DIR opvallend goed blijft werken bij een reductie van de beeldresolutie. Als de resolutie een factor 2 omlaag gaat ($(5\,\mathrm{mm})^3$ voxel), is het verschil in afgeschatte beweging slechts 1.5 mm RMS, gekeken over een representatieve set voxels. Ten opzichte van de ground truth vonden we bovendien lokale absolute afwijkingen van slechts maximaal 0.5 mm. Dit toont aan dat laag-resolute imaging voldoende kan zijn om een goede afschatting van beweging te maken. We hebben dus een veelbelovende en relatief gemakkelijke manier gevonden om on-line MRI te versnellen.

Hoofdstuk 3 beschrijft waarneming met MRI van de bewegende anatomie gedurende een behandeling. Dit kan aan de hand van een nieuwe on-line imaging-methode op de MR-linac. Hiervoor hebben we MRI op een veelvoudige manier gebruikt: snelle 1D-imaging voor het compenseren van ademhalingsbeweging, en 3D-imaging om het volume van de anatomie tijdens de behandeling in beeld te brengen. We hebben twee dosisplannen gesimuleerd op de continue MRI-datasets bij vrijwilligers. Vervolgens hebben we de afgeleverde stralingsdoses gereconstrueerd aan de hand van de anatomische beweging op MRI. Door het vergelijken van het oorspronkelijke dosisplan met de gereconstrueerde dosis, kunnen we concluderen dat het haalbaar is om op de beschreven manier dose tracking te doen. Hoewel de verschillen in DVH-parameters voor doelgebieden en OAR tijdens de dosisafgifte niet significant waren, zagen we in het PTV grote lokale afwijkingen van -2.3/+1.5 Gy (-11.5 %/+7.5 % van de PTV-dosis) op voxelniveau. Bovendien zagen we in de gereconstrueerde dosis, in OAR zoals de lever, lokale varianties tot op 10 % van de voorgeschreven PTV-dosis. Hiermee hebben we dus laten zien dat het haalbaar is om met on-line MRI lokale dosisverschillen in zeer beweeglijke regios, zoals het abdomen, te tracken. Bovendien hebben we aangetoond dat globale statistische parameters, zoals alleen een DVH, niet genoeg zijn om deze lokale verschillen op te lossen. Deze zijn dus niet geschikt om een gedetailleerde kwalititeitsanalyse van een afgeleverd plan te evalueren met on-line MRI.

De MLC die in de MR-linac is gemonteerd is zodanig ontworpen dat de opening ervan dynamisch en snel aangepast kan worden, bijvoorbeeld voor het toepassen van VMAT. In het ideale geval zou deze beweeglijkheid gebruikt kunnen worden om op een adaptieve manier de positie van een doelvolume te tracken gedurende de behandeling, met behulp van on-line imaging. In **hoofdstuk 4** wordt een voorbeeld van een imaging-pipeline beschreven, waarbij snelle on-line imaging is gesimuleerd. We hebben een eenvoudige MLC-opening gericht op een doel, dat in een sinusvorm beweegt, met uiteenlopende waarden in amplitude en frequentie. Een indirecte meting liet daarbij zien dat een lag van alleen de MLC-hardware 15.9±6.6 ms was, en de loop delay van de gehele imaging-loop ongeveer 110 ms bedroeg. De lag als gevolg van de traagheid van zware MLC-leaves bleek opmerkelijk klein te zijn, en had als gevolg ook maar een zeer kleine bijdrage aan de totale lag van de imaging en dataverwerking. Het tracken van fysiologische beweging kan dosimetrisch gezien zeer voordelig zijn. We hebben dit getest door een dosimetrische film te laten bewegen aan de hand van een bewegingspatroon dat op cine-MRI-data in vrijwilligers is bepaald. Zowel lokale als globale metingen lieten grote dosimetrische verbeteringen zien. De γ pass rates (1 %/1 mm, 10 % lage-dosis exclusiedrempel), die soms niet hoger dan 49 % waren - als gevolg van fysiologische beweging - konden omhoog gebracht worden tot wel 92 %, door het tracken van het doelvolume aan de hand van camerabeelden.

Als gevolg van de niet-perfecte mechanische reactie van de verschillende dynamische onderdelen bij MLC-tracking kunnen er geometrische fouten optreden tussen de positie van het doelvolume en die van de MLC-opening. In **hoofdstuk 4** hebben we verschillende fouten bepaald, met hoge zekerheid, zoals de latency die samenhangt met de beeldverwerking. Andere foutenbronnen, bijvoorbeeld door de

traagheid van het MLC-systeem die toeneemt naarmate bewegingspatronen ingewikkelder worden, zijn minder deterministisch en kunnen daarom beter beschreven worden met een statistische maat. In **hoofdstuk 5** wordt een techniek beschreven die de fouten bij tracking moet verkleinen aan de hand van een dergelijke statistische beschrijving. Daarbij hebben we een algoritme gebruikt, met een looptijd van 23 ms, dat de statistische fout evalueerde tussen daadwerkelijke posities van het doelvolume en de huidige MLC-opening, in real-time. Vervolgens hebben we de dosimetrische impact van zulke geometrische fouten bepaald. Analoog aan het concept van een PTV-marge lieten we een dosimetrische fout toe (vooraf bepaald op 10 %) om een on-line tracking-marge af te leiden, die op het segment werd opgelegd. De real-time loop hebben we getest op een gemodeleerde imaging-pipeline met 300 ms latency, met de daadwerkelijke MLC-hardware, waarbij de beweging is bepaald aan de hand van MRI-data van twee vrijwilligers met verschillende ademhalingspatronen. Het algoritme liet zien dat het de fout in dosis op het doelvolume, als gevolg van vertragingen en onvolkomenheden in de apparatuur, inderdaad kon beperken tot de vooraf bepaalde waarde van 10 %. Aan de randen van de dosisverdeling bleek dat het gebied dat meer dan 90 % van de voorgeschreven dosis krijgt tot wel 40 % groter kon worden, ten opzichte van de situatie zonder trackingmarges. Dit resultaat laat zien dat de coverage van de dosis aanzienlijk groter kan worden als deze speciale tracking-marges worden toegepast. Bij het optimaliseren van de coverage hebben we de overdosis minimaal kunnen houden.

Bibliography

Ahnesjö, A. and Aspradakis, M. M. (1999). "Dose calculations for external photon beams in radiotherapy". In: *Phys. Med. Biol.* 44.11, pp. 99–155.

Baker, S., Scharstein, D., Lewis, J. P., Roth, S., Black, M. J., and Szeliski, R. (2011). "A database and evaluation methodology for optical flow". In: *Int. J. Comput. Vis.* 92.1, pp. 1–31.

Barron, J. L., Fleet, D. J., and Beauchemin, S. S. (1994). "Performance of optical flow techniques". In: *Int. J. Comput. Vis.* 12.1, pp. 43–77.

Baumgartner, C. F., Kolbitsch, C., McClelland, J. R., Rueckert, D., and King, A. P. (2017). "Autoadaptive motion modelling for MR-based respiratory motion estimation". In: *Med. Image Anal.* 35, pp. 83–100.

Beckham, W. A., Keall, P. J., and Siebers, J. V. (2002). "A fluence-convolution method to calculate radiation therapy dose distributions that incorporate random set-up error". In: *Phys. Med. Biol.* 47.19, pp. 3465–3473.

Bedford, J. L., Fast, M. F., Nill, S., McDonald, F. M. A., Ahmed, M., Hansen, V. N., and Oelfke, U. (2015). "Effect of MLC tracking latency on conformal volumetric modulated arc therapy (VMAT) plans in 4D stereotactic lung treatment". In: *Radiother. Oncol.* 117.3, pp. 491–495.

Bender, E. T., Hardcastle, N., and Tomé, W. A. (2012). "On the dosimetric effect and reduction of inverse consistency and transitivity errors in deformable image registration for dose accumulation." In: *Med. Phys.* 39.1, pp. 272–80.

Bender, E. T. and Tomé, W. A. (2009). "The utilization of consistency metrics for error analysis in deformable image registration." In: *Phys. Med. Biol.* 54.18, pp. 5561–5577.

Berbeco, R. I., Mostafavi, H., Sharp, G. C., and Jiang, S. B. (2005). "Towards fluoroscopic respiratory gating for lung tumours without radiopaque markers." In: *Phys. Med. Biol.* 50.19, pp. 4481–4490.

Berbeco, R. I., Nishioka, S., Shirato, H., and Jiang, S. B. (2006). "Residual motion of lung tumors in end-of-inhale respiratory gated radiotherapy based on external surrogates." In: *Med. Phys.* 33.11, pp. 4149–4156.

Bjerre, T., Crijns, S. P. M., Rosenschöld, P. M. af, Aznar, M., Specht, L., Larsen, R., and Keall, P. (2013). "Three-dimensional MRI-linac intra-fraction guidance using multiple orthogonal cine-MRI planes". In: *Phys. Med. Biol.* 58.14, pp. 4943–4950.

Blaimer, M., Breuer, F., Mueller, M., Heidemann, R. M., Griswold, M. A., and Jakob, P. M. (2004). "SMASH, SENSE, PILS, GRAPPA: how to choose the optimal method." In: *Top. Magn. Reson. Imaging* 15.4, pp. 223–236.

Bol, G. H., Hissoiny, S., Lagendijk, J. J. W., and Raaymakers, B. W. (2012). "Fast online Monte Carlo-based IMRT planning for the MRI linear accelerator." In: *Phys. Med. Biol.* 57.5, pp. 1375–1385.

Bolme, D., Beveridge, J. R., Draper, B. A., and Lui, Y. M. (2010). "Visual object tracking using adaptive correlation filters". In: *IEEE Comput. Soc. Conf. Comput. Vis. Pattern Recognit.* Pp. 2544–2550. arXiv: 1404.7584.

Bondar, M. L., Hoogeman, M. S., Mens, J. W., Quint, S., Ahmad, R., Dhawtal, G., and Heijmen, B. J. (2012). "Individualized nonadaptive and online-adaptive intensity-modulated radiotherapy treatment strategies for cervical cancer patients based on pretreatment acquired variable bladder filling computed tomography scans". In: *Int. J. Radiat. Oncol. Biol. Phys.* 83.5, pp. 1617–1623.

Booth, J. T., Caillet, V., Hardcastle, N., O'Brien, R., Szymura, K., Crasta, C., Harris, B., Haddad, C., Eade, T., and Keall, P. J. (2016). "The first patient treatment of electromagnetic-guided real time adaptive radiotherapy using MLC tracking for lung SABR". In: *Radiother. Oncol.* 121.1, pp. 19–25.

Borman, P. T. S., Bos, C., Boorder, T. de, Raaymakers, B. W., Moonen, C. T. W., and Crijns, S. P. M. (2016). "Towards real-time thermometry using simultaneous multislice MRI". In: *Phys. Med. Biol.* 61.17, pp. 461–477.

Borst, G. R., Sonke, J.-J., Betgen, A., Remeijer, P., Herk, M. van, and Lebesque, J. V. (2007). "Kilo-Voltage Cone-Beam Computed Tomography Setup Measurements for Lung Cancer Patients; First Clinical Results and Comparison With Electronic Portal-Imaging Device". In: *Int. J. Radiat. Oncol.* 68.2, pp. 555–561.

Bortfeld, T., Jiang, S. B., and Rietzel, E. (2004). "Effects of motion on the total dose distribution." In: *Semin. Radiat. Oncol.* 14.1, pp. 41–51.

Bowman, A. W. and Azzalini, A. (1997). *Applied smoothing techniques for data analysis : the kernel approach with S-Plus illustrations*. Clarendon Press ; Oxford University Press.

Boye, D., Lomax, T., and Knopf, A. (2013). "Mapping motion from 4D-MRI to 3D-CT for use in 4D dose calculations: A technical feasibility study". In: *Med. Phys.* 40.6, p. 061702.

Bradski, G. (2000). "The opencv library". In: *Dr. Dobbs J.* 25.11, pp. 120–126.

Breuer, F. A., Blaimer, M., Heidemann, R. M., Mueller, M. F., Griswold, M. A., and Jakob, P. M. (2005). "Controlled aliasing in parallel imaging results in higher acceleration (CAIPIRINHA) for multi-slice imaging". In: *Magn. Reson. Med.* 53.3, pp. 684–691.

Brix, L., Ringgaard, S., Sørensen, T. S., and Poulsen, P. R. (2014). "Three-dimensional liver motion tracking using real-time two-dimensional MRI." In: *Med. Phys.* 41.4, p. 042302.

Bruhn, A., Weickert, J., and Schnörr, C. (2005). "Lucas/Kanade meets Horn/Schunck: Combining local and global optic flow methods". In: *Int. J. Comput. Vis.* 61.3, pp. 1–21. arXiv: 1035417.

Bussels, B., Goethals, L., Feron, M., Bielen, D., Dymarkowski, S., Suetens, P., and Haustermans, K. (2003). "Respiration-induced movement of the upper abdom-

inal organs: A pitfall for the three-dimensional conformal radiation treatment of pancreatic cancer". In: *Radiother. Oncol.* 68.1, pp. 69–74.

Celicanin, Z., Bieri, O., Preiswerk, F., Cattin, P., Scheffler, K., and Santini, F. (2015). "Simultaneous acquisition of image and navigator slices using CAIPIRINHA for 4D MRI". In: *Magn. Reson. Med.* 73.2, pp. 669–676.

Cerviño, L. I., Chao, A. K. Y., Sandhu, A., and Jiang, S. B. (2009). "The diaphragm as an anatomic surrogate for lung tumor motion." In: *Phys. Med. Biol.* 54.11, pp. 3529–41.

Chang, J., Cheung, P., Erler, D., Sonier, M., Korol, R., and Chu, W. (2016). "Stereotactic Ablative Body Radiotherapy for Primary Renal Cell Carcinoma in Non-surgical Candidates: Initial Clinical Experience". In: *Clin. Oncol.* 28.9, pp. 109–114.

Colvill, E., Booth, J. T., O'Brien, R. T., Eade, T. N., Kneebone, A. B., Poulsen, P. R., and Keall, P. J. (2015). "Multileaf Collimator Tracking Improves Dose Delivery for Prostate Cancer Radiation Therapy: Results of the First Clinical Trial". In: *Int. J. Radiat. Oncol.* 92.5, pp. 1141–1147.

Crijns, S. P. M., Raaymakers, B. W., and Lagendijk, J. J. W. (2012). "Proof of concept of MRI-guided tracked radiation delivery: tracking one-dimensional motion." In: *Phys. Med. Biol.* 57.23, pp. 7863–72.

Crijns, S. P. M., Kotte, A. N. T. J., Lagendijk, J. J. W., and Raaymakers, B. W. (2012). "Validation of real-time target tracking for MRI-guided interventions". In: *Proc. Int. Soc. Magn. Reson. Med.* P. 987.

Davies, G. A., Clowes, P., Bedford, J. L., Evans, P. M., Webb, S., and Poludniowski, G. (2013). "An experimental evaluation of the Agility MLC for motion-compensated VMAT delivery." In: *Phys. Med. Biol.* 58.13, pp. 4643–57.

De Meerleer, G., Khoo, V., Escudier, B., Joniau, S., Bossi, A., Ost, P., Briganti, A., Fonteyne, V., Van Vulpen, M., Lumen, N., Spahn, M., and Mareel, M. (2014). "Radiotherapy for renal-cell carcinoma". In: *Lancet Oncol.* 15.4.

Delaney, G., Jacob, S., Featherstone, C., and Barton, M. (2005). "The role of radiotherapy in cancer treatment: Estimating optimal utilization from a review of evidence-based clinical guidelines". In: *Cancer* 104.6, pp. 1129–1137.

Denis De Senneville, B., Mougenot, C., and Moonen, C. T. W. (2007). "Real-time adaptive methods for treatment of mobile organs by MRI-controlled high-intensity focused ultrasound". In: *Magn. Reson. Med.* 57.2, pp. 319–330.

Denis de Senneville, B., Ries, M., Bartels, L. W., and Moonen, C. T. W. (2012). "MRI-Guided High-Intensity Focused Ultrasound Sonication of Liver and Kidney". In: *Interv. Magn. Reson. Imaging*. Ed. by T. Kahn and H. Busse. Berlin, Heidelberg: Springer Berlin Heidelberg, pp. 349–366.

Depuydt, T., Verellen, D., Haas, O., Gevaert, T., Linthout, N., Duchateau, M., Tournel, K., Reynders, T., Leysen, K., Hoogeman, M., Storme, G., and Ridder, M. D. (2011). "Geometric accuracy of a novel gimbals based radiation therapy tumor tracking system". In: *Radiother. Oncol.* 98.3, pp. 365–372.

Dragonu, I., Denis De Senneville, B., Quesson, B., Moonen, C., and Ries, M. (2009). "Real-time geometric distortion correction for interventional imaging with Echo-planar imaging (EPI)". In: *Magn. Reson. Med.* 61.4, pp. 994–1000.

Elgammal, A., Duraiswami, R., Harwood, D., and Davis, L. (2001). "Background and Foreground Modeling Using Nonparametric Kernel Density Estimation for Visual Surveillance". In: *Proc. IEEE* 90.7, pp. 1151–1163.

Falk, M., Munck af Rosenschöld, P., Keall, P., Cattell, H., Cho, B. C., Poulsen, P., Povzner, S., Sawant, A., Zimmerman, J., and Korreman, S. (2010). "Real-time dynamic MLC tracking for inversely optimized arc radiotherapy". In: *Radiother. Oncol.* 94.2, pp. 218–223.

Falk, M., Larsson, T., Keall, P., Chul Cho, B., Aznar, M., Korreman, S., Poulsen, P., and Munck Af Rosenschold, P. (2012). "The dosimetric impact of inversely optimized arc radiotherapy plan modulation for real-time dynamic MLC tracking delivery." In: *Med. Phys.* 39.3, pp. 1588–94.

Fallone, B. G. (2014). "The Rotating Biplanar Linac-Magnetic Resonance Imaging System". In: *Semin. Radiat. Oncol.* 24.3, pp. 200–202.

Fast, M. F., Kamerling, C. P., Ziegenhein, P., Menten, M. J., Bedford, J. L., Nill, S., and Oelfke, U. (2016). "Assessment of MLC tracking performance during hypofractionated prostate radiotherapy using real-time dose reconstruction". In: *Phys. Med. Biol.* 61.4, pp. 1546–1562.

Fast, M. F., Nill, S., Bedford, J. L., and Oelfke, U. (2014). "Dynamic tumor tracking using the Elekta Agility MLC". In: *Med. Phys.* 41.11, pp. 1–5.

Feng, M., Balter, J. M., Normolle, D., Adusumilli, S., Cao, Y., Chenevert, T. L., and Ben-Josef, E. (2009). "Characterization of Pancreatic Tumor Motion Using Cine- MRI: Surrogates for Tumor Position Should be Used with Caution". In: *Int. J. Radiat. Oncol. Biol. Phys.* 74.3, pp. 884–891.

Fowler, J. F. (2005). "The radiobiology of prostate cancer including new aspects of fractionated radiotherapy". In: *Acta Oncol. (Madr).* 44.3, pp. 265–276.

Freislederer, P., Reiner, M., Hoischen, W., Quanz, A., Heinz, C., Walter, F., Belka, C., and Soehn, M. (2015). "Characteristics of gated treatment using an optical surface imaging and gating system on an Elekta linac". In: *Radiat Oncol* 10, p. 68.

Fuss, M., Salter, B. J., Cavanaugh, S. X., Fuss, C., Sadeghi, A., Fuller, C. D., Ameduri, A., Hevezi, J. M., Herman, T. S., and Thomas, C. R. (2004). "Daily ultrasound-based image-guided targeting for radiotherapy of upper abdominal malignancies". In: *Int. J. Radiat. Oncol. Biol. Phys.* 59.4, pp. 1245–1256.

Ghilezan, M. J., Jaffray, D. A., Siewerdsen, J. H., Van Herk, M., Shetty, A., Sharpe, M. B., Jafri, S. Z., Vicini, F. A., Matter, R. C., Brabbins, D. S., and Martinez, A. A. (2005). "Prostate gland motion assessed with cine-magnetic resonance imaging (cine-MRI)". In: *Int. J. Radiat. Oncol. Biol. Phys.* 62.2, pp. 406–417.

Gierga, D., Brewer, J., and Sharp, G. (2005). "The correlation between internal and external markers for abdominal tumors: implications for respiratory gating". In: *Int. J. ...* 61.5, pp. 1551–8.

Giraud, P. and Garcia, R. (2010). "Respiratory gating for radiotherapy: main technical aspects and clinical benefits". In: *Bull. Cancer* 97.Table 1, pp. 847–856.

Giraud, P., Yorke, E., Jiang, S., Simon, L., Rosenzweig, K., and Mageras, G. (2006). "Reduction of organ motion effects in IMRT and conformal 3D radiation delivery by using gating and tracking techniques." In: *Cancer Radiother.* 10.5, pp. 269–82.

Glitzner, M., Denis de Senneville, B., Lagendijk, J. J. W., Raaymakers, B. W., and Crijns, S. P. M. (2015a). "On-line 3D motion estimation using low resolution MRI." In: *Phys. Med. Biol.* 60.16, pp. 301–310.

Glitzner, M., Crijns, S. P. M., Denis de Senneville, B., Kontaxis, C., Prins, F. M., Lagendijk, J. J. W., and Raaymakers, B. W. (2015b). "On-line MR imaging for dose validation of abdominal radiotherapy". In: *Phys. Med. Biol.* 60.22, pp. 8869–8883.

Glitzner, M., Crijns, S. P. M., Denis De Senneville, B., Lagendijk, J. J. W., and Raaymakers, B. W. (2015c). "On the suitability of Elekta's Agility 160 MLC for tracked radiation delivery: closed-loop machine performance". In: *Phys. Med. Biol.* 60.5, pp. 2005–2017.

Glitzner, M., Fast, M. F., Denis de Senneville, B., Nill, S., Oelfke, U., Lagendijk, J. J. W., Raaymakers, B. W., and Crijns, S. P. M. (2017a). "Real-time auto-adaptive margin generation for MLC-tracked radiotherapy". In: *Phys. Med. Biol.* 62.1, pp. 186–201.

Glitzner, M., Woodhead, P. L., Lagendijk, J. J. W., and Raaymakers, B. W. (2017b). "Real-time performance of the Elekta MR-linac clinical prototype". In: *Proc. 59th AAPM.* Vol. 44.

Groh, B. A., Siewerdsen, J. H., Drake, D. G., Wong, J. W., and Jaffray, D. A. (2002). "A performance comparison of flat-panel imager-based MV and kV cone-beam CT." In: *Med. Phys.* 29.2002, pp. 967–975.

Haacke, E. M., Brown, R. W., Thompson, M. R., and Venkatesan, R. (1999). *Magnetic Resonance Imaging: Physical Principles and Sequence Design.* Wiley.

Heerkens, H. D., Van Vulpen, M., Van Den Berg, C. a. T., Tijssen, R. H. N., Crijns, S. P. M., Molenaar, I. Q., Van Santvoort, H. C., Reerink, O., and Meijer, G. J. (2014). "MRI-based tumor motion characterization and gating schemes for radiation therapy of pancreatic cancer". In: *Radiother. Oncol.* 111.2, pp. 252–257.

Heide, U. A. van der, Kotte, A. N. T. J., Dehnad, H., Hofman, P., Lagenijk, J. J. W., and Vulpen, M. van (2007). "Analysis of fiducial marker-based position verification in the external beam radiotherapy of patients with prostate cancer". In: *Radiother. Oncol.* 82.1, pp. 38–45.

Heijst, T. C. F. van, Philippens, M. E. P., Charaghvandi, R. K., Hartogh, M. D. den, Lagendijk, J. J. W., Desirée van den Bongard, H. J. G., and Asselen, B. van (2016). "Quantification of intra-fraction motion in breast radiotherapy using supine magnetic resonance imaging." In: *Phys. Med. Biol.* 61.3, pp. 1352–1370.

Heinrich, M. P., Jenkinson, M., Bhushan, M., Matin, T., Gleeson, F. V., Brady, S. M., and Schnabel, J. a. (2012). "MIND: Modality independent neighbourhood descriptor for multi-modal deformable registration". In: *Med. Image Anal.* 16.7, pp. 1423–1435.

Herman, M. G. (2005). "Clinical use of electronic portal imaging". In: *Semin. Radiat. Oncol.* 15.3, pp. 157–167.

Hissoiny, S., Raaijmakers, A. J. E., Ozell, B., Després, P., and Raaymakers, B. W. (2011a). *Fast dose calculation in magnetic fields with GPUMCD.* Tech. rep. 16, pp. 5119–5129.

Hissoiny, S., Ozell, B., Bouchard, H., and Després, P. (2011b). "GPUMCD: A new GPU-oriented Monte Carlo dose calculation platform." In: *Med. Phys.* 38.2, pp. 754–764. arXiv: 1101.1245.

Hoogeman, M., Prévost, J. B., Nuyttens, J., Pöll, J., Levendag, P., and Heijmen, B. (2009). "Clinical Accuracy of the Respiratory Tumor Tracking System of the CyberKnife: Assessment by Analysis of Log Files". In: *Int. J. Radiat. Oncol. Biol. Phys.* 74.1, pp. 297–303.

Hore, P. (1983). "Solvent suppression in fourier transform nuclear magnetic resonance". In: *J. Magn. Reson.* 55.2, pp. 283–300.

Horn, B. K. P. and Schunck, B. G. (1981). "Determining optical flow". In: *Artif. Intell.* 17.1-3, pp. 185–203.

Hynynen, K., Freund, W. R., Cline, H. E., Chung, A. H., Watkins, R. D., Vetro, J. P., and Jolesz, F. A. (1996). "A clinical, noninvasive, MR imaging monitored ultrasound surgery method". In: *Radiographics* 16.1, pp. 185–195.

ICRU 83, (2010). "Prescribing, Recording, and Reporting Photon-Beam Intensity-Modulated Radiation Therapy (IMRT)". In: *J. Int. Comm. Radiat. Units Meas.* 10.1.

Jaffray, D. A., Siewerdsen, J. H., Wong, J. W., and Martinez, A. A. (2002). "Flat-panel cone-beam computed tomography for image-guided radiation therapy". In: *Int. J. Radiat. Oncol. Biol. Phys.* 53.5, pp. 1337–1349.

Jaffray, D. A., Lindsay, P. E., Brock, K. K., Deasy, J. O., and Tomé, W. A. (2010). "Accurate Accumulation of Dose for Improved Understanding of Radiation Effects in Normal Tissue". In: *Int. J. Radiat. Oncol. Biol. Phys.* 76.3, pp. 135–139. arXiv: NIHMS150003.

Jaffray, D. A., Carlone, M. C., Milosevic, M. F., Breen, S. L., Stanescu, T., Rink, A., Alasti, H., Simeonov, A., Sweitzer, M. C., and Winter, J. D. (2014). "A Facility for Magnetic Resonance-Guided Radiation Therapy". In: *Semin. Radiat. Oncol.* 24.3, pp. 193–195.

Kamerling, C. P., Fast, M. F., Ziegenhein, P., Menten, M. J., Nill, S., and Oelfke, U. (2016). "Real-time 4D dose reconstruction for tracked dynamic MLC deliveries for lung SBRT". In: *Med. Phys.* 43.11, pp. 6072–6081.

Karlsson, M., Karlsson, M. G., Nyholm, T., Amies, C., and Zackrisson, B. (2009). "Dedicated Magnetic Resonance Imaging in the Radiotherapy Clinic". In: *Int. J. Radiat. Oncol. Biol. Phys.* 74.2, pp. 644–651.

Kashani, R., Tanderup, K., Victoria, J., Santanam, L., Wooten, H., Green, O., Dempsey, J., and Mutic, S. (2014). "Feasibility of Gating Using a Magnetic-Resonance Image Guided Radiation Therapy (MR-IGRT) System". In: *Int. J. Radiat. Oncol.* 90.1, S843–S844.

Keall, P. J., Barton, M., and Crozier, S. (2014). "The Australian Magnetic Resonance Imaging-Linac Program". In: *Semin. Radiat. Oncol.* 24.3, pp. 203–206.

Keall, P. J., Kini, V. R., Vedam, S. S., and Mohan, R. (2001). "Motion adaptive x-ray therapy: a feasibility study." In: *Phys. Med. Biol.* 46.1, pp. 1–10.

Keall, P. J., Cattell, H., Pokhrel, D., Dieterich, S., Wong, K. H., Murphy, M. J., Vedam, S. S., Wijesooriya, K., and Mohan, R. (2006a). "Geometric accuracy of a real-time target tracking system with dynamic multileaf collimator tracking system". In: *Int. J. Radiat. Oncol. Biol. Phys.* 65.5, pp. 1579–1584.

Keall, P. J., Vedam, S., George, R., Bartee, C., Siebers, J., Lerma, F., Weiss, E., and Chung, T. (2006b). "The clinical implementation of respiratory-gated intensity-modulated radiotherapy". In: *Med. Dosim.* 31.2, pp. 152–162.

Keall, P. J., Mageras, G. S., Balter, J. M., Emery, R. S., Forster, K. M., Jiang, S. B., Kapatoes, J. M., Low, D. a., Murphy, M. J., Murray, B. R., Ramsey, C. R., Van Herk, M. B., Vedam, S. S., Wong, J. W., and Yorke, E. (2006c). "The management of respiratory motion in radiation oncology report of AAPM Task Group 76." In: *Med. Phys.* 33.10, pp. 3874–3900.

Keall, P. J., Colvill, E., O'Brien, R., Ng, J. A., Poulsen, P. R., Eade, T., Kneebone, A., and Booth, J. T. (2014). "The first clinical implementation of electromagnetic transponder-guided MLC tracking." In: *Med. Phys.* 41.2, p. 020702.

Kerkhof, E. M., Balter, J. M., Vineberg, K., and Raaymakers, B. W. (2010). "Treatment plan adaptation for MRI-guided radiotherapy using solely MRI data: a CT-based simulation study." In: *Phys. Med. Biol.* 55.16, N433–N440.

King, A. P., Buerger, C., Tsoumpas, C., Marsden, P. K., and Schaeffter, T. (2012). "Thoracic respiratory motion estimation from MRI using a statistical model and a 2-D image navigator". In: *Med. Image Anal.* 16.1, pp. 252–264.

Kleijnen, J.-p. J. E., Asselen, B. van, Burbach, J. P. M., Intven, M., Philippens, M. E. P., Reerink, O., Lagendijk, J. J. W., and Raaymakers, B. W. (2016). "Evolution of motion uncertainty in rectal cancer: implications for adaptive radiotherapy". In: *Phys. Med. Biol.* 61.1, pp. 1–11.

Kontaxis, C., Bol, G. H., Lagendijk, J. J. W., and Raaymakers, B. W. (2015a). "A new methodology for inter- and intrafraction plan adaptation for the MR-linac". In: *Phys. Med. Biol.* 60.19, pp. 7485–7497.

— (2015b). "Towards adaptive IMRT sequencing for the MR-linac". In: *Phys. Med. Biol.* 60.6, pp. 2493–2509.

Koolwal, K. (2009). "Investigating latency effects of the Linux real-time Preemption Patches (PREEMPT RT) on AMD's GEODE LX Platform". In: *RTLWS11*.

Korin, H. W., Ehman, R. L., Riederer, S. J., Felmlee, J. P., and Grimm, R. C. (1992). "Respiratory kinematics of the upper abdominal organs: A quantitative study". In: *Magn. Reson. Med.* 23.1, pp. 172–178.

Kotte, A. N. T. J., Hofman, P., Lagendijk, J. J. W., Vulpen, M. van, and Heide, U. A. van der (2007). "Intrafraction Motion of the Prostate During External-Beam Radiation Therapy: Analysis of 427 Patients with Implanted Fiducial Markers". In: *Int. J. Radiat. Oncol. Biol. Phys.* 69.2, pp. 419–425.

Krauss, A., Nill, S., and Oelfke, U. (2011). "The comparative performance of four respiratory motion predictors for real-time tumour tracking." In: *Phys. Med. Biol.* 56.16, pp. 5303–5317.

Kupelian, P. and Sonke, J. J. (2014). "Magnetic Resonance-Guided Adaptive Radiotherapy: A Solution to the Future". In: *Semin. Radiat. Oncol.* 24.3, pp. 227–232.

Lagendijk, J. J. W. and Bakker, C. J. G. (2000). "MRI guided radiotherapy: a MRI based linear accelerator". In: *Radiother. Oncol* 56.S1, pp. 60–61.

Lagendijk, J. J. W., Raaymakers, B. W., Van Der Heide, U. A., Topolnjak, R., Dehnad, H., Hofman, P., Nederveen, A. J., Schulz, I. M., Welleweerd, J., and

Bakker, C. J. G. (2002). "MRI guided radiotherapy: MRI as position verification system for IMRT". In: *Radiother. Oncol* 64.S1, S75–S76.

Lagendijk, J. J. W., Raaymakers, B. W., and Vulpen, M. van (2014). "The Magnetic Resonance Imaging-Linac System". In: *Semin. Radiat. Oncol.* 24.3, pp. 207–209.

Langen, K. M. and Jones, D. T. L. (2001). "Organ motion and its management". In: *Int. J. Radiat. Oncol. Biol. Phys.* 50.1, pp. 265–278.

Larkman, D. J., Hajnal, J. V., Herlihy, A. H., Coutts, G. A., Young, I. R., and Ehnholm, G. (2001). "Use of multicoil arrays for separation of signal from multiple slices simultaneously excited". In: *J. Magn. Reson. Imaging* 13.2, pp. 313–317.

Lattanzi, J., McNeeley, S., Pinover, W., Horwitz, E., Das, I., Schultheiss, T. E., and Hanks, G. E. (1999). "A comparison of daily CT localization to a daily ultrasound-based system in prostate cancer". In: *Int. J. Radiat. Oncol. Biol. Phys.* 43.4, pp. 719–725.

Lin, M.-H., Li, J., Wang, L., Koren, S., Fan, J., Forkal, E., and Ma, C.-M. (2012). "4D patient dose reconstruction using online measured EPID cine images for lung SBRT treatment validation". In: *Med. Phys.* 39.10, p. 5949.

Litzenberg, D., Dawson, L. A., Sandler, H., Sanda, M. G., McShan, D. L., Ten Haken, R. K., Lam, K. L., Brock, K. K., and Balter, J. M. (2002). "Daily prostate targeting using implanted radiopaque markers". In: *Int. J. Radiat. Oncol. Biol. Phys.* 52.3, pp. 699–703.

Low, D. A., Zhu, X. R., Harms, W. B., and Purdy, J. a. (1995). "Measurement of a photon penumbra-generating kernel for a convolution-adapted ratio-TAR algorithm for 3D treatment planning." In: *Med. Phys.* 22.9, pp. 1395–403.

Low, D. A., Harms, W. B., Mutic, S., and Purdy, J. a. (1998). "A technique for the quantitative evaluation of dose distributions." In: *Med. Phys.* 25.5, pp. 656–61.

Luo, W., Li, J., Price, R. a., Chen, L., Yang, J., Fan, J., Chen, Z., McNeeley, S., Xu, X., and Ma, C.-M. (2006). "Monte Carlo based IMRT dose verification using MLC log files and R/V outputs." In: *Med. Phys.* 33.7, pp. 2557–2564.

Lustig, M., Donoho, D., and Pauly, J. M. (2007). "Sparse MRI: The application of compressed sensing for rapid MR imaging". In: *Magn. Reson. Med.* 58.6, pp. 1182–1195.

Macías, V. and Biete, A. (2009). "Hypofractionated radiotherapy for localised prostate cancer. Review of clinical trials". In: *Clin. Transl. Oncol.* 11.7, pp. 437–445.

McBain, C. A., Henry, A. M., Sykes, J., Amer, A., Marchant, T., Moore, C. M., Davies, J., Stratford, J., McCarthy, C., Porritt, B., Williams, P., Khoo, V. S., and Price, P. (2006). "X-ray volumetric imaging in image-guided radiotherapy: The new standard in on-treatment imaging". In: *Int. J. Radiat. Oncol. Biol. Phys.* 64.2, pp. 625–634.

McCammon, R., Schefter, T. E., Gaspar, L. E., Zaemisch, R., Gravdahl, D., and Kavanagh, B. (2009). "Observation of a Dose-Control Relationship for Lung and Liver Tumors After Stereotactic Body Radiation Therapy". In: *Int. J. Radiat. Oncol. Biol. Phys.* 73.1, pp. 112–118.

McGahan, J. P., Ryu, J., and Fogata, M. (2004). "Ultrasound probe pressure as a source of error in prostate localization for external beam radiotherapy". In: *Int. J. Radiat. Oncol. Biol. Phys.* 60.3, pp. 788–793.

Menten, M. J., Fast, M. F., Nill, S., Kamerling, C. P., McDonald, F., and Oelfke, U. (2016). "Lung stereotactic body radiotherapy with an MR-linac - Quantifying the impact of the magnetic field and real-time tumor tracking." In: *Radiother. Oncol.* 119.3, pp. 461–6.

Metcalfe, P., Kron, T., Elliot, A., Wong, T., and Hoban, P. (1993). "Dosimetry of 6-MV x-ray beam penumbra". In: *Med. Phys.* 20.5, pp. 1439–45.

Moerland, M., Bergh, A. van den, Bhagwandien, R., Janssen, W., Bakker, C., Lagendijk, J., and Battermann, J. (1994). "The influence of respiration induced motion of the kidneys on the accuracy of radiotherapy treatment planing, a magnetic resonance imaging study". In: *Radiother. Oncol.* 30, pp. 150–154.

Moore, D., Ruan, D., and Sawant, A. (2016). "Fast leaf-fitting with generalized underdose/overdose constraints for real-time MLC tracking". In: *Med. Phys.* 43.1, pp. 465–474.

Mutic, S. and Dempsey, J. F. (2014). "The ViewRay System: Magnetic Resonance-Guided and Controlled Radiotherapy". In: *Semin. Radiat. Oncol.* 24.3, pp. 196–199.

Nederveen, A., Lagendijk, J., and Hofman, P. (2000). "Detection of fiducial gold markers for automatic on-line megavoltage position verification using a marker extraction kernel (MEK)". In: *Int. J. Radiat. Oncol. Biol. Phys.* 47.5, pp. 1435–1442.

Ohara, K., Okumura, T., Akisada, M., Inada, T., Mori, T., Yokota, H., and Calaguas, M. J. B. (1989). "Irradiation synchronized with respiration gate". In: *Int. J. Radiat. Oncol.* 17.4, pp. 853–857.

Oliveira, F. P. and Tavares, J. M. R. (2014). "Medical image registration: a review". In: *Comput. Methods Biomech. Biomed. Engin.* 17.2, pp. 73–93.

Onishi, H., Shirato, H., Nagata, Y., Hiraoka, M., Fujino, M., Gomi, K., Karasawa, K., Hayakawa, K., Niibe, Y., Takai, Y., Kimura, T., Takeda, A., Ouchi, A., Hareyama, M., Kokubo, M., Kozuka, T., Arimoto, T., Hara, R., Itami, J., and Araki, T. (2011). "Stereotactic body radiotherapy (SBRT) for operable Stage i non-small-cell lung cancer: Can SBRT be comparable to surgery?" In: *Int. J. Radiat. Oncol. Biol. Phys.* 81.5, pp. 1352–1358.

Østergaard Noe, K., De Senneville, B. D., Elstrøm, U. V., Tanderup, K., and Sørensen, T. S. (2008). "Acceleration and validation of optical flow based deformable registration for image-guided radiotherapy." In: *Acta Oncol.* 47.7, pp. 1286–1293.

Overweg, J., Raaymakers, B. W., Lagendijk, J. J. W., and Brown, K. (2009). "System for MRI guided radiotherapy". In: *Proc. Int. Soc. Mag. Reson. Med.* Vol. 17, p. 594.

Paganelli, C., Peroni, M., Riboldi, M., Sharp, G. C., Ciardo, D., Alterio, D., Orecchia, R., and Baroni, G. (2013). "Scale invariant feature transform in adaptive radiation therapy: a tool for deformable image registration assessment and re-planning indication." In: *Phys. Med. Biol.* 58, pp. 287–99.

Plathow, C., Ley, S., Fink, C., Puderbach, M., Hosch, W., Schmähl, A., Debus, J., and Kauczor, H. U. (2004). "Analysis of intrathoracic tumor mobility during

whole breathing cycle by dynamic MRI". In: *Int. J. Radiat. Oncol. Biol. Phys.* 59.4, pp. 952–959.

Plathow, C., Schoebinger, M., Fink, C., Ley, S., Puderbach, M., Eichinger, M., Bock, M., Meinzer, H.-P., and Kauczor, H.-U. (2005). "Evaluation of lung volumetry using dynamic three-dimensional magnetic resonance imaging." In: *Invest. Radiol.* 40.3, pp. 173–9.

Plathow, C., Hof, H., Kuhn, S., Puderbach, M., Ley, S., Biederer, J., Claussen, C. D., Huber, P. E., Schaefer, J., Tuengerthal, S., and Kauczor, H. U. (2006). "Therapy monitoring using dynamic MRI: Analysis of lung motion and intrathoracic tumor mobility before and after radiotherapy". In: *Eur. Radiol.* 16.9, pp. 1942–1950.

Poels, K., Verellen, D., Van de Vondel, I., El Mazghari, R., Depuydt, T., and De Ridder, M. (2014). "Fiducial marker and marker-less soft-tissue detection using fast MV fluoroscopy on a new generation EPID: investigating the influence of pulsing artifacts and artifact suppression techniques." In: *Med. Phys.* 41.10, p. 101911.

Poulsen, P. R., Cho, B., Sawant, A., Ruan, D., and Keall, P. J. (2010). "Detailed analysis of latencies in image-based dynamic MLC tracking." In: *Med. Phys.* 37.9, pp. 4998–5005.

Poulsen, P. R., Schmidt, M. L., Keall, P., Worm, E. S., Fledelius, W., and Hoffmann, L. (2012). "A method of dose reconstruction for moving targets compatible with dynamic treatments." In: *Med. Phys.* 39.10, pp. 6237–46.

Pruessmann, K. P., Weiger, M., Scheidegger, M. B., and Boesiger, P. (1999). "SENSE : Sensitivity Encoding for Fast MRI". In: 962, pp. 952–962.

Purdy, J. A. (1992). "Photon dose calculations for three-dimensional radiation treatment planning". In: *Semin. Radiat. Oncol.* 2.4, pp. 235–245.

Raaijmakers, A. J. E., Raaymakers, B. W., and Lagendijk, J. J. W. (2005). "Integrating a MRI scanner with a 6 MV radiotherapy accelerator: dose increase at tissue-air interfaces in a lateral magnetic field due to returning electrons." In: *Phys. Med. Biol.* 50.7, pp. 1363–76.

Raaymakers, B. W., Raaijmakers, A. J. E., Kotte, A. N. T. J., Jette, D., and Lagendijk, J. J. W. (2004). "Integrating a MRI scanner with a 6 MV radiotherapy accelerator: dose deposition in a transverse magnetic field". In: *Phys. Med. Biol.* 49.17, p. 4109.

Raaymakers, B. W., Lagendijk, J. J. W., Overweg, J., Kok, J. G. M., Raaijmakers, a. J. E., Kerkhof, E. M., Put, R. W. van der, Meijsing, I., Crijns, S. P. M., Benedosso, F., Vulpen, M. van, Graaff, C. H. W. de, Allen, J., and Brown, K. J. (2009). "Integrating a 1.5 T MRI scanner with a 6 MV accelerator: proof of concept." In: *Phys. Med. Biol.* 54.12, pp. 229–237.

Ravkilde, T., Keall, P. J., Grau, C., Høyer, M., and Poulsen, P. R. (2014). "Fast motion-including dose error reconstruction for VMAT with and without MLC tracking". In: *Phys. Med. Biol.* 59.23, p. 7279.

Richard, C. A., Borchers, B., and Clifford, H. T. (2013). *Parameter Estimation and Inverse Problems*. International Geophysics. Elsevier Science, p. 359.

Ries, M., Denis de Senneville, B., Roujol, S., Berber, Y., Quesson, B., and Moonen, C. (2010). "Real-time 3D target tracking in MRI guided focused ultrasound ablations in moving tissues." In: *Magn. Reson. Med.* 64.6, pp. 1704–12.

Roujol, S., Ries, M., Quesson, B., Moonen, C., and Denis De Senneville, B. (2010). "Real-time MR-thermometry and dosimetry for interventional guidance on abdominal organs". In: *Magn. Reson. Med.* 63.4, pp. 1080–1087.

Roujol, S., Ries, M., Moonen, C., and Denis De Senneville, B. (2011). "Automatic nonrigid calibration of image registration for real time MR-guided HIFU ablations of mobile organs". In: *IEEE Trans. Med. Imaging* 30.10, pp. 1737–1745.

Ruan, D. (2010). "Kernel density estimation-based real-time prediction for respiratory motion." In: *Phys. Med. Biol.* 55.5, pp. 1311–26.

Ruan, D., Kupelian, P., and Low, D. a. (2011). "Image-guided positioning and tracking." In: *Cancer J.* 17.3, pp. 155–8.

Santanam, L., Kashani, R., Green, O., Noel, C., Senadheera, L., Patel, V., Victoria, J., Tanderup, K., and Mutic, S. (2014). "Gating Latency of Soft Tissue Tracking Beam Control for an Onboard MR-IGRT System". In: *Int. J. Radiat. Oncol.* 90.1, p. 199.

Santanam, L., Noel, C., Wan, H., Kashani, R., Rankine, L. J., Mazur, T. R., Goddu, S. M., Wooten, H., Yaddanapudi, S., Green, O. L., Parikh, P. J., Mutic, S., and Olsen, J. R. (2015). "Adequacy of Gating Margins for Abdominal Tumors of Patients Treated With Real-Time MR Guided Radiation Therapy". In: *Int. J. Radiat. Oncol. Biol. Phys.* 93.3, S216–S217.

Santelli, C., Nezafat, R., Goddu, B., Manning, W. J., Smink, J., Kozerke, S., and Peters, D. C. (2011). "Respiratory bellows revisited for motion compensation: preliminary experience for cardiovascular MR." In: *Magn. Reson. Med.* 65.4, pp. 1097–1102.

Sawant, A., Venkat, R., Srivastava, V., Carlson, D., Povzner, S., Cattell, H., and Keall, P. (2008). "Management of three-dimensional intrafraction motion through real-time DMLC tracking". In: *Med. Phys.* 35.5, pp. 2050–61.

Sawant, A., Smith, R. L., Venkat, R. B., Santanam, L., Cho, B., Poulsen, P., Cattell, H., Newell, L. J., Parikh, P., and Keall, P. J. (2009). "Toward submillimeter accuracy in the management of intrafraction motion: the integration of real-time internal position monitoring and multileaf collimator target tracking." In: *Int. J. Radiat. Oncol. Biol. Phys.* 74.2, pp. 575–82.

Sawant, A., Dieterich, S., Svatos, M., and Keall, P. (2010). "Failure mode and effect analysis-based quality assurance for dynamic MLC tracking systems." In: *Med. Phys.* 37.2010, pp. 6466–6479.

Sawant, A., Keall, P., Pauly, K. B., Alley, M., Vasanawala, S., Loo, B. W., Hinkle, J., and Joshi, S. (2014). "Investigating the feasibility of rapid MRI for image-guided motion management in lung cancer radiotherapy." In: *Biomed Res. Int.* 2014, p. 485067.

Scarbrough, T. J., Golden, N. M., Ting, J. Y., Fuller, C. D., Wong, A., Kupelian, P. A., and Thomas, C. R. (2006). "Comparison of ultrasound and implanted seed marker prostate localization methods: Implications for image-guided radiotherapy". In: *Int. J. Radiat. Oncol. Biol. Phys.* 65.2, pp. 378–387.

Schellen, J., Dernehl, C., and Kowalewski, S. (2013). "Optimizing Image Processing on OMAP3 with driver-level frame buffering and color space conversion". In: *Proceedings of International Micro Air Vehicle Conference and Flight Competition 2014*, pp. 17–20.

Schreiner, L. J. (2004). "Review of Fricke gel dosimeters". In: *J. Phys. Conf. Ser.* 3, pp. 9–21.

Schultheiss, T. E., Tome, W. a., and Orton, C. G. (2012). "It is not appropriate to deform dose along with deformable image registration in adaptive radiotherapy". In: *Med. Phys.* 39.11, p. 6531.

Schwartz, L. H., Richaud, J., Buffat, L., Touboul, E., and Schlienger, M. (1994). "Kidney mobility during respiration." In: *Radiother. Oncol.* 32.1, pp. 84–86.

Seregni, M., Paganelli, C., Fattori, G., Summers, P., Bellomi, M., Baroni, G., and Riboldi, M. (2006). "Automated analysis of liver motion variability based on cine-MRI". In: *ISBI 2015*, p. 4.

Shah, A. P., Kupelian, P. A., Waghorn, B. J., Willoughby, T. R., Rineer, J. M., Mañon, R. R., Vollenweider, M. A., and Meeks, S. L. (2013). "Real-time tumor tracking in the lung using an electromagnetic tracking system". In: *Int. J. Radiat. Oncol. Biol. Phys.* 86.3, pp. 477–483.

Shimizu, S., Shirato, H., Kitamura, K., Shinohara, N., Harabayashi, T., Tsukamoto, T., Koyanagi, T., and Miyasaka, K. (2000). "Use of an implanted marker and real-time tracking of the marker for the positioning of prostate and bladder cancers". In: *Int. J. Radiat. Oncol. Biol. Phys.* 48.5, pp. 1591–1597.

Shirato, H., Shimizu, S., Kunieda, T., Kitamura, K., Van Herk, M., Kagei, K., Nishioka, T., Hashimoto, S., Fujita, K., Aoyama, H., Tsuchiya, K., Kudo, K., and Miyasaka, K. (2000). "Physical aspects of a real-time tumor-tracking system for gated radiotherapy". In: *Int. J. Radiat. Oncol. Biol. Phys.* 48.4, pp. 1187–1195.

Shirato, H., Seppenwoolde, Y., Kitamura, K., Onimura, R., and Shimizu, S. (2004). "Intrafractional Tumor Motion: Lung and Liver". In: *Semin. Radiat. Oncol.* 14.1, pp. 10–18.

Siebenthal, M. von, Székely, G., Gamper, U., Boesiger, P., Lomax, A., and Cattin, P. (2007a). "4D MR imaging of respiratory organ motion and its variability." In: *Phys. Med. Biol.* 52.6, pp. 1547–64.

Siebenthal, M. von, Székely, G., Lomax, A. J., and Cattin, P. C. (2007b). "Systematic errors in respiratory gating due to intrafraction deformations of the liver." In: *Med. Phys.* 34.9, pp. 3620–3629.

Smith, R. L., Sawant, A., Santanam, L., Venkat, R. B., Newell, L. J., Cho, B.-C., Poulsen, P., Catell, H., Keall, P. J., and Parikh, P. J. (2009). "Integration of real-time internal electromagnetic position monitoring coupled with dynamic multileaf collimator tracking: an intensity-modulated radiation therapy feasibility study." In: *Int. J. Radiat. Oncol. Biol. Phys.* 74.3, pp. 868–75.

Sotiras, A., Davatzikos, C., and Paragios, N. (2013). "Deformable medical image registration: A survey". In: *IEEE Trans. Med. Imaging* 32.7, pp. 1153–1190. arXiv: NIHMS150003.

Stam, M. K., Crijns, S. P. M., Zonnenberg, B. A., Barendrecht, M. M., Vulpen, M. van, Lagendijk, J. J. W., and Raaymakers, B. W. (2012). "Navigators for motion detection during real-time MRI-guided radiotherapy." In: *Phys. Med. Biol.* 57.21, pp. 6797–805.

Stam, M. K., Vulpen, M. van, Barendrecht, M. M., Zonnenberg, B. a., Crijns, S. P. M., Lagendijk, J. J. W., and Raaymakers, B. W. (2013). "Dosimetric

feasibility of MRI-guided external beam radiotherapy of the kidney." In: *Phys. Med. Biol.* 58.14, pp. 4933–41.

Stemkens, B., Glitzner, M., Kontaxis, C., Denis de Senneville, B., Prins, F., Crijns, S. P. M., Kerkmeijer, L., Lagendijk, J. J. W., Berg, C. A. T. van den, and Tijssen, R. H. N. (2016a). "The effects of inter-cycle respiratory motion variation on dose accumulation in single fraction MR-guided SBRT treatment of renal cell carcinoma". In: *Proc. 58th AAPM.* Vol. 43. 6, p. 3344.

Stemkens, B., Tijssen, R. H. N., Denis De Senneville, B., Lagendijk, J. J. W., and Berg, C. A. T. van den (2016b). "Image-driven, model-based 3D abdominal motion estimation for MR-guided radiotherapy." In: *Phys. Med. Biol.* 61.14, pp. 5335–55.

Tacke, M. B., Nill, S., Krauss, A., and Oelfke, U. (2010). "Real-time tumor tracking: Automatic compensation of target motion using the Siemens 160 MLC". In: *Med. Phys.* 37.2, p. 753.

Uematsu, M., Fukui, T., Shioda, A., Tokumitsu, H., Takai, K., Kojima, T., Asai, Y., and Kusano, S. (1996). "A dual computed tomography linear accelerator unit for stereotactic radiation therapy: A new approach without cranially fixated stereotactic frames". In: *Int. J. Radiat. Oncol. Biol. Phys.* 35.3, pp. 587–592.

Van Herk, M., Remeijer, P., Rasch, C., and Lebesque, J. V. (2000). "The probability of correct target dosage: Dose-population histograms for deriving treatment margins in radiotherapy". In: *Int. J. Radiat. Oncol. Biol. Phys.* 47.4, pp. 1121–1135.

Verellen, D., De Ridder, M., Linthout, N., Tournel, K., Soete, G., and G, S. (2007). "Innovations in image-guided radiotherapy". In: *Nat Rev Cancer* 7.12, pp. 949–960.

Wang, Y., Rossman, P. J., Grimm, R. C., Riederer, S. J., and Ehman, R. L. (1996). "Navigator-echo-based real-time respiratory gating and triggering for reduction of respiration effects in three-dimensional coronary MR angiography." In: *Radiology* 198.1, pp. 55–60.

Wendling, M., Louwe, R. J. W., McDermott, L. N., Sonke, J.-J., Herk, M. van, and Mijnheer, B. J. (2006). "Accurate two-dimensional IMRT verification using a back-projection EPID dosimetry method." In: *Med. Phys.* 33.2, pp. 259–273.

Willoughby, T. R., Kupelian, P. A., Pouliot, J., Shinohara, K., Aubin, M., Roach, M., Skrumeda, L. L., Balter, J. M., Litzenberg, D. W., Hadley, S. W., Wei, J. T., and Sandler, H. M. (2006). "Target localization and real-time tracking using the Calypso 4D localization system in patients with localized prostate cancer". In: *Int. J. Radiat. Oncol. Biol. Phys.* 65.2, pp. 528–534.

Wisotzky, E., O'Brien, R., and Keall, P. J. (2016). "Technical Note: A novel leaf sequencing optimization algorithm which considers previous underdose and overdose events for MLC tracking radiotherapy". In: *Med. Phys.* 43.1, pp. 132–136.

Wolff, D., Stieler, F., Welzel, G., Lorenz, F., Abo-Madyan, Y., Mai, S., Herskind, C., Polednik, M., Steil, V., Wenz, F., and Lohr, F. (2009). "Volumetric modulated arc therapy (VMAT) vs. serial tomotherapy, step-and-shoot IMRT and 3D-conformal RT for treatment of prostate cancer". In: *Radiother. Oncol.* 93.2, pp. 226–233.

Wolthaus, J. W. H., Sonke, J. J., Herk, M. van, and Damen, E. M. F. (2008). "Reconstruction of a time-averaged midposition CT scan for radiotherapy planning of lung cancer patients using deformable registration." In: *Med Phys* 35.9, pp. 3998–4011.

Wolthaus, J. W. H., Schneider, C., Sonke, J. J., Herk, M. van, Belderbos, J. S. a., Rossi, M. M. G., Lebesque, J. V., and Damen, E. M. F. (2006). "Mid-ventilation CT scan construction from four-dimensional respiration-correlated CT scans for radiotherapy planning of lung cancer patients". In: *Int. J. Radiat. Oncol. Biol. Phys.* 65.5, pp. 1560–1571.

Wu, Q., Chi, Y., Chen, P. Y., Krauss, D. J., Yan, D., and Martinez, A. (2009). "Adaptive Replanning Strategies Accounting for Shrinkage in Head and Neck IMRT". In: *Int. J. Radiat. Oncol. Biol. Phys.* 75.3, pp. 924–932.

Wysocka, B., Kassam, Z., Lockwood, G., Brierley, J., Dawson, L. A., Buckley, C. A., Jaffray, D., Cummings, B., Kim, J., Wong, R., and Ringash, J. (2010). "Interfraction and Respiratory Organ Motion During Conformal Radiotherapy in Gastric Cancer". In: *Int. J. Radiat. Oncol. Biol. Phys.* 77.1, pp. 53–59.

Yang, D., Li, H., Low, D. a., Deasy, J. O., and El Naqa, I. (2008). "A fast inverse consistent deformable image registration method based on symmetric optical flow computation." In: *Phys. Med. Biol.* 53.21, pp. 6143–6165.

Yeo, U. J., Taylor, M. L., Supple, J. R., Smith, R. L., Kron, T., and Franich, R. D. (2013). "Deformable gel dosimetry I: application to external beam radiotherapy and brachytherapy". In: *J. Phys. Conf. Ser.* 444.1, p. 012107.

Yun, J., Wachowicz, K., Mackenzie, M., Rathee, S., Robinson, D., and Fallone, B. G. (2013). "First demonstration of intrafractional tumor-tracked irradiation using 2D phantom MR images on a prototype linac-MR." In: *Med. Phys.* 40.5, p. 051718.

Zachiu, C., Denis de Senneville, B., Moonen, C., and Ries, M. (2015). "A framework for the correction of slow physiological drifts during MR-guided HIFU therapies: Proof of concept". In: *Med. Phys.* 42.7, pp. 4137–4148.

Zhang, S., Block, K. T., and Frahm, J. (2010). "Magnetic resonance imaging in real time: Advances using radial FLASH". In: *J. Magn. Reson. Imaging* 31.1, pp. 101–109.

Ziegenhein, P., Kamerling, C. P., Bangert, M., Kunkel, J., and Oelfke, U. (2013). "Performance-optimized clinical IMRT planning on modern CPUs." In: *Phys. Med. Biol.* 58.11, pp. 3705–15.

Publications

Journal articles

Glitzner, M., Denis de Senneville, B., Lagendijk, J. J. W., Raaymakers, B. W., and Crijns, S. P. M. (2015a). "On-line 3D motion estimation using low resolution MRI." In: *Phys. Med. Biol.* 60.16, pp. 301–310.

Glitzner, M., Crijns, S. P. M., Denis de Senneville, B., Kontaxis, C., Prins, F. M., Lagendijk, J. J. W., and Raaymakers, B. W. (2015b). "On-line MR imaging for dose validation of abdominal radiotherapy". In: *Phys. Med. Biol.* 60.22, pp. 8869–8883.

Glitzner, M., Crijns, S. P. M., Denis De Senneville, B., Lagendijk, J. J. W., and Raaymakers, B. W. (2015c). "On the suitability of Elekta's Agility 160 MLC for tracked radiation delivery: closed-loop machine performance". In: *Phys. Med. Biol.* 60.5, pp. 2005–2017.

Glitzner, M., Fast, M. F., Denis de Senneville, B., Nill, S., Oelfke, U., Lagendijk, J. J. W., Raaymakers, B. W., and Crijns, S. P. M. (2017). "Real-time auto-adaptive margin generation for MLC-tracked radiotherapy". In: *Phys. Med. Biol.* 62.1, pp. 186–201.

Kontaxis, C., Bol, G. H., Stemkens, B., Glitzner, M., Prins, F. M., Kerkmeijer, L. G. W., Lagendijk, J. J. W., and Raaymakers, B. W. (2017). "Towards fast online intrafraction replanning for free-breathing stereotactic body radiation therapy with the MR-linac". In: *Phys. Med. Biol.* submitted.

Stemkens, B., Glitzner, M., Kontaxis, C., Denis de Senneville, B., Prins, F. M., Crijns, S. P., Kerkmeijer, Linda G.W. , Lagendijk, J. J., Berg, C. A. van den, and Tijssen, R. H. (2017). "Effect of intra-fraction motion on the accumulated dose for free-breathing MR-guided stereotactic body radiation therapy of renal-cell carcinoma". In: *Phys. Med. Biol.* submitted.

Selected oral presentations

Glitzner, M., Crijns, S. P. M., Lagendijk, J. J. W., and Raaymakers, B. W. (2014). "Assessing Elekta MLC Tracking Performance". In: *Proc. 56th AAPM.* Vol. 41. 6, p. 119.

Glitzner, M., Fast, M., Senneville, B. de, Nill, S., Oelfke, U., Lagendijk, J., Raaymakers, B., and Crijns, S. (2016a). "Auto-Adaptive Margin Generation for MLC-Tracked Radiotherapy". In: *Proc. 58th AAPM.* Vol. 43. 6, p. 3857.

Glitzner, M., Fast, M. F., Denis de Senneville, B., Nill, S., Oelfke, U., Lagendijk, J. J. W., Raaymakers, B. W., and Crijns, S. P. M. (2016b). "On-line machine error compensation for MLC tracking". In: *Proc. XVIIIth ICCR*.

Glitzner, M., Raaymakers, B. W., Lagendijk, J. J. W., and Denis De Senneville, B. (2017a). "Multi-channel deformable image registration based on MRI tissue classes". In: *5th MR in RT Symposium*.

Glitzner, M. (2016). "Dose reconstruction and tracking margins for MRI-guided radiotherapy". In: *DKFZ Heidelberg Physikseminar*.

Glitzner, M., Woodhead, P. L., Lagendijk, J. J. W., and Raaymakers, B. W. (2017b). "Real-time performance of the Elekta MR-linac clinical prototype". In: *Proc. 59th AAPM*. Vol. 44.

Miscellaneous conference proceedings

Crijns, S. P. M., Glitzner, M., Denis de Senneville, B., Kontaxis, C., Maenhout, M., Bol, G., Lagendijk, J. J. W., and Raaymakers, B. W. (2015). "Fast Volumetric MRI On An MRI-Linac Enables On-Line QA On Dose Deposition in the Patient". In: *Proc. 57th AAPM*. Vol. 42. 6, p. 3638.

Glitzner, M., Crijns, S., Senneville, B. D. de, Kontaxis, C., Prins, F., Lagendijk, J., and Raaymakers, B. (2015a). "Dose Tracking On An MR-Linac for Online QA and Plan Adaptation in Abdominal Organs". In: *Proc. 57th AAPM*. Vol. 42. 6, pp. 3281–3282.

Glitzner, M., Denis de Senneville, B., Lagendijk, J. J. W., Raaymakers, B. W., and Crijns, S. P. M. (2015b). "Real-Time 3D Anatomy Estimation From Undersampled MR Acquisitions". In: *Proc. 57th AAPM*. Vol. 42. 6, p. 3320.

Kontaxis, C., Bol, G., Stemkens, B., Glitzner, M., Prins, F., Kerkmeijer, L., Lagendijk, J., and Raaymakers, B. (2017). "Fast online intrafraction replanning for the MR-linac". In: *5th MR in RT Symposium*.

Stemkens, B., Glitzner, M., Kontaxis, C., Denis de Senneville, B., Prins, F., Crijns, S. P. M., Kerkmeijer, L., Lagendijk, J. J. W., Berg, C. A. T. van den, and Tijssen, R. H. N. (2016). "The effects of inter-cycle respiratory motion variation on dose accumulation in single fraction MR-guided SBRT treatment of renal cell carcinoma". In: *Proc. 58th AAPM*. Vol. 43. 6, p. 3344.

Nominations

"Young Investigator award" (2017). In: *5th MR in RT Symposium*.

Acknowledgements

> Coming together is a beginning;
> keeping together is progress;
> working together is success.
>
> Henry Ford

While developing my thesis I encountered all those lines - in many languages and with many people who deserve credit. En omdat ik nog twijfel over de juiste taal van deze zinnen, I will switch to English to thank you first, Sjoerd Crijns, my brilliant daily supervisor and copromotor. From day one, you enabled me to work hands-on with cutting edge (even clinical - at daytime) equipment. Your ability to solve seemingly complex problems in elegant and simple ways inspires me and whenever I am about to write a piece of code, I tend to ask myself, "How would Sjoerd do it?". I am very proud of what we have achieved together in the last three-and-a-bit years. Both in the field of radiotherapy and assessing optimal force vectors in the bouldering hall!

Obviously, I owe special thanks to both my promotors, Jan Lagendijk and Bas Raaymakers: your vision and relentless efforts in the developments of the MR-linac project provide the raison d'être for *Motion compensation for MRI-guided radiotherapy*, which has been a fascinating topic for me ever since. I am very proud and pleased to make a contribution to this very subject. Bas, thank you for your positive and yet realistic perspectives on scientific issues and technicalities ("Nobody will read it. Sorry, Markus!") which have given me much tailwind during my PhD track, SoRTS demonstration and the First-in-Man preparations. Jan, I am very thankful that, even in the busiest periods, you provide a calm anchor and LOTS of confidence and freedom to develop to everybody working around the MR-linac. I also really appreciate the many remarkably (sometimes painfully) accurate, concise and impressively fast (6 min registered record time) comments on all the papers, talks, abstracts and finally the dissertation!

My gratitude goes out to my second daily supervisor Baudouin Denis de Senneville, as each one of the papers in this booklet carries the signature of your research on motion estimation[1], which significantly shaped this thesis. Your ability to patiently listen to problems and turn them into new research opportunities is

[1] RTTracker `http://bsenneville.free.fr/RealTITracker/`

quite remarkable! Thank you for all your support and input in scientific, moral and athletic matters (What a swimmer!). I am excited about wrapping up our current projects and hope we will continue the successful collaboration after my graduation. Thank you also for complimenting me for managing to drive my car into the totally locked down main shopping street of Bordeaux!

I would like to express my sincere gratitude to the thesis assessment committee members and/or defense ceremony opponents, Prof. Ben Slotman, Prof. Chrit Moonen, Prof. Chris Terhaard, Prof. Uwe Oelfke, Prof. Peter Luijten and Dr. Maurits Barendrecht for the evaluation of this thesis.

Moving to another country can be burdensome and requires a lot of motivation. Thus, I would like to express my appreciation to Prof. Rudolf Stollberger, Prof. Hermann Scharfetter (both TU Graz) and the European Commission, for promoting and funding my Master's graduation project within Philips Research, Eindhoven, where my supervisor Rolf Lamerichs introduced me to the art of ^{19}F MRSI ("life is terrible and there is always an echo") and the Dutch way of working.

Since then, working with the Dutch was formidably productive, and I would like to thank all my estimated co-workers from IT, the linac engineers (sorry for all the missing leaves), in particular Jan Kok for his inspiring electronics lessons (the Kasteel is best before 8/2019!) and the incredibly talented MRL physicists and assistants from the U2 mission control center including Hanneke, Rob, Wilfred, Marielle, Sara, Bram, Jochem and Simon, who deserves an XL thank-you for the very helpful and critical comments while proof-reading the English manuscript and for the fun Dutch lessons together! I would also like to acknowledge the great work of the radiotherapy and MRI technicians, particularly Tuan for helping with the first MRI-tracking experiments, contributions to protocol developments and enthusiasm, the AiOs, in particular Fieke Prins for the great planning efforts and the entire MR-HIFU group around Mario Ries for being great partners in crime for bold experiments and ideas. A special, huge, thank-you and *¡hola!* goes out to Alexis, Gijs and Peter for spending numerous and humorous day and evening hours discussing, debugging, fixing and (hopefully) improving hard- and software at U2. 1ATL - *we were there*! I am confident that our upcoming projects are going to be great, again!

In the context of 1ATL, the SoRTS project and the preparation for *First-in-Man*, I would like to thank Marco Luzzara, Hugo Gratama van Andel, Rob Spaninks, Jeroen Schuurman and Sneha Cloake (all Elekta) and Marijn Kruiskamp and Eveline Alberts (both Philips) for the good collaboration.

Ein großes Dankeschön an die Wissenschaftler vom ICR/RMH in London rund um Martin Fast (auch an Maple!), für die tolle Zusammenarbeit und lustigen group socials während meiner doch recht zahlreichen Aufenthalte im Zuge des Adaptive-Tracking-Margins-Projekts. Ich freue mich schon auf die nächsten gemeinsamen Unternehmungen!

Spending quality time with my fellow PhDs, colleagues and friends here in Utrecht played a big role in the formation of the thesis. Thank y'all for the countless squash and tennis matches, heavy lifting, crossfit sessions, road trips, pelican moments,

ice skating, swims, boulders, conferences, drinks, coffees, kapsalons, carnivals and King's/Queen's days Charis, Maxence, Jean-paul, Pascal, Pim, Mariska & Marc, Stefan, Bjorn, Matteo, Michaela, Ellis, Filipa, Tim, Tom, Martijn, Saman & Kim, Cyril, Henry, Matt, Ana, Charlotte, Cornel, Stan, Charles, Ivan, Xiao Xu, Yulia, and Tristan, squash-champion, great translator and paranymph at my side during the defense ceremony. I am looking forward to many more collaborations and much more fun together!

Liebe Leute in, um und aus Österreich, Susanne, Alin, Matthias Graz, Matthias Wien, Isi mit Vincent & Co., Hassan, Marietta (das Cover ist genial geworden!), Franz & Kinga, Chri & Monika, Benedikt & Ludovica, Philipp & Nasti, Moritz & Jana, Angy & Andi, Willi & Selina, und viele mehr, es macht jedes mal gewaltig Spaß, Euch zu treffen und in der guten alten und neuen Zeit zu schwelgen.

Elisabeth, Schwesterchen und Paranimf, wenn Du unsere Lebensläufe mal nebeneinander legst, wirst du einen großen Deckungsgrad (mit Latenz!) fest stellen. Deine Arbeit hat meine Laufbahn bis heute entscheidend beeinflusst. Für deinen guten Einfluss, deine pep talks, großartigen Optimismus und für die zahlreichen gemeinsamen Trips durch Österreich, Spanien, Kanada und Kreta danke ich Dir. Ich wünsche Dir das allerbeste! Für Dich springe ich sogar vom Stockbett!

Mein aufrichtigster Dank gilt meinen Gönnern und Mentoren, Volker und Barbara. Ihr habt es mir ermöglicht, mich frei in der in der Akademia bewegen zu können - von meinen ersten Code-Zeilen, auf dem von Euch geschenkten Computer, bis zu meiner Diss. Die vielen lustigen Familienfeste und Sommerferien mit Euch konnten die Ba(k)tterien immer wieder voll aufladen und die gemeinsamen kulturellen Events und Diskussionen sorgten für enorm viel Inspiration in allen Lebenslagen!

Liebe Tant', mein ehrliches Dankeschön für Deine anhaltende Unterstützung und dass Du immer die bemerkenswert richtigsten und schärfsten Kommentare auf Lager hast ("Des kennan sie si einrexen"). Und an die Familie in Mariazell, meine Oma und Tante Frieda: Treffen mit Euch wecken immer wieder schöne Erinnerungen und sollten definitiv öfter vorkommen!

Dear Marielle, dear chica, it is hard to tell how much of all this is due to your support and compassion - it is certainly a lot. Thank you for your courage to move to Utrecht to share a life and a home with me - sometimes without heating, but always with a lot of fun, cosiness and creativity. Sitting back and reflecting your advice made me taking the right decision more than once. And if I took a bad one, you helped me to get it right again. Thank you for having my back!
The many big and small steps we have already taken together make me really curious what's there to come. *Peut-être même en français*?

In Memoriam

Dipl. Ing. Norbert Glitzner
*16. Mai 1942 †2. April 2008

Curriculum vitae

Markus Glitzner was born on October 10, 1985 in Hallein bei Salzburg, Austria. After primary school in Elsbethen, he studied modern languages, programming and electronic circuit design at Neusprachliches Gymnasium Salzburg and Höhere Technische Bundeslehranstalt Salzburg. In 2006, he enrolled at Graz University of Technology and obtained his Master's degree ("Diplom-Ingenieur") in Biomedical Engineering in 2013 with distinction. For his Master's thesis at Philips Research, Eindhoven, he focused on the detection of ^{19}F-based contrast agents using MR spectroscopic imaging. Fascinated about MRI-guided radiotherapy, he started his PhD within the MR-linac project at University Medical Center Utrecht, the Netherlands. The results of his research about motion compensation using on-line MRI are presented in this thesis.

Markus took a position as a computer scientist in the radiotherapy department at UMC Utrecht. He continues his research and development around the MR-linac project, pushing towards *First-in-Man* and software solutions for on-line MRI-guidance and real-time machine control for motion-adaptive radiotherapy.